Doctoral Dissertation

Control System Design and Stability Analysis of Legged Locomotion Robots Based on Tensegrity Structures and Its Morphology

Yanqiu Zheng

Supervisor: Fumihiko Asano

Graduate School of Advanced Science and Technology
Advanced Science and Technology
Information Science

September 2023

Abstract

Inspired by biology, biomimetic robots imitate living organisms to enhance their adaptability and mobility. Designing robots based on their morphology can provide specific functions, but there is a lack of unified guidance and efficient research methods in this area. Therefore, an innovative theory of robot morphology is urgently needed. To establish this system, a representative minimal model is necessary to explore essential issues and provide a research platform. The first step in robot morphology is designing a minimal model that can serve as a platform for future academic research.

Rigid and soft robots are the two main types of robots, each with unique features and applications. Rigid robots offer higher precision, speed, and agility due to their mathematical models, especially their dynamic models. Soft robots, on the other hand, have high adaptability but struggle with high-precision mathematical models, resulting in slower speed and lower accuracy. However, the adaptability of soft robots cannot be replaced by rigid robots.

The significance of robot morphology lies in finding the optimal form for specific tasks. Variable soft robots are advantageous as a minimal model because their structures are more changeable compared to rigid robots. However, the study of soft robots often doesn't utilize high-precision mathematical models, which contradicts the requirements of the minimal model.

Tensegrity robots combine the precision and agility of rigid robots with the adaptability of soft robots, making them lighter, stiffer, and more versatile. They have gained attention in recent years, such as NASA's Super Ball Bot for planetary exploration. However, these robots face challenges, such as difficulties in building dynamic models, limiting their high-speed motion control. Despite this, tensegrity robots offer opportunities for dynamic modeling, making them ideal candidates for studying robot morphology.

This paper focuses on a minimal model called the rimless-wheel-like tensegrity walker (RWT), inspired by the widely studied rimless wheel (RW) model for legged locomotion. The dynamics model considers the internal coupling force from elasticity and the external constraint force from the environment. Different movement modes are discussed, providing guidance for dynamics modeling and bridging the gap between rigid and soft robots.

Considering practical applications, modifications to the minimal model are necessary. For instance, the SLIP model based on an inverted pendulum explains the motion of the center of gravity during human walking more effectively. Extensions to the RW model accommodate objective conditions like semicircular feet and frictional road surfaces, improving the model's accuracy. A MATLAB-based simulator is designed, demonstrating that the RW achieves periodic passive gaits and stability even when each rod is independent. Changes in the internal structure lead to discrete changes in the RW's characteristics, showcasing the importance of morphology. Morphological transitions based on the proposed morphology-based control (MBC) theory enable different gaits such as crawling, walking, and hopping. The MBC approach simulates morphological changes by controlling inputs, enhancing adaptability and stability of the control system. A simplified version of the model, the simplified rimless-wheel-like tensegrity walker (SRWT), achieves continuous morphological changes through MBC, resulting in locomotion on flat ground. Detailed analyses of gait, stability, and applications are provided. Physical experiments validate the minimal model of robot morphology. Verification experiments reveal drastic internal property changes in tensegrity robots with varying structures, confirming the necessity of the RW as the minimal model. Engineering experiments demonstrate flat walking of the SRWT based on the presented theory, highlighting the model's relevance in academic research and engineering applications.

In conclusion, this study introduces the minimal model for robot morphology, providing a theoretical method and advancing its implementation. Dynamic modeling of tensegrity robots offers insights for high-speed and high-precision movement and interaction with rigid and soft robots. The experiments demonstrate the positive impact of the proposed model in engineering applications.

Keywords: Robot morphology, Minimal model, Tensegrity robots, Rimless wheel, Dynamics modeling, Stability analysis

Acknowledgments

I thought that completing my dissertation would bring me a strong sense of achievement and satisfaction. However, now I feel even more fortunate to have had the opportunity to pursue a doctoral degree, and to have a deeper understanding of the meaning of acknowledgments.

First and foremost, I am grateful to my advisor, Professor Fumihiko Asano, who has been instrumental in shaping my career path. I feel lucky to have joined Asano Lab eight years ago and to have met Professor Asano, for whom I am deeply grateful for his guidance and assistance. He has taught me that true education is not like PID control, where the controller fights against the object being controlled and forcibly increases the input to produce a result. Rather, it is more like the MBC proposed in this study, which changes the essence (morphology) of the object through input, thus enabling it to develop strong characteristics and to be self-sufficient in future endeavors. This concept was one of the inspirations behind the control approach presented in this dissertation. Professor Asano has not only guided me academically and provided me with help, but he has also been extremely accommodating in my personal life, for which I am truly grateful. I hope to work even harder in the future and live up to the reputation of Professor Asano.

Research is not only about hard work but also about exchanging ideas and receiving new perspectives. Therefore, I am also grateful to my co-advisor, Professor Yonghoon Ji, who provided me with valuable advice during critical moments and has shown me a different attitude towards both academic and personal life, which has always given me a positive outlook.

I would also like to express my special thanks to Professor Sang-Ho Hyon, Professor Ichiro Jikuya and Professor Kunihiko Hiraishi, who, despite their busy schedules, took the time to review my dissertation and provide me with professional academic and editorial advice. I am very grateful for their guidance, and I believe that through their feedback, I will submit an improved final dissertation.

I would like to thank Professor Yuxiang Yang for his influence on my life. Even though he was not my advisor during my university years, he showed me the charm of academia and guided me onto the path of scientific research. He has been a lifelong inspiration to me.

I am thankful to all of my advisors for guiding me in the right direction with my research, and to my seniors and friends, Li Longchuan, Yan Cong, He Yuetong and Xiang Yuxuan, for their help with minor issues. Daily discussions and interactions with my lab mates made my intense research life more enjoyable, and I learned new ideas and knowledge from them, for which I am truly grateful. I would also like to extend my special thanks to Xiang Yuxuan, who helped me with many time-consuming and tedious tasks, allowing me to focus on my research.

I am also deeply grateful to my partner, Wang Zhe. Since we had a child, she has taken on the responsibility of running the household and taking care of the child, which has helped me to focus on my studies. With our child being so young and requiring constant attention, she would stay up late to put the baby to sleep and avoid disturbing me, which made me feel guilty. I did not have enough time to fulfill my duties as a husband, so I will work hard to be a better partner in the future.

I would also like to express my sincere gratitude to my parents. Although they may not understand the specifics of my research, they trust and support me unconditionally, enabling me to focus on my studies without any concerns. Since they do not live in Japan, they cannot inform me of any family issues, and I feel guilty about that. I hope to take good care of them in the future.

Finally, I would also like to express my gratitude to JAIST for providing me with the environment to conduct my research, the scholarship they awarded me, the research grants (Houga) they provided me with, and the daily assistance from all of the staff.

List of Figures

List of Tables

Acronym and Abbreviation

BOA	Basin of attraction
COM	Center of mass
DOF	Degrees of freedom
DSP	Double-legged-support phase
NSP	None-legged-support phase
MBC	Morphology-based control
MSP	Multi-legged-support phase
RW	Rimless wheel
RWT	Rimless-Wheel-Like Tensegrity Robot
SRWT	Simplified Rimless-Wheel-Like Tensegrity Robot
SSP	Single-legged-support phase
TSP	Triple-legged-support phase
ZMP	Zero moment point

Table of Contents

Chapter 1

Introduction

1.1 Background

1.1.1 Biorobotics

Mobile robots are autonomous robots capable of moving and performing various tasks in different environments [11]. They have become an important research direction and development focus in the field of robotics technology [12–15]. Mobile robots have broad application prospects and play an important role in many fields, such as industrial production, agricultural production, medical surgery, and exploration. The significance of mobile robots lies in their ability to replace humans in performing tasks that are dangerous, repetitive, fine, high difficulty, and high risk, thereby improving work efficiency and ensuring work safety [16–20]. In addition, mobile robots can also extend human capabilities, allowing humans to access more dangerous and unreachable environments. Therefore, research and application of mobile robots are of great significance for promoting the development of robotics technology and improving human production, life, and exploration levels [21–24].

According to their mode of movement, mobile robots can be divided into various types. Among them, legged and wheeled mobile robots are the most common types [25–27]. Legged mobile robots simulate animal locomotion through biomimetic design and can move freely in different terrains and environments [28, 29]. They have advantages such as strong adaptability, high flexibility, energy efficiency, high safety, and wide applications, and thus have broad prospects in exploration, search and rescue, agriculture, industry, and medicine in the future [30–33].

a. Robo-shark of Robosea

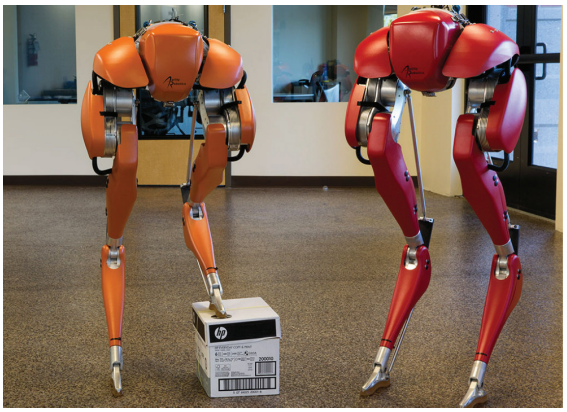

b. Cassie of Agility robotics

c. Spot of Boston dynamic

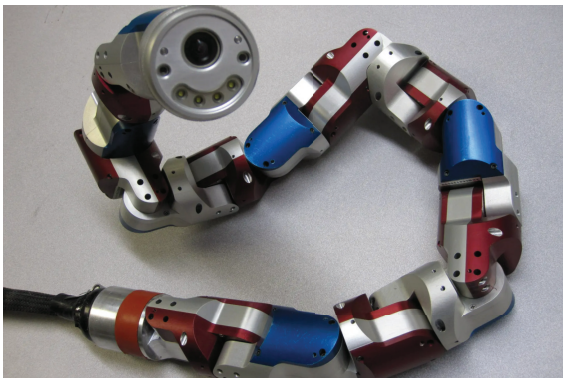

d. Snakerobot of Biorobotics Lab

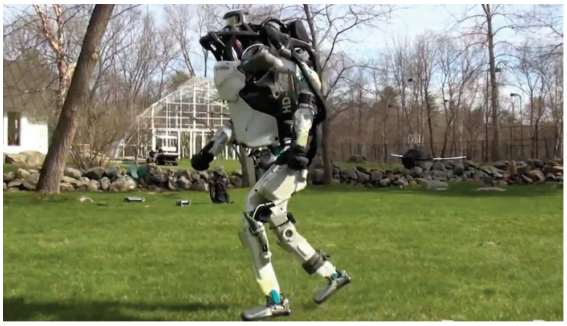

e. Atlas of Boston dynamic

f. BionicWheelBot of Festo

Figure 1.1: Various bionic robots [1–5]

However, control of legged robots is a challenging problem. For example, the typical underactuation [34, 35]. The underactuation problem of legged mobile robots refers to the situation where the number of degrees of freedom of the legged robot is greater than its controllable degrees of freedom. Specifically, a legged robot may have multiple joints and motion degrees of freedom, but not all degrees of freedom can be controlled due to system constraints and dynamic limitations [36].

For example, a robot with six legs, each leg having three joints, has a total of 18 degrees

of freedom. However, due to system dynamic limitations and constraint conditions, only 12 degrees of freedom may be controllable. This situation is referred to as underactuation.

Underactuation can lead to unstable and unpredictable robot control. When the robot is in an unstable state, it may lose balance, fall, or be unable to continue moving. Therefore, solving the underactuation problem is crucial for controlling legged robots [37].

In contrast, animals are a typical underactuated model, but they can easily move in different environments because they have high environmental adaptability and autonomous motion capabilities, and can achieve efficient and stable motion through nonlinear control and feedback mechanisms. Therefore, studying animal locomotion has important reference value for solving underactuated control of robots [38–40] as shown in Figure 1.1.

1.1.2 Morphology

As intelligent beings, humans and chimpanzees share similar body structures, including heads, bodies, and limbs, but they differ significantly in their modes of movement. For instance, humans primarily rely on their legs for walking, while chimpanzees use all four limbs to climb.

Additionally, humans are unable to climb vertically like felines. Unlike humans, felines can easily climb vertically on trees or walls because they have sharp claws and strong muscles that enable them to maintain balance and grip surfaces. Humans lack these features, as our fingers cannot grip like feline claws, and our muscles and bones are not adapted to this type of movement.

Humans are also unable to run at extreme speeds like cheetahs. Cheetahs can run at extremely high speeds because their body structure and muscles are adapted to this type of movement. Cheetahs are very agile, with long and soft limbs that enable them to move quickly. In contrast, human body structures and muscles are not adapted for high-speed running, as our legs are relatively short, and our bones and joints are not flexible enough.

We are also unable to hang easily from trees like primates. Primates can easily hang from trees because their arms and legs are long, and their fingers can grasp tree branches. The human body structure is not suited to this type of movement, as our limbs are relatively short, and our fingers are not flexible enough.

Although humans have highly developed brains, we are unable to perform movements and achieve performance levels similar to some lower animals. This suggests that morphological

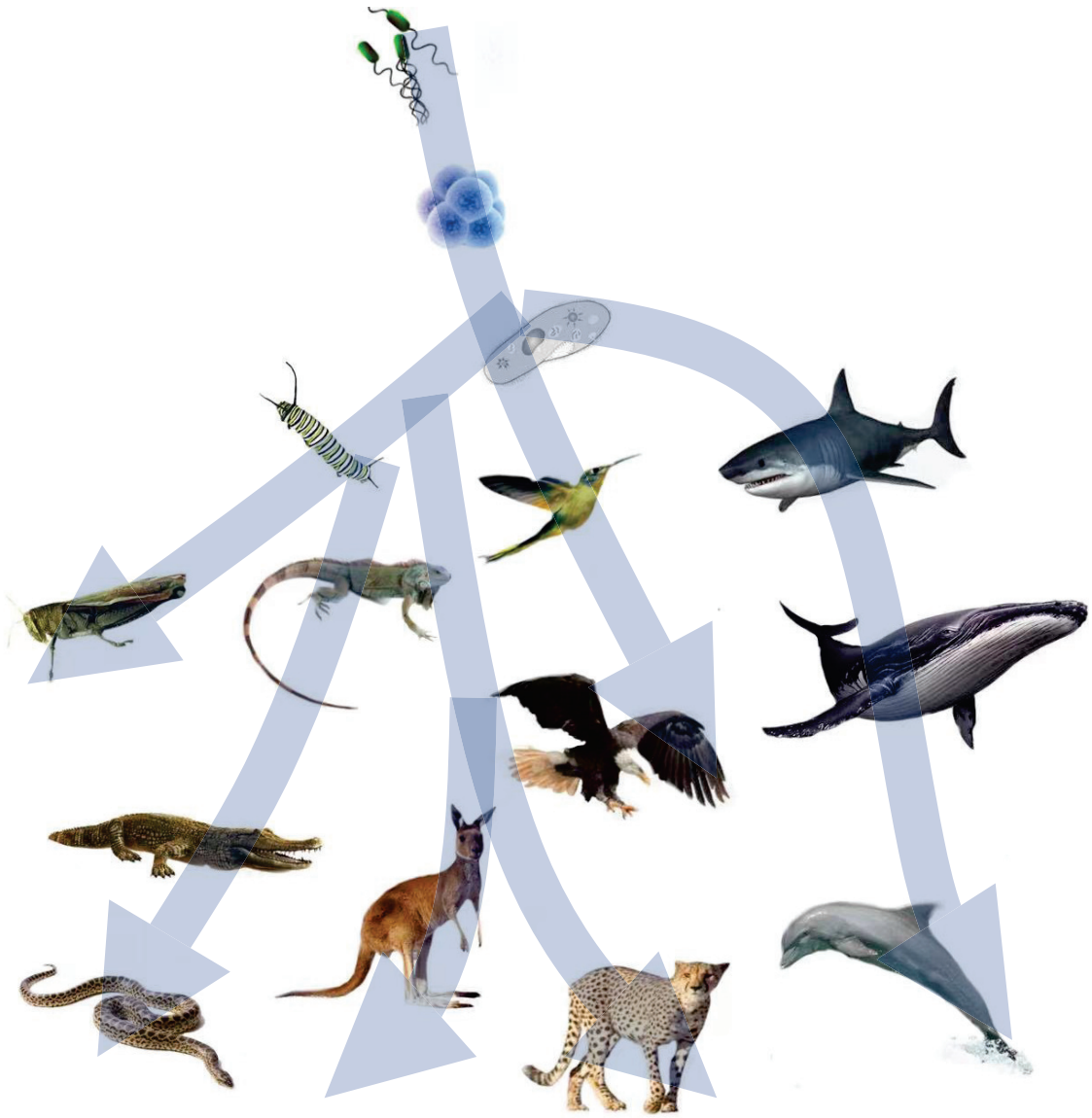

Figure 1.2: Evolution. Under natural selection, various morphologies have evolved with different modes of movement.

factors of movement and performance are more important than brain function. Despite being highly intelligent, humans' bodies are not adapted for all types of movement, and our physical limitations restrict us in certain ways.

In recent years, morphology has become an important criterion in robot design [41–44]. Morphology studies the shape, structure, and function of organisms, including how they move and perceive their environment, and how they adapt to their living conditions. The findings of these studies have significant implications for robot design, making morphology an essential reference for designing robots.

The main idea of morphology is to design robots that correspond to the shape, structure, and function of organisms , as shown in Figure 1.1. This approach can make robots better adapted to specific tasks and environments. For example, biomimetic robots can mimic the swimming posture of fish, resulting in more efficient swimming ability. By imitating the leg structure of insects, robots can walk in complex environments. Similarly, by designing wings based on the structure of birds, robots can achieve better flight performance [45–48].

Morphology can also help robot designers optimize the structure and function of robots. By studying the anatomy and kinematics of organisms, many structures and movements with high energy efficiency can be discovered. Applying these principles to robot design can result in robots with higher energy efficiency and longer working time.

Therefore, morphology has become an indispensable part of robot design, improving robot performance and adaptability, making robots more in line with human needs [49–51].

1.1.3 Evolution and significance of morphology

Evolutionary theory posits that the morphological evolution of organisms is driven by the processes of natural selection and genetic variation [52] as shown in Figure 1.2. The morphology of an organism is tightly linked to its environment, and it continually adapts to changing environmental conditions in order to improve its chances of survival. This adaptive evolution includes many aspects, such as body size, color, structure, and behavior [53].

When environmental factors change, organisms need to adapt to the new environment in order to maintain their ability to survive and reproduce. For example, when a plant is transplanted to a new environment, it may need to adapt to new temperature, humidity, and soil conditions. In this case, the plant may produce new morphologies, such as deeper roots and thicker leaves, to adapt to the new soil and climate conditions.

Consider the evolution of cheetahs. Cheetahs are a mammal that runs at high speeds and needs to catch prey in a short amount of time. Therefore, the cheetah's body has evolved into a long and slender morphology, giving it better speed and agility. At the same time, the cheetah's mode of locomotion has also been continually optimized with the evolution of its body morphology, such as by increasing muscle elasticity and changing its gait, to maximize running efficiency and speed.

In the evolution of birds, their wings gradually evolved into a morphology that is adapted

for flight as the environment changed, and their mode of flight was also continually optimized through evolution to match their wing morphology, such as with flapping flight and gliding flight. This high coupling of flight and body morphology allowed birds to achieve highly efficient and agile flight.

The body of lizards has evolved to be highly adapted for running on the ground, with a flat body, long and flexible trunk, strong limbs, and a long and powerful tail. This morphology enables lizards to quickly run, turn, accelerate, and decelerate, allowing them to evade predators or catch prey.

The morphology and mode of locomotion of organisms are interdependent and adaptive to each other, evolving in concert to meet different environmental demands. This process of mutual adaptation has led to a high degree of coupling between motion and morphology [54, 55].

1.1.4 Morphology and motion

The previous section explained the highly correlated relationship between morphology and motion, but how exactly does morphology determine motion?

Selection pressure refers to various factors in the natural environment, such as competition, predation, climate, resource availability, etc., that affect the survival and reproduction of individual organisms and species, leading to the process of selection or exclusion of certain traits or behaviors in a population. Long-term selection pressure can promote adaptive evolution in individuals or species to adapt to their environment [56, 57].

As shown in Figure 1.2, under selection pressure, corresponding morphologies produce corresponding modes of motion, which as products of selection pressure, provide feedback to their own morphology, ultimately minimizing the selection pressure. Here, under selection pressure, the pressure is transformed through morphology into a mode of motion, and the transformation of different morphologies results in different modes of motion. Therefore, this can also explain why humans are limited by their own morphology and cannot match the modes of motion of other animals.

Passive walking was discovered in the last century and is a walking method in robotics that is achieved through passive components [58], such as passive mechanical structures like springs, pendulums, or wheels, rather than through active motors or other active components [59, 60]. Such walking is natural and energy-efficient and closely resembles human gait. This

type of walking converts gravity into a mode of motion through the characteristics of its own structure [61].

Passive walking not only demonstrates that under pressure, corresponding modes of motion can be produced through morphology, but it can also be used to study the relationship between morphology and modes of motion. That is, what is the best mode of motion corresponding to the current morphology.

Therefore, when we want to change the mode of motion or address a specific task, we can first consider changing the corresponding morphology to achieve the desired mode of motion, because this produces not only efficient but also natural and stable motion. Of course, finding the optimal morphology is extremely difficult, and the passive gait method can only provide the mapping relationship from morphology to motion, and the establishment of the reverse mapping relationship is not easy.

1.1.5 Morphology, control and morphology-based control(MBC)

The common practice in the past has been to establish a relationship between control and movement by directly ignoring or not fully considering the influence of morphology [62]. Such movements rely entirely on control algorithms, which are highly developed by the brain. However, if we take into account the morphology, we can effectively match our highly developed brains with the environment or task, resulting in significantly improved outcomes [63].

As shown in Figure 1.3, while calculating the optimal control method can achieve the goal of moving a stone, attempting to change the stone's morphology can greatly simplify the control cost and produce even better movement results.

Eq. 1.1 is the general state space equation composed of two parts, where Ax is the zero-input response and Bu is the zero-state response. The most general way , the PID control is to make state x get to target state x_t by designing the Bu term to make state x point to x_t along the shortest path, where the tracking error from x to x_t is used as feedback, aiming to minimize the error and achieve control. This method is simple and easy to implement, but it has poor anti-interference ability. Mathematically, this means that when designing the Bu term, only the feedback of state x is considered.

$$\dot{x} = Ax + Bu \tag{1.1}$$

By considering the system characteristics, the designed trajectory may not be the shortest path

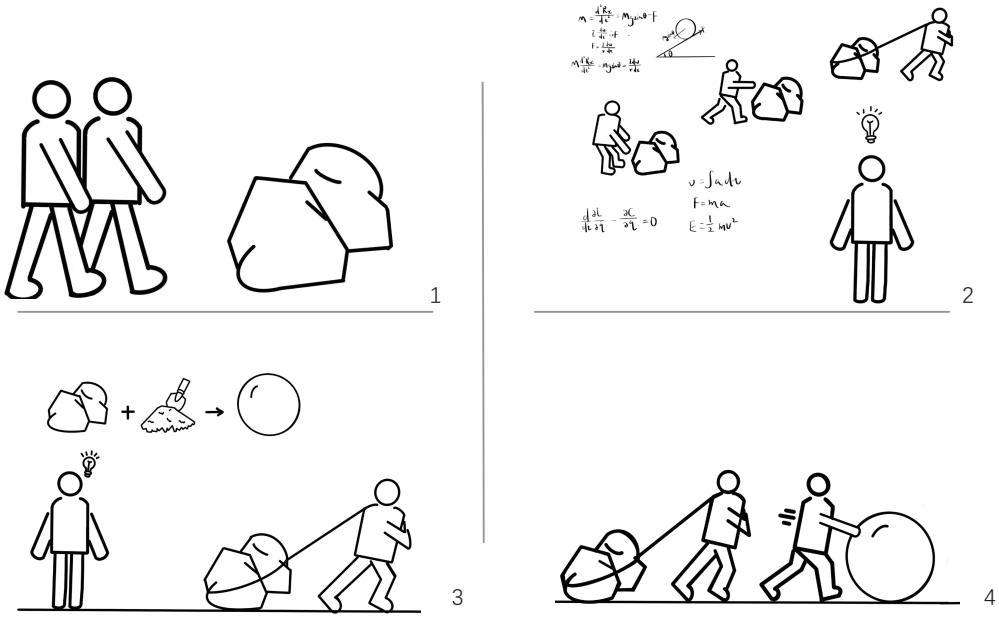

Figure 1.3: Locomotion in different morphology

as described above, but it must be the more adaptive one because it does not need to resist the system characteristics. It greatly enhances the system's anti-interference ability by conforming to its movement characteristics. This reduces control cost, making it easier to achieve better control effects than PID control.

The above control methods are all based on the assumption that the movement characteristics do not change. If morphology can change, however, the most intuitive effect is to make $Ax + Bu$ variable. By designing the change in morphology, we can change the convergence characteristics of the system even without using the control term Bu. This significantly reduces control difficulty and can even achieve movement without control.

The natural evolution of organisms is actually a process of reducing the complexity of control methods and improving the morphology characteristics based on the natural selection pressure of specific tasks. This ultimately leads to the most straightforward control method being able to achieve complex movements through morphology characteristics alone. Therefore, for robots, if we can control morphology, the simplest, and even no control input, can achieve complex movements and excellent performance.

Therefore, the change in morphology is crucial. This study proposes a concept based on morphology-based control, as shown in Eq. 1.2.

$$Ax + Bu \rightarrow A'x + B'\tau \tag{1.2}$$

Here, $Ax + Bu$ can be seen as the original morphology, and by controlling u, the current morphology becomes the new morphology $A'x + B'\tau$.

The proposal of MBC is inspired by previous research on morphology and control. Chandana Paul [64] investigated the impact of a robot's morphology on its control requirements, which has become increasingly evident in the field of robotics. Morphology not only determines the achievable behaviors but also influences the control effort needed to perform those behaviors. This relationship was initially observed and described by Pfeifer in her work "Understanding Intelligence," but the underlying mechanisms remain unclear. The authors suggest that the dynamics of morphology may play a computational role within the system, potentially replacing some aspects of control functions. Therefore, exploring the relationship between morphology and control can be used for analysis and guide the design of robots with reduced control demands. The goal of this paper is to explore this possibility.

Nygaard, T. F. [65] indicates that evolutionary robotics aims to address this issue by optimizing both the control and the body (morphology) of robots, enabling them to adapt to internal and external variations. Most of the work in this field has been conducted in simplified physics simulators, which lack the rich interactions found in the real world. As a result, there are few solutions that rely on complex interactions between control, body, and environment.

Füchslin [66] states that morphological computation can broadly be defined as an approach that utilizes the shape, material properties, and physical dynamics of a physical system to enhance computational efficiency. Morphological control is the process of applying morphological computation to control tasks. In the theoretical part of the author's research, they further refine and expand these definitions by proposing new formal definitions and identifying areas where our proposed definitions are still incomplete.

In studies [67, 68], the consideration of morphology and the utilization of morphological characteristics to achieve control objectives are also mentioned.

It is evident that morphology plays a crucial role in control and even the locomotion performance of robots. However, although current research is based on the idea of leveraging morphological characteristics to change the properties of the morphology, there is no unified methodology. Most approaches are tailored to specific robot requirements, lacking generality.

In contrast, this study presents a general approach and provides specific examples of morphological control based on the robot described in this paper.

Although MBC has many advantages, it also has some limitations, as compared to traditional methods, as shown in Table 1.1.

According to Table 1.1, it can be observed that MBC is particularly suitable for higher-order nonlinear systems. These types of systems are challenging to control, and traditional methods, such as reducing the order or using approximation techniques, are often ineffective. In such cases, it becomes difficult to determine the state changes of these higher-order nonlinear systems. However, while the state changes may be elusive, the ultimate convergence trends of these systems, known as behavior of attractor, may objectively exist. MBC, by manipulating the system's characteristics through input, can generate or modify its attractor. By guiding the attractor towards the target position, the desired motion can be achieved. This approach is more indirect, and the time to achieve the motion is unknown. However, indirect control can be achieved by adjusting the convergence velocity to the attractor. MBC leverages the concept of morphology to address the challenges in controlling higher-order nonlinear systems that traditional control methods struggle to solve. Additionally, the addition of MBC control to traditional control methods can significantly improve control effectiveness.

Table 1.1: Comparison of MBC and traditional control methods

	MBC	Traditional control methods
Control Objectives	Morphological characteristics (e.g. equilibrium position and its convergence)	Relative position of the structure
For the realization of the movement	Indirect	Direct
Motion response time	Long	Short
Stability	Higher	Standard
Difficulty of realization	Easier	Standard
Applicable Systems	Higher-order nonlinear systems (hard to linearize)	Linearizable or approximable systems

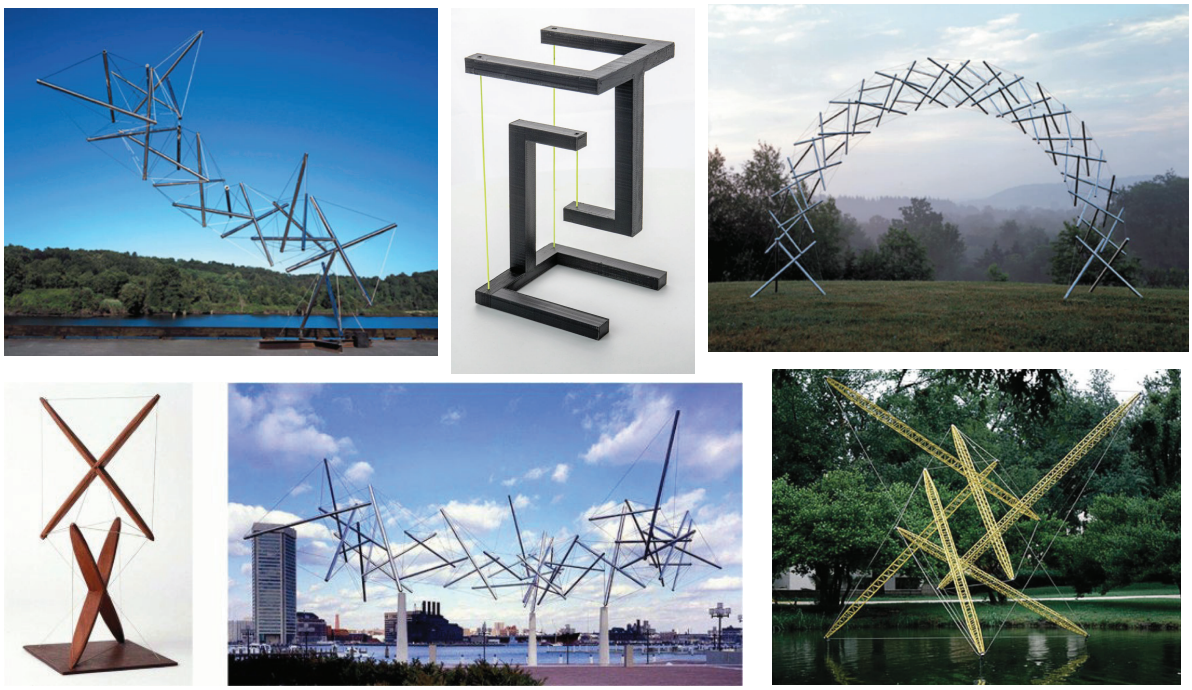

Figure 1.4: Tensegrity structure [6, 7]

1.1.6 Tensegrity structure and tensegrity robot

The necessary condition for morphology-based control is that the morphology is variable. Although rigid robots have advantages such as high speed and high precision, they cannot easy to change their morphology [69, 70]. Soft robots, on the other hand, can change their morphology and have high adaptability, but they face difficulties in dynamics modeling, slow speed, and low precision [71, 72]. Therefore, a tensegrity structure that is both morphologically variable and has both rigid and soft characteristics is the best candidate for this purpose.

Tensegrity [73] as shown in Figure 1.4 is a structural system composed of the words ”tension” and ”integrity”. It was originally proposed by American designer R. Buckminster Fuller and further developed by his student Kenneth Snelson. Tensegrity structures achieve stability through the balance of tension and compression between different parts. They are composed of a series of struts and tensioned wires arranged in a triangular lattice structure. The struts can only withstand compression and not tension, while the tensioned wires can only withstand tension and not compression [74]. They will form an empty mesh, i.e., they are spatially stable.

Tensegrity structures are characterized by high self-stabilization and flexibility. They can withstand complex external loads and maintain stability in different directions. This makes them widely applicable in fields such as architecture, engineering, aerospace, and biology [75, 76].

DuCTT, for Duct Climbing Tetrahedral Tensegrity

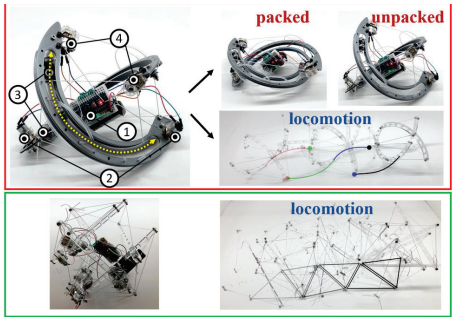

Agile Robotics Lab

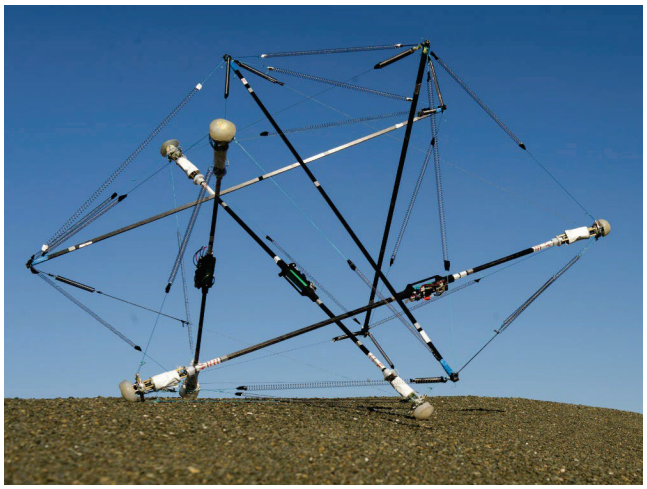

Super Ball Bot of NASA

Figure 1.5: Tensegrity robots [8–10]

The development of tensegrity robots [77–80] has been ongoing since the concept was first introduced in the 1950s. Tensegrity robots as shown in Figure 1.5 have a variety of potential applications due to their unique design and capabilities. They have been studied for use in exploration, search and rescue, and even as artificial muscles in prosthetic devices [81]. In exploration, tensegrity robots could be used to navigate rough terrain or even explore other planets. They could be sent to areas that are too dangerous for humans to access, such as disaster zones or hazardous materials sites. Tensegrity robots are also being explored as a means of transporting payloads in space, as their lightweight and flexible design makes them ideal for use in microgravity environments.

It is not difficult to find that tensegrity robots follow the characteristics of tensegrity structures, i.e., they are composed of compressed rods and tensile strings, and they will form a spatial mesh structure with self-stabilizing properties. In addition, they have a new derived feature, which is to generate different convergence properties with different variations of internal tension, pointing to different stabilizing structures. Moreover, this derived characteristic is how tensegrity robots achieve mobility.

Due to the tensegrity robots are the best research candidates for studying morphology in robots [82], as they combine the advantages of rigid and soft robots, such as high speed, high precision, morphing capability, and high adaptability. However, their high degree of freedom

makes it challenging to model their dynamics, which currently limits their ability to achieve high-speed and high-precision movements, thereby restricting their application in the study of robot morphology.

1.2 Research Aim and Significance

Robot morphology can serve as a guideline for robot design, enabling the search for optimal solutions in structure and reducing control complexity to enhance robot performance. However, due to the complex structure and control system of robots, building an accurate model is challenging. Moreover, the more complex the model, the greater the computational complexity, making it difficult to handle. Therefore, to address these issues, this study proposes the RWT minimal model based on the characteristics of tensegrity robots, which aims to simplify the robot model while retaining its essential features. This provides a concrete research object for robot morphology studies and offers academic value for further theoretical research.

In addition, the mathematical modeling method presented in this paper aims to be solve so that it can provide guidance for the dynamics modeling of tensegrity robots, allowing them to truly leverage their advantages as both rigid and soft robots, thereby offering more practical value. Furthermore, the method employs the modeling techniques of rigid robots to describe the structure of soft robots, promoting interaction between the fields of rigid and soft robots.

Another contribution can be expected by this study is the proposed morphology-based control (MBC), which provides the idea of changing form and adapting to circumstances, rather than opposing them, thereby reducing effort and improving control. This control concept is not only applicable to the robots studied in this research but also has generality.

Finally, the RWT minimal model developed in this study has practical engineering significance, allowing for better adaptation to the environment through its inherent morphological characteristics, which have specific applications in fields such as rescue operations and space exploration.

1.3 Research Methodology

1.3.1 Minimal mathematical model of the tensegrity robot

The benefits of using the minimal model which is the simplest model possible in robot modeling can be numerous [83–85]. First, simpler models are often easier to analyze mathematically and computationally, which can facilitate the process of designing, testing and optimizing the robot's behavior. Second, simpler models can also be more robust and reliable than complex ones, as they have fewer parameters to estimate and fewer potential sources of error. Thirdly, simpler models can be more generalizable and transferable to new environments and tasks, as they are less specific and more abstract. Finally, simpler models can be more interpretable and explainable, as they can reveal the underlying principles and mechanisms of the robot's operation in a more transparent way. Therefore, the use of the simplest model possible in robot modeling can lead to a more efficient, effective, and understandable robotic system.

As one of the minimal models of legged locomotion, rimless wheel model has been widely used to study gait analysis and control problems in various legged robots [86–88]. In the development of the rimless wheel model, researchers gradually discovered many interesting dynamic and control characteristics of the model, which can be used to explain and predict the behavior of real robots. For example, the rimless wheel model is an important tool for studying gait control problems in legged robots. Its simple structure and adjustability allow researchers to explore the gait of robots by changing initial conditions and parameters, providing useful references for designing and controlling legged robots.

In addition, the rimless wheel model is a typical nonlinear dynamic system that can be used to study the behavior of many dynamic systems, such as chaos in nonlinear dynamics. In the rimless wheel model, researchers have found that when the friction coefficient and mass parameter exceed a certain value, its motion becomes disorderly and unpredictable [89,90]. The appearance and study of the rimless wheel model have promoted the development of nonlinear dynamics, laying a foundation for exploring the behavior and theory of nonlinear dynamic systems. Its discoveries and studies have not only important practical applications in robot control and biomechanics but also significant implications for fundamental research in other fields such as physics, mathematics, and engineering [91].

Based on the advantages of the rimless wheel model, this study proposes a new mathemati-

cal model that combines the rimless wheel structure with the tensegrity structure as the simplest unified minimal model for a morphological mobile robot. The key innovation of this study lies in the development of a foundational model for investigating morphology-based mobile robots. This model not only serves as a crucial tool for further research in this field, but also carries significant academic implications. By providing a comprehensive framework for understanding the behavior and functionality of these robots, this study offers valuable insights into the potential applications of morphology-based mobile robots and opens up new avenues for future research in the field.

1.3.2 Passive dynamic walking

Passive dynamic walking [58] is one of the important research directions in the field of robot gait control and analysis. Research on passive gaits began in the last century. Through such research, people have gained a better understanding of the fundamental principles underlying human and animal walking, as well as strategies for optimizing robot motion. Passive gaits are a type of gait that does not require any control input. They utilize the robot's own dynamic characteristics and environmental conditions to achieve gait stability through mechanical coupling or elastic components, and forward motion through momentum transfer. Such gaits are not only natural and highly energy-efficient, but also closely aligned with human walking patterns [58, 92–94]. Research on passive gaits has laid the foundation for the development of robot gait control. The human morphology that has evolved over a long period of time is best suited for bipedal walking, and through passive gaits, the most corresponding motion patterns for this morphology can be identified.

Therefore, in this study, we will use the method of passive walking to find the most suitable motion patterns for different morphologies under the simplest model, and construct the relationship between morphology and motion pattern.

1.3.3 Morphology-based control method and evaluation criterion

Based on the relationship between morphology and locomotion patterns obtained from passive gait, we propose a control method that changes the morphology of a robot to indirectly adapt its locomotion pattern to the current task and reduce control complexity. Here, we use the basin of attraction (BOA) [95, 96] as a stability evaluation criterion.

In nonlinear systems, the BOA refers to the region of the state space where initial conditions are attracted to a stable state or attractor. The attractor is a set of states to which the system evolves, and all initial conditions associated with states in the BOA are attracted to the same attractor. The BOA is used to describe the attractivity of stable states in nonlinear systems, which is typically determined by the system's dynamical equations [97–99].

In some nonlinear systems, there may be multiple attractors, each of which corresponds to a BOA. Different attractors correspond to different stable states of the system, and when the system is within a particular BOA, it exhibits certain stability properties and evolves continuously in that state. When the system is in different basins of attraction, it exhibits different stable states.

The size and shape of the BOA are usually determined by the specific morphology of the system's dynamical equations. In some systems, the BOA can be a point, line, surface, volume, or more complex shape, and in some cases, the BOA may exhibit branching, where a system may have multiple basins of attraction that are connected through branching structures [100, 101].

Therefore, we aim to use morphology-based control to change and obtain larger basins of attraction, where the attractors are precisely located at the desired control target states. This approach not only simplifies control complexity but also improves stability.

On the other hand, BOA can represent the breadth of convergence, while the Poincaré map can translate the speed of convergence. The Poincaré map, also known as the Poincaré section or the first return map, is a mathematical tool used to study the behavior of dynamical systems, particularly those that are periodic or quasiperiodic. The map is named after the French mathematician Henri Poincaré, who first introduced the concept in the late 19th century.

At its core, the Poincaré map involves taking a cross-section of a trajectory in phase space and mapping it to the next intersection of the trajectory with that same cross-section. This process can be thought of as "slicing" the phase space along a particular plane or surface, and then examining how the trajectory intersects with that plane as it evolves over time. The resulting map provides a discrete representation of the system's behavior, capturing the sequence of state transitions as the trajectory passes through the chosen cross-section.

One of the key advantages of the Poincaré map is that it can simplify the analysis of complex dynamical systems by reducing the dimensionality of the problem. For example, a 3-

dimensional system can be reduced to a 2-dimensional map by selecting a suitable cross-section, which can make it easier to visualize and understand the underlying dynamics. Additionally, the properties of the Poincaré map, such as its fixed points or periodic orbits, can provide valuable insights into the behavior of the original system, such as stability, bifurcations, and chaos.

Therefore, it is also one of the evaluation criterion in this study.

1.3.4 Experimental validation

In the field of robotics, the importance of experimental validation cannot be overstated. While simulations and theoretical models can provide useful insights, real-world testing is crucial for verifying the performance of a robotic system under various conditions and for identifying any discrepancies between the model and the actual system.

Experimental validation not only provides empirical evidence for the effectiveness of a robot's design and control algorithms, but also reveals unforeseen challenges and limitations that may not have been anticipated in simulation or analysis. In addition, the data collected during experimental testing can be used to refine and improve the system's performance through iterative design and testing cycles.

Therefore, it is essential for researchers and engineers in the field of robotics to conduct thorough experimental validation of their designs and algorithms, in order to ensure the reliability and robustness of their systems.

In this study, we focus on experiments to verify the relationship between morphology and movement patterns, and, to verify that the control methods described above are also necessary.

1.4 Organization of Dissertation

This study is divided into several parts: first, we focus on the study of tensegrity robots, propose a minimal model, establish a mathematical model, and use a passive walking method to explore the relationship between their motion and morphology. Second, we focus on validating the effectiveness of the above model, and draw conclusions about its universality and significance to robotics morphology. In the third part, we propose a control theory based on the above model, and validate it to meet engineering requirements. Finally, we draw a conclusion that proves the minimal model of robotics morphology, which has important implications.

Throughout the study, various experiments and parameter optimizations were conducted to ensure the reliability and accuracy of the conclusions.

Chapter 2 : This chapter first proposes the minimal model of a tensegrity legged locomotion robot and establishes a dynamics model. We consider internal elastic coupling forces and provide different constraint force models according to different grounding situations. In addition, collision and state transition models are also taken into account. Finally, we expand the model by considering circular feet and frictional ground surfaces, making it more generalizable.

Chapter 3 : This chapter first introduces the design of the simulator, and then, based on the simulator, the passive gait simulation results of the above model are obtained. Periodic stable gaits based on the model are observed and analyzed. Additionally, it was found that the internal characteristics could change abruptly with changes in the robot's shape, exhibiting the characteristics of morphological transitions. Therefore, we conducted in-depth research on the characteristics of the robot under different shapes and obtained different corresponding movement modes under different shapes: crawling, walking, and skipping.

Chapter 4 : This chapter proposes a model-based control approach. First, the control idea and implementation were introduced using the simplest spring-loaded cart model. Then, it was applied to the minimum model to achieve shape shifting, allowing for the observation of the transition between crawling and walking. Additionally, a simpler model was proposed and dynamic walking was achieved using MBC, while stability and application of the corresponding gait were analyzed.

Chapter 5 : The previous chapter introduced the implementation of gait based on MBC and the stability of gait under different desired postures, while the reasons why gait is stable will be described in detail in this chapter. Therefore, in this chapter, the proposed model is used to validate the achievement of limit cycle gaits for different control objectives, thereby demonstrating the necessary conditions for generating limit cycle gaits.

Chapter 6 : This chapter mainly introduces the experiments related to the above content as supplementary explanation. First, based on the preliminary experiments, the motion and characteristics of RWT passive gait were demonstrated, which supported the theory of morphological transition. Second, experiments were conducted on dynamic gait controlled by MBC, which successfully proved that posture transition based on morphology is feasible, and a stable limit cycle gait was achieved.

Chapter 7 : Summarize the dissertation and lead to the next work.

Chapter 2

Passive Dynamic Modeling of RWT

2.1 Overview

In the field of robotics, a minimal model, also known as a simple model, refers to a model that only considers the most basic characteristics and functions of a robot, while ignoring other complex factors and influences. Minimal models generally have the following significance:

1. Studying the essence of robots: Minimal models can help us delve deeper into the essence of robots, explore the most basic kinematic and dynamic laws, and reveal the principles and mechanisms behind robot behavior.

2. Simplifying problems: Minimal models can help us simplify problems, reduce research difficulties, quickly verify theoretical hypotheses, and find solutions and directions for problem-solving.

3. Identifying problems: Minimal models can help us identify key points and bottlenecks in robot problems, enabling us to focus on solving the most critical problems.

4. Improving efficiency: Minimal models can help us improve the efficiency and stability of robot control and motion planning algorithms, thereby improving robot performance and precision.

Inspired by the minimal model, rimless wheel and utilizing tensegrity structures, this study proposes a planar Rimless-Wheel-Like Tensegrity Robot (RTW) model as the minimal mobile model in robotics morphology. First, the dynamic model of the RTW is presented, which

considers both single-legged support phase (SSP) and multi-legged support phase(MSP), and provides corresponding constraint conditions. Unlike the Rimless Wheel model, the landing collision of the RTW is based on the swing leg's own motion rather than the assumption that the swing leg has minimal mass and is judged by the touching angle. Normally, collisions in soft structures are considered to be elastic collisions, resulting in extremely small energy loss. However, due to the unique structure of the RTW, the collision between the swing leg and the ground is a inelastic collision, which reasonably simulates the MSP of animals. In addition, the strings connecting the legs in the RTW model also alter the model's dynamic characteristics, and the structure's rigidity or softness maps different morphologies, thus achieving different optimal modes of movement.

The proposed minimal model and corresponding passive dynamic modeling method not only provide a method and direction for establishing mathematical models of tensegrity robots, but also provide an academic research object for robotics morphology.

2.2 Mathematical Modeling

2.2.1 Introduction of RWT

The simplest spatial network structure of tensegrity can be achieved by fixing two rods with four strings. However, according to the research on the passive walking of the RW, the angle between the legs when the swing leg lands should be less than 90 degrees to ensure that the kinetic energy caused by the collision is not completely lost, thereby ensuring continuous walking. Therefore, this study uses a three-rods structure as the minimal model.

As shown in Figure 2.1, it consists of three rods, namely, Leg A, Leg B and Leg C, connected by six mass-less elastic strings. The major design parameters and Descriptions of the robot are listed in Table 2.1. It is assumed that there is no sliding behavior at the grounding point/points.

2.2.2 Equation of motion

Let $\boldsymbol{q} = \begin{bmatrix} x_a & z_a & \theta_a & x_b & z_b & \theta_b & x_c & z_c & \theta_c \end{bmatrix}^{\mathrm{T}}$ be the generalized coordinate vector, the robot equation of motion then becomes:

$$\boldsymbol{M}\ddot{\boldsymbol{q}} + \boldsymbol{h} = \boldsymbol{F}_{\mathrm{con}} + \boldsymbol{F}_{\mathrm{cou}}, \tag{2.1}$$

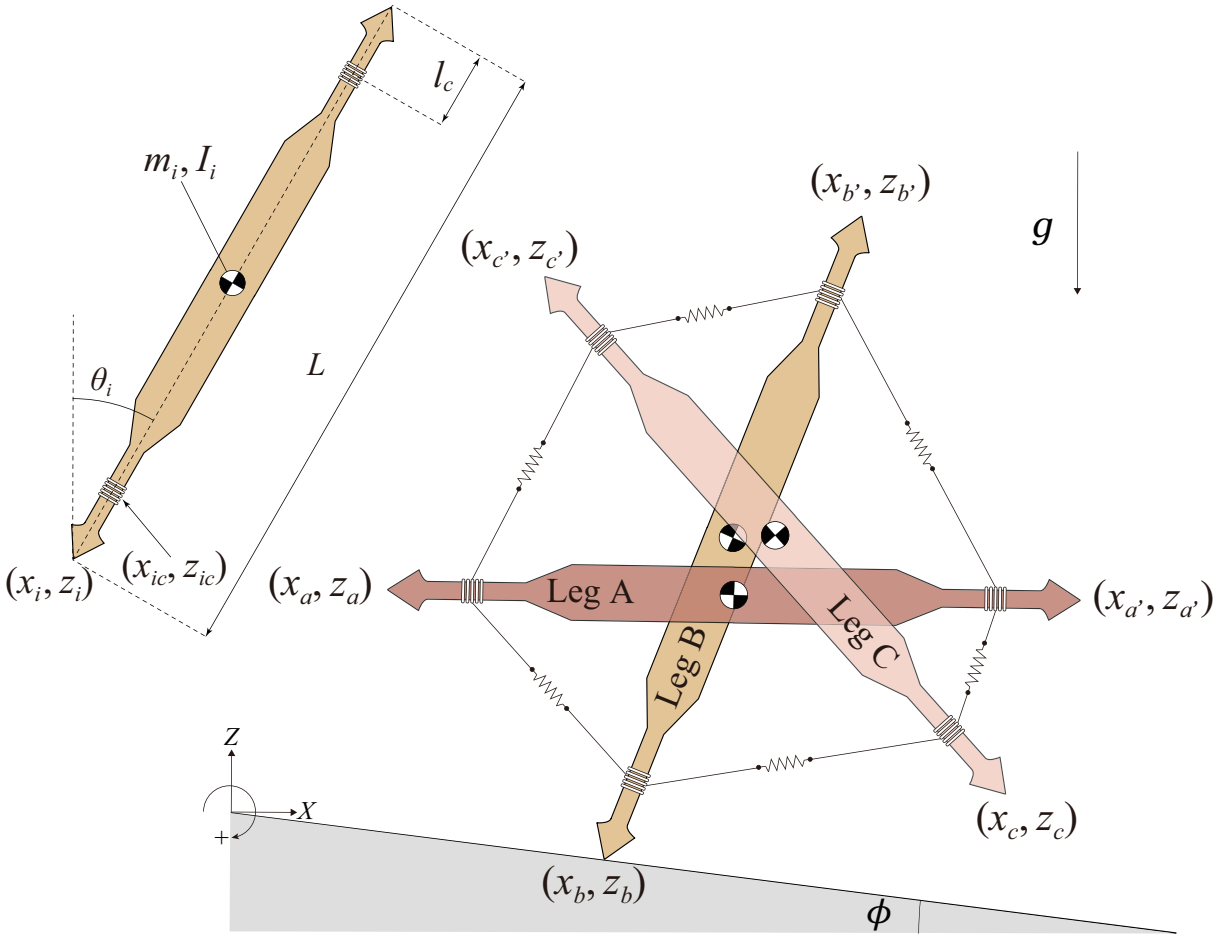

Figure 2.1: Mathematical model of RWT on downhill

where $\boldsymbol{M}$ represents the inertia matrix, $\boldsymbol{h}$ represents the combination of central force, Coriolis force and gravity terms. $\boldsymbol{F}_{\text{con}}$ is the constraint forces term and $\boldsymbol{F}_{\text{cou}}$ is the coupled internal elastics term.

2.2.3 Coupled internal elastics

The dynamics of legs are coupled through six mass-less elastic strings. In terms of coupling tension, we can express it as follows:

$$\boldsymbol{F}_{\text{cou}} = \sum_{i=1}^{12} \boldsymbol{J}_n^{\mathrm{T}} \boldsymbol{f}_n, \tag{2.2}$$

where $\boldsymbol{f}_n, n \in [1, 12]$ represents the force acting on every connection point in counterclockwise order that starts from the connection point (x_{ac}, z_{ac}), and $\boldsymbol{J}_n$, $n \in [1, 12]$ is its corresponding Jacobian matrix.

What can be difficult to understand is that there are 12 forces involved here. With 6 strings present, each string exerts an equal but opposite force on the two connecting points in different directions. The description is as follows:

$$\boldsymbol{f}_{2m} = \boldsymbol{f}_{2m-1},\ m \in [1, 6]. \tag{2.3}$$

Taking $\boldsymbol{J}_1^{\mathrm{T}} \boldsymbol{f}_1$ as an example, we can express the details of it as follows:

$$\boldsymbol{J}_1^{\mathrm{T}} \boldsymbol{f}_1 = \boldsymbol{J}_1^{\mathrm{T}} \boldsymbol{d}_{ab} f_{ab}, \tag{2.4}$$

where

$$\boldsymbol{J}_1 = \begin{bmatrix} 1 & 0 & l_c \cos\theta_a & 0 & 0 & 0 & 0 & 0 & 0 \\ 0 & 1 & -l_c \sin\theta_a & 0 & 0 & 0 & 0 & 0 & 0 \end{bmatrix}, \tag{2.5}$$

and $\boldsymbol{d}_{ab}$ represents the direction vector from (x_{ac}, z_{ac}) to (x_{bc}, z_{bc}):

$$\boldsymbol{d}_{ab} = \boldsymbol{S}_{ab} / D_{ab}. \tag{2.6}$$

Here,

$$\boldsymbol{S}_{ab} := \begin{bmatrix} x_{bc} - x_{ac} \\ z_{bc} - z_{ac} \end{bmatrix}, \tag{2.7}$$

$$D_{ab} := \sqrt{(x_{bc} - x_{ac})^2 + (z_{bc} - z_{ac})^2}. \tag{2.8}$$

Table 2.1: Configuration of robot

Symbol	Unit	Description
$m_i, i \in [a, b, c]$	kg	Weight of each leg
$I_i, i \in [a, b, c]$	kg·m^2	Inertia moment of each leg
L	m	Length of each leg
l_c	m	Length between connection point and tip point of each leg
$(x_i, z_i), i \in [a, b, c]$	m	Coordinates of each leg
$(x_{ic}, z_{ic}), i \in [a, b, c]$	m	Connection point on each leg
$\theta_i, i \in [a, b, c]$	rad	Angle to the vertical of each leg
ϕ	rad	Angle of gentle downhill

Tension occurs only when the distance between adjacent connection points exceeds the natural length of the elastic string. To realize such a both-side behavior and calculation continuity, we adopt

$$\chi_{ab} = 1/(1 + e^{-\epsilon(D_{ab}-L_n)}), \tag{2.9}$$

as a step function, where ϵ is a large dimensionless constant and L_n [m] is the natural length of elastic string. By approximating it as mass-spring-damper system, the magnitude of tension f_{ab} is determined as:

$$f_{ab} = \chi_{ab}\left(k(D_{ab} - L_n) + c\boldsymbol{V}_{ab}^{\mathrm{T}}\boldsymbol{d}_{ab}\right), \tag{2.10}$$

where

$$\boldsymbol{V}_{ab} := \begin{bmatrix} \dot{x}_{bc} - \dot{x}_{ac} \\ \dot{z}_{bc} - \dot{z}_{ac} \end{bmatrix}, \tag{2.11}$$

and k [N/m] and c [N·s/m] are coefficients of elasticity and viscosity respectively. In addition, the coefficient c is also used to represent the energy consumption of the system due to air resistance, internal friction and some others. $\boldsymbol{V}_{ab}^{\mathrm{T}}\boldsymbol{d}_{ab}$ is the mathematically organized form representing the difference in velocity in any direction projected onto the string, giving the magnitude of the projection.

Then the coupling tensions can be organized as follows:

$$\boldsymbol{F}_{\mathrm{cou}} = \boldsymbol{J}^{\mathrm{T}}\boldsymbol{D}\boldsymbol{T}\boldsymbol{f}, \tag{2.12}$$

where the details of the collection of Jacobian matrices $\boldsymbol{J}^{\mathrm{T}} \in \mathbb{R}^{9\times 24}$, the collection of direction vectors $\boldsymbol{D} \in \mathbb{R}^{24\times 12}$, the transformation matrix $\boldsymbol{T} \in \mathbb{R}^{12\times 6}$ and the collection of tensile force $\boldsymbol{f} \in \mathbb{R}^{6}$, as follows:

$$\boldsymbol{J}^{\mathrm{T}} = \begin{bmatrix} \boldsymbol{J}_1^{\mathrm{T}} & \boldsymbol{J}_2^{\mathrm{T}} & \cdots & \boldsymbol{J}_{12}^{\mathrm{T}} \end{bmatrix},$$

$$\boldsymbol{D} = \begin{bmatrix} \boldsymbol{d}_{ab} & \boldsymbol{0} & \cdots & \boldsymbol{0} \\ \boldsymbol{d}_{ba} & \boldsymbol{0} & \cdots & \boldsymbol{0} \\ \boldsymbol{0} & \boldsymbol{d}_{bc} & \cdots & \boldsymbol{0} \\ \boldsymbol{0} & \boldsymbol{d}_{cb} & \cdots & \boldsymbol{0} \\ \vdots & \vdots & \ddots & \vdots \\ \boldsymbol{0} & \cdots & \boldsymbol{0} & \boldsymbol{d}_{c'a} \\ \boldsymbol{0} & \cdots & \boldsymbol{0} & \boldsymbol{d}_{ac'} \end{bmatrix}, \quad \boldsymbol{T} = \begin{bmatrix} 1 & 0 & \cdots & 0 \\ 1 & 0 & \cdots & 0 \\ 0 & 1 & \cdots & 0 \\ 0 & 1 & \cdots & 0 \\ \vdots & \vdots & \ddots & \vdots \\ 0 & \cdots & 0 & 1 \\ 0 & \cdots & 0 & 1 \end{bmatrix}, \quad \boldsymbol{f} = \begin{bmatrix} f_{ab} \\ f_{bc} \\ \vdots \\ f_{c'a} \end{bmatrix}. \tag{2.13}$$

2.2.4 MSP and constraints

The corresponding gaits of RWT can be divided as: TSP, DSP, SSP, and fly, namely NSP.

None-legged Support Phase (NSP)

The robot equation of motion is:

$$\boldsymbol{M}\ddot{\boldsymbol{q}} + \boldsymbol{h} = \boldsymbol{F}_{\text{cou}}, \tag{2.14}$$

where $\boldsymbol{F}_{\text{con}} = \boldsymbol{0}$ in Eq. 2.1 that means there are no constraint forces from the ground.

Single-legged Support Phase (SSP)

The constraint force between the robot and the ground is generated when the robot interacts with the ground. For computational uniformity, during SSP, Leg C is guaranteed to be the collision leg, and Leg B is defined as the support leg. Then the equation of motion becomes:

$$\boldsymbol{M}\ddot{\boldsymbol{q}} + \boldsymbol{h} = \boldsymbol{J}_b^{\mathrm{T}}\boldsymbol{\lambda}_b + \boldsymbol{F}_{\text{cou}}, \tag{2.15}$$

By considering constraint forces term $\boldsymbol{F}_{\text{con}} := \boldsymbol{J}_b^{\mathrm{T}}\boldsymbol{\lambda}_b$ in Eq. 2.1, where $\boldsymbol{J}_b$ is the Jacobian matrix for holonomic constraints at grounding point (x_b, z_b) and $\boldsymbol{\lambda}_b$ is the constraint forces vector. The grounding point is fixed based on the assumption of no sliding, and the constraint conditions are shown as follows:

$$\dot{x}_b = 0, \quad \dot{z}_b = 0. \tag{2.16}$$

Accordingly, the constraint Jacobian matrix $\boldsymbol{J}_b$ by Eq. (2.16) can be summarized as:

$$\boldsymbol{J}_b\dot{\boldsymbol{q}} = \begin{bmatrix} 0 & 0 & 0 & 1 & 0 & 0 & 0 & 0 & 0 \\ 0 & 0 & 0 & 0 & 1 & 0 & 0 & 0 & 0 \end{bmatrix} \dot{\boldsymbol{q}} = \boldsymbol{0}_{2\times 1}. \tag{2.17}$$

The time derivative of Eq. (2.17) is

$$\boldsymbol{J}_b\ddot{\boldsymbol{q}} = \boldsymbol{0}_{2\times 1}. \tag{2.18}$$

By solving Eq. (2.15) with the Eq. (2.18) simultaneously, the constraint force vector $\boldsymbol{\lambda}_b$ can be obtained:

$$\boldsymbol{\lambda}_b = -\boldsymbol{X}_b^{-1}\boldsymbol{J}_b\boldsymbol{M}^{-1}(\boldsymbol{F}_{\text{cou}} - \boldsymbol{h}), \tag{2.19}$$

where $\boldsymbol{X}_b := \boldsymbol{J}_b\boldsymbol{M}^{-1}\boldsymbol{J}_b^{\mathrm{T}}$.

Double-legged Support Phase (DSP)

The equation of motion is

$$\boldsymbol{M}\ddot{\boldsymbol{q}} + \boldsymbol{h} = \sum_{i=a,b} \boldsymbol{J}_i^{\mathrm{T}} \boldsymbol{\lambda}_i + \boldsymbol{F}_{\mathrm{cou}}, \tag{2.20}$$

by considering the (x_a, z_a) and (x_b, z_b) are grounding points simultaneously. With the similar manner to solve $\boldsymbol{\lambda_b}$ in Eq. (2.19), We can derive $\boldsymbol{\lambda}_a$ and $\boldsymbol{\lambda}_b$ as

$$\begin{aligned} \boldsymbol{\lambda}_a &= -\boldsymbol{X}_a^{-1}\boldsymbol{X}_{ab}\boldsymbol{\lambda}_b - \boldsymbol{X}_a^{-1}\boldsymbol{J}_a\boldsymbol{M}^{-1}(\boldsymbol{F}_{\mathrm{cou}} - \boldsymbol{h}), \\ \boldsymbol{\lambda}_b &= -\boldsymbol{X}_b^{-1}\boldsymbol{X}_{ba}\boldsymbol{\lambda}_a - \boldsymbol{X}_b^{-1}\boldsymbol{J}_b\boldsymbol{M}^{-1}(\boldsymbol{F}_{\mathrm{cou}} - \boldsymbol{h}), \end{aligned} \tag{2.21}$$

where $\boldsymbol{X}_a := \boldsymbol{J}_a\boldsymbol{M}^{-1}\boldsymbol{J}_a^{\mathrm{T}}$, $\boldsymbol{X}_{ab} := \boldsymbol{J}_a\boldsymbol{M}^{-1}\boldsymbol{J}_b^{\mathrm{T}}$, $\boldsymbol{X}_{ba} := \boldsymbol{J}_b\boldsymbol{M}^{-1}\boldsymbol{J}_a^{\mathrm{T}}$, and

$$\boldsymbol{J}_a = \begin{bmatrix} 1 & 0 & 0 & 0 & 0 & 0 & 0 & 0 & 0 \\ 0 & 1 & 0 & 0 & 0 & 0 & 0 & 0 & 0 \end{bmatrix}. \tag{2.22}$$

The coordinates of the legs are independent of each other, as shown in $\boldsymbol{q}$. Therefore, the sparse matrices $\boldsymbol{J}_a$ and $\boldsymbol{J}_b$ result in null $\boldsymbol{X}_{ab}$ and $\boldsymbol{X}_{ba}$ matrices, i.e., $\boldsymbol{X}_{ab} = \boldsymbol{0}$ and $\boldsymbol{X}_{ba} = \boldsymbol{0}$. Consequently, Eq. (2.21) becomes:

$$\boldsymbol{\lambda}_a = -\boldsymbol{X}_a^{-1}\boldsymbol{J}_a\boldsymbol{M}^{-1}(\boldsymbol{F}_{\mathrm{cou}} - \boldsymbol{h}), \tag{2.23}$$

$$\boldsymbol{\lambda}_b = -\boldsymbol{X}_b^{-1}\boldsymbol{J}_b\boldsymbol{M}^{-1}(\boldsymbol{F}_{\mathrm{cou}} - \boldsymbol{h}), \tag{2.24}$$

that is similar to the SSP.

In general, during the DSP, the constraint forces from the ground on each foot are coupled, and a third constraint condition is required to decouple them. For example, the micro deformation of the legs can be considered to introduce force balance, or the constraint of both feet can be viewed as a whole and introduced into the Zero moment point(ZMP) formula. The derivation of Eq. (2.21) proves that the model proposed in this study can achieve decoupling more conveniently, which is also one of the features of RWT.

Triple-legged Support Phase (TSP)

The equation of motion is

$$\boldsymbol{M}\ddot{\boldsymbol{q}} + \boldsymbol{h} = \sum_{i=a,b,c'} \boldsymbol{J}_i^{\mathrm{T}} \boldsymbol{\lambda}_i + \boldsymbol{F}_{\mathrm{cou}}. \tag{2.25}$$

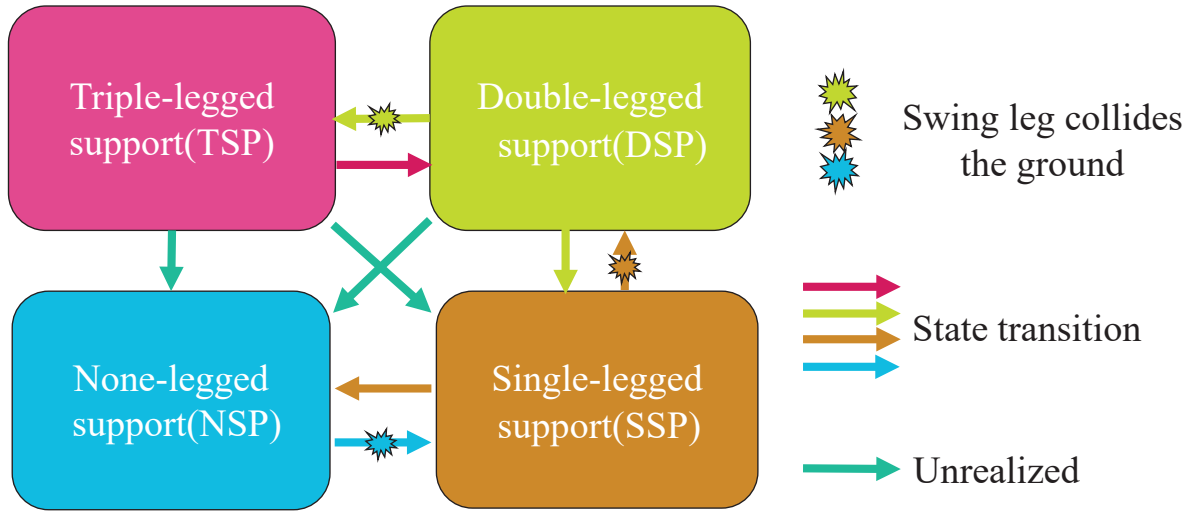

Figure 2.2: Gait transition of RWT locomotion

The constraint forces vector $\boldsymbol{\lambda}_i$, $i \in [a, b, c']$ can be explained as follows:

$$\boldsymbol{\lambda}_i = -\boldsymbol{X}_i^{-1}\boldsymbol{J}_i\boldsymbol{M}^{-1}(\boldsymbol{F}_{\text{cou}} - \boldsymbol{h}), \tag{2.26}$$

where $\boldsymbol{X}_i := \boldsymbol{J}_i\boldsymbol{M}^{-1}\boldsymbol{J}_i^{\mathrm{T}}$ and

$$\boldsymbol{J}_{c'} = \begin{bmatrix} 0\ 0\ 0\ 0\ 0\ 0\ 1\ 0 & L\cos\theta_c \\ 0\ 0\ 0\ 0\ 0\ 0\ 0\ 1 & -L\sin\theta_c \end{bmatrix}. \tag{2.27}$$

2.2.5 Gait transition and collision

The walking process of a robot is a hybrid system composed of both continuous and discrete events. During each step, the state undergoes continuous changes, but when the swing leg collides inelastically with the ground, energy is lost and kinetic energy decreases. This sudden change in velocity triggers a discrete event, leading to a state transition.

Moreover, the continuous events in the system, i.e., the state within each step, are continuous and segmented. When the robot is supported by multiple legs, lifting one leg causes a change in the corresponding equations of motions. Therefore, the walking process of a robot is a complex interplay between continuous and discrete events, which must be carefully considered in modeling and control design for optimal performance.This segmentation and discreteness are illustrated in Figure 2.2.

During the transition from NSP to TSP, state changes are accompanied by collisions. When the swing leg collides with the ground, the inelastic collision causes a sudden decrease in its

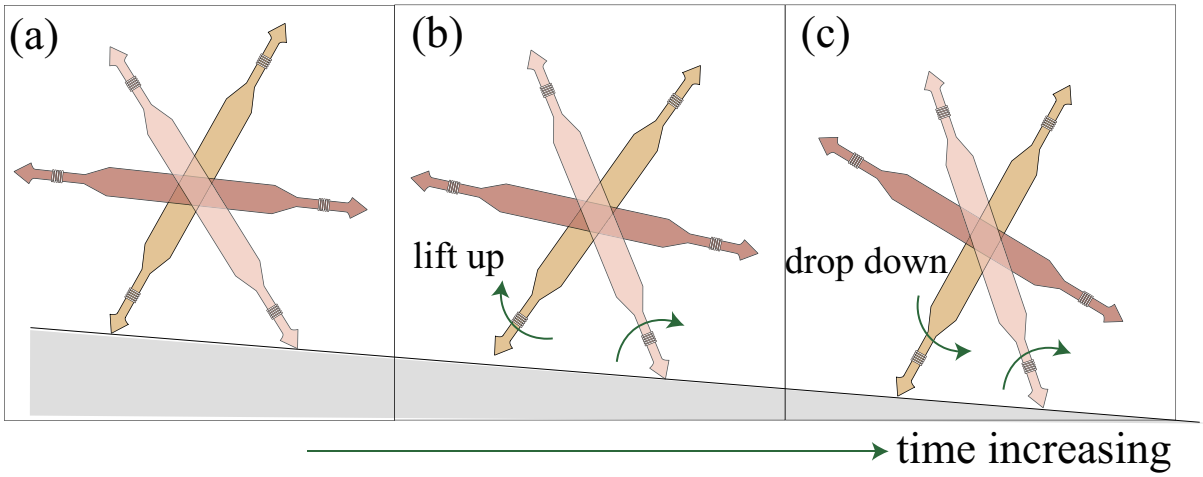

Figure 2.3: Backward re-collision schematic

velocity. However, since the stance leg and the swing leg are independent of each other, the collision does not instantly change the state of the stance leg. Therefore, after the collision, the swing leg remains in contact with the ground, leading to an increase in the number of stance legs.

Conversely, during the transition from TSP to NSP, the state does not change abruptly. When the constraint force exerted by the ground on the swing leg becomes less than zero, the swing leg will lift, and the corresponding equation of motion will be replaced. This segmentation does not affect the continuity of the state.

According to the Eq. (2.19), Eq. (2.24) and Eq. (2.26), the ground reaction force f_{i_support} [N], $i \in [a, b, c']$ can be obtained as:

$$f_{i\_\text{support}} = \left[\sin\phi \ \cos\phi\right] \boldsymbol{\lambda}_i. \tag{2.28}$$

The triggering condition for the stance leg to become the swing leg is $f_{i\_\text{support}} < 0, i \in [a, b, c']$, while the triggering condition for the swing leg to become the stance leg is $z_i < Z_{\text{land}}, i \in [a, b, c']$, where Z_{land} is the corresponding ground height. Due to the unpredictability of nonlinear motion, it is possible for the rear legs to re-collide with the ground as soon as they leave the ground as explained in Figure 2.3. Here, Figure 2.3 (a) represents the initial state, as forward movement (to the right) occurs, the swing leg lifts as shown in Figure 2.3 (b), and based on its own elastic potential energy, its movement becomes nonlinear and unpredictable. It may touch the ground again after being lifted, as shown in Figure 2.3 (c). Such a phenomenon of repeated collision is easy to overlook and inevitable.

It is important to note that despite the robot's softness characteristics, the collision between the legs and the ground is inelastic, and the collision equation is as follows:

$$\boldsymbol{M}\dot{\boldsymbol{q}}^{+} = \boldsymbol{M}\dot{\boldsymbol{q}}^{-} + \boldsymbol{J}_c^{\mathrm{T}}\boldsymbol{\lambda}_c, \tag{2.29}$$

$$\boldsymbol{J}_c\dot{\boldsymbol{q}}^{+} = \boldsymbol{0}_{2\times 1}, \tag{2.30}$$

where Leg C is the collision leg as mentioned and the superscripts "−" and "+" denote the instances immediately before and after impact this collision, respectively. By solving Eqs. (2.29) and (2.30) simultaneously, $\dot{\boldsymbol{q}}^{+}$ is given by:

$$\dot{\boldsymbol{q}}^{+} = \left(\boldsymbol{I}_9 - \boldsymbol{M}^{-1}\boldsymbol{J}_c^{\mathrm{T}}\boldsymbol{X}_c^{-1}\boldsymbol{J}_c\right)\dot{\boldsymbol{q}}^{-}, \tag{2.31}$$

where $\boldsymbol{X}_c := \boldsymbol{J}_c\boldsymbol{M}^{-1}\boldsymbol{J}_c^{\mathrm{T}}$.

2.3 Improvement of the Reality-based RWT Model

The advantages of minimal models lie in their ability to simplify problems and highlight the essence of problems. However, some real-world problems may be unexpectedly ignored due to the simplification of the model. In the case of robot locomotion, the reaction force of the ground plays a vital role. Different foot shapes can lead to different motion performance, and the optimal solution is often not just point contact. Therefore, it is necessary to consider a smoother ground contact approach. Additionally, the influence of friction is also significant, and how to walk on a smooth surface cannot be studied by the above model. Thus, this section will transform the above model to make the RWT model more general.

2.3.1 Semicircular feet

As shown in Figure 2.4, the RTW that has semicircular feet with radius R [m] and walks on a gentle slope of ϕ [rad]. Compared to the previous model definition, it should be noted here that $(x_{ig}, z_{ig}), i \in [a, b, c]$ represents the grounding point of different feet, while $(x_i', z_i'), i \in [a, b, c]$ represents the corresponding center of the circle.

After the modification of the foot shape, the constraint forces $\boldsymbol{F}_{\mathrm{con}}$ in Eq. 2.1 exerted on the robot also changes. Since each leg is independent as proven previously, the ground reaction force on each leg can be calculated separately and then added together. This decoupling property

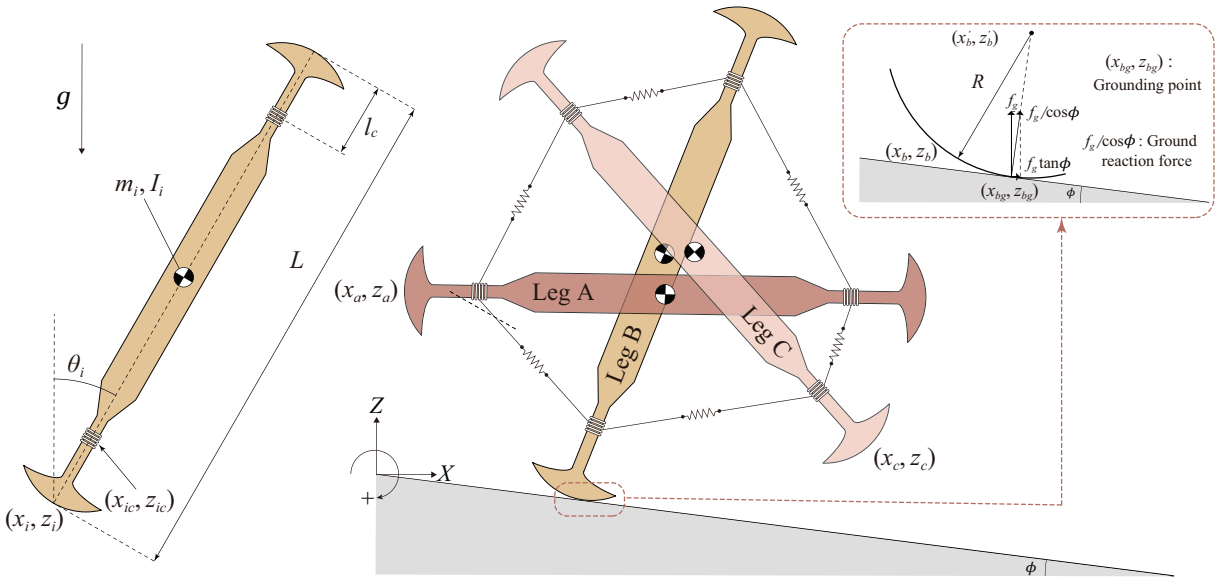

Figure 2.4: Mathematical model of RWT with semicircular feet

of the ground reaction force calculation simplifies the computation. Here, SSP is taken as an example, and the calculation method for MSP is similar.

Constraint Forces

The velocity constraint condition of grounding point (x_{bg}, z_{bg}) of stance leg, Leg B is defined as follows:

$$\begin{bmatrix} \dot{x}_{bg} \\ \dot{z}_{bg} \end{bmatrix} = \begin{bmatrix} -R\dot{\theta}_b \cos\ \phi \\ R\dot{\theta}_b \sin\ \phi \end{bmatrix}. \tag{2.32}$$

The coordinates of grounding point is shown below:

$$\begin{bmatrix} x_{bg} \\ z_{bg} \end{bmatrix} = \begin{bmatrix} x_b + R\sin\theta_b - R\sin\phi \\ z_b + R\cos\theta_b - R\cos\phi \end{bmatrix}. \tag{2.33}$$

The velocity of the grounding point can be obtained by differentiating Eq. (2.33) as:

$$\frac{\mathrm{d}}{\mathrm{d}t}\begin{bmatrix} x_{bg} \\ z_{bg} \end{bmatrix} = \frac{\mathrm{d}}{\mathrm{d}t}\begin{bmatrix} x_b' \\ z_b' \end{bmatrix} = \begin{bmatrix} \dot{x_b} + R\dot{\theta_b}\cos\theta_b \\ \dot{z_b} - R\dot{\theta_b}\sin\theta_b \end{bmatrix}. \tag{2.34}$$

By substituting Eq. (2.34) into Eq. (2.32), the holonomic constraint condition can be obtained as

$$\begin{bmatrix} \dot{x_b} + R\dot{\theta_b}\cos\theta_b - R\dot{\theta_b}\cos\ \phi \\ \dot{z_b} - R\dot{\theta_b}\sin\theta_b + R\dot{\theta_b}\sin\ \phi \end{bmatrix} = \mathbf{0}. \tag{2.35}$$

Then, it can be further arranged as follows:

$$\boldsymbol{J}_{bg} = \begin{bmatrix} \mathbf{0}_{1\times3} & 1 & 0 & R\left(\cos\theta_b - \cos\phi\right) & \mathbf{0}_{1\times3} \\ \mathbf{0}_{1\times3} & 0 & 1 & -R\left(\sin\theta_b - \sin\phi\right) & \mathbf{0}_{1\times3} \end{bmatrix}, \tag{2.36}$$

$$\boldsymbol{J}_{bg}\dot{\boldsymbol{q}} = \mathbf{0}. \tag{2.37}$$

By differentiating Eq. (2.37) with respect to time, we get:

$$\boldsymbol{J}_{bg}\ddot{\boldsymbol{q}} + \dot{\boldsymbol{J}}_{bg}\dot{\boldsymbol{q}} = \mathbf{0}. \tag{2.38}$$

Therefore, the constraint force $\boldsymbol{\lambda}_{bg}$ can be obtained by substituting the Eq. (2.38) into the equation of motion for the SSP:

$$\boldsymbol{\lambda}_{bg} = \boldsymbol{X}_{bg}^{-1}\left(\boldsymbol{J}_{bg}\boldsymbol{M}^{-1}\left(\boldsymbol{h} - \boldsymbol{J}\boldsymbol{F}_{\text{cou}}\right) - \dot{\boldsymbol{J}}_{bg}\dot{\boldsymbol{q}}\right), \tag{2.39}$$

where $\boldsymbol{X}_{bg} := \boldsymbol{J}_{bg}\boldsymbol{M}^{-1}\boldsymbol{J}_{bg}^{\mathrm{T}}$. Then The constraint forces $\boldsymbol{F}_{\text{con}}$ in Eq. 2.1 in DSP and TSP can be defined as follows:

$$\boldsymbol{F}_{\text{con}} = \sum_{i=a,b} \boldsymbol{J}_{ig}^{\mathrm{T}}\boldsymbol{\lambda}_{ig} \tag{2.40}$$

or

$$\boldsymbol{F}_{\text{con}} = \sum_{i=a,b,c'} \boldsymbol{J}_{ig}^{\mathrm{T}}\boldsymbol{\lambda}_{ig}. \tag{2.41}$$

Collision Equation

The semicircular foot also changes the contact point during collision, so the Jacobian matrix $\boldsymbol{J}_c$ in Eq. 2.30 will also change to

$$\boldsymbol{J}_c = \begin{bmatrix} \mathbf{0}_{1\times6} & 1 & 0 & R\left(\cos\theta_b - \cos\phi\right) \\ \mathbf{0}_{1\times6} & 0 & 1 & -R\left(\sin\theta_b - \sin\phi\right) \end{bmatrix}. \tag{2.42}$$

2.3.2 Frictional constraints

During walking, the frictional force between the ground and the feet is an important environmental factor that cannot be ignored. Previous research often regarded frictional force as external interference and attempted to minimize its impact by improving the robustness of the control system. However, utilizing frictional force can also bring many benefits. For example, in some cases, utilizing the frictional force of the ground can help the robot walk more stably and improve its walking efficiency and performance. Therefore, this section mainly introduces the mathematical modeling of the system under consideration of frictional force.

Equation of Motion

Taking single leg support as an example, the equations of motion can be written as follows.

$$\boldsymbol{M}\ddot{\boldsymbol{q}} + \boldsymbol{h} = \boldsymbol{J}_{bf}^{\mathrm{T}} f_g + \boldsymbol{J}_{\mu b}^{\mathrm{T}} f_g + \boldsymbol{F}_{\mathrm{cou}}. \tag{2.43}$$

Here, $\boldsymbol{F}_{\mathrm{con}} := \boldsymbol{J}_{bf}^{\mathrm{T}} f_g + \boldsymbol{J}_{\mu b}^{\mathrm{T}} f_g$ is the holonomic constraint force vector and f_g is the reaction force in the vertical direction. Then, the reaction force on the contact surface vertical is $f_g/\cos\phi$. $\boldsymbol{J}_{bf}^{\mathrm{T}} f_g$ constrains the grounding point to move along the slope, while $\boldsymbol{J}_{\mu b}^{\mathrm{T}} f_g$ provides the corresponding friction force.

Constraint Forces

The point foot model is a special case of the arc foot model with a radius R of 0. Therefore, we use the arc foot model to model friction in order to ensure generality.

The velocity constraint condition of grounding point (x_{bc}, z_{bc}) of leg B is defined as follows:

$$\dot{z}_{bg} = -\tan\phi \cdot \dot{x}_{bg}. \tag{2.44}$$

The coordinates of grounding point and the velocity of it can be obtained from Eq. (2.33) and Eq. (2.34). By substituting Eq. (2.34) into Eq. (2.44), the holonomic constraint condition can be obtained as

$$\dot{x}_b \tan\phi + \dot{z}_b + R\dot{\theta}_b \left(\cos\theta_b \tan\phi - \sin\theta_b\right) = 0. \tag{2.45}$$

Then, it can be further arranged as follows:

$$\boldsymbol{J}_{bf} = \left[\boldsymbol{0}_{1\times 3} \;\; \tan\phi \;\; 1 \;\; R\left(\cos\theta_b \tan\phi - \sin\phi\right) \;\; \boldsymbol{0}_{1\times 3}\right], \tag{2.46}$$

$$\boldsymbol{J}_{bf}\dot{\boldsymbol{q}} = 0. \tag{2.47}$$

By differentiating Eq. (2.47) with respect to time, we get:

$$\boldsymbol{J}_{bf}\ddot{\boldsymbol{q}} + \dot{\boldsymbol{J}}_{bf}\dot{\boldsymbol{q}} = 0. \tag{2.48}$$

Therefore, the constraint force f_g can be obtained by substituting the Eq. (2.48) into the equation of motion for the SSP:

$$f_g = X_{bf}^{-1}\left(\boldsymbol{J}_{bf}\boldsymbol{M}^{-1}\left(\boldsymbol{h} - \boldsymbol{F}_{\mathrm{cou}}\right) - \dot{\boldsymbol{J}}_{bf}\dot{\boldsymbol{q}}\right), \tag{2.49}$$

where $X_{bf} := \boldsymbol{J}_{bf}\boldsymbol{M}^{-1}\hat{\boldsymbol{J}}_b^{\mathrm{T}}$ and $\hat{\boldsymbol{J}}_b := \boldsymbol{J}_{bf} + \boldsymbol{J}_{\mu b}$.

Coulomb Friction Force

In the SSP, the Coulomb friction force f_b [N] that is applied to the support leg B can be defined by the following geometric relationships:

$$f_b = \mu \frac{f_g}{\cos \phi}. \tag{2.50}$$

The signed friction coefficient μ is determined by the contact point velocity as as follows:

$$\mu = -\mu_0 \tanh(\kappa V). \tag{2.51}$$

Here, V [m/s] is relative sliding speed and κ is a dimensionless parameter that adjusts the slope of μ around $V = 0$. Here, we use 'tanh()' to ensure the continuity of μ, so that it approaches 0 as V approaches 0. This not only makes the segmented and discrete μ continuous for mathematical convenience, but also reduces the integration cost in the computer's discrete cycle processing. When V approaches 0, a large μ value can cause the computer to repeatedly jump around the $V = 0$ point during the integration calculation, increasing the computational cost and possibly leading to integration divergence and failure. However, the continuous change generated by using 'tanh()' can reduce the stiffness of the differential equation, which will be specifically discussed in the next chapter on simulator design. Here, the sliding velocity to the stationary surface V [m/s] is specified as:

$$V = \frac{\dot{x}_b}{\cos \phi} - R\dot{\theta}_b. \tag{2.52}$$

It is important to note that friction forces have both rolling and sliding effects. Therefore, if the rolling effect is not considered, then it will result in a misunderstanding of the force acting on the central position of semicircular feet. Therefore, we use the following outer product approach to calculate $\boldsymbol{J}_{\mu b}$.

The three-dimension friction force vector is

$$\begin{bmatrix} \cos \phi \\ 0 \\ -\sin \phi \end{bmatrix} f_b = \begin{bmatrix} \mu \\ 0 \\ -\mu \tan \phi \end{bmatrix} \lambda_b. \tag{2.53}$$

Accordingly, the torque effect of θ_b is as follows:

$$\begin{bmatrix} x_{bg} - x_b \\ 0 \\ z_{bg} - z_b \end{bmatrix} \times \begin{bmatrix} \mu \\ 0 \\ -\mu \tan \phi \end{bmatrix} f_g = \begin{bmatrix} 0 \\ \mu R \left(\cos\left(\phi - \theta_b\right) - 1\right) / \cos \phi \\ 0 \end{bmatrix} f_g. \tag{2.54}$$

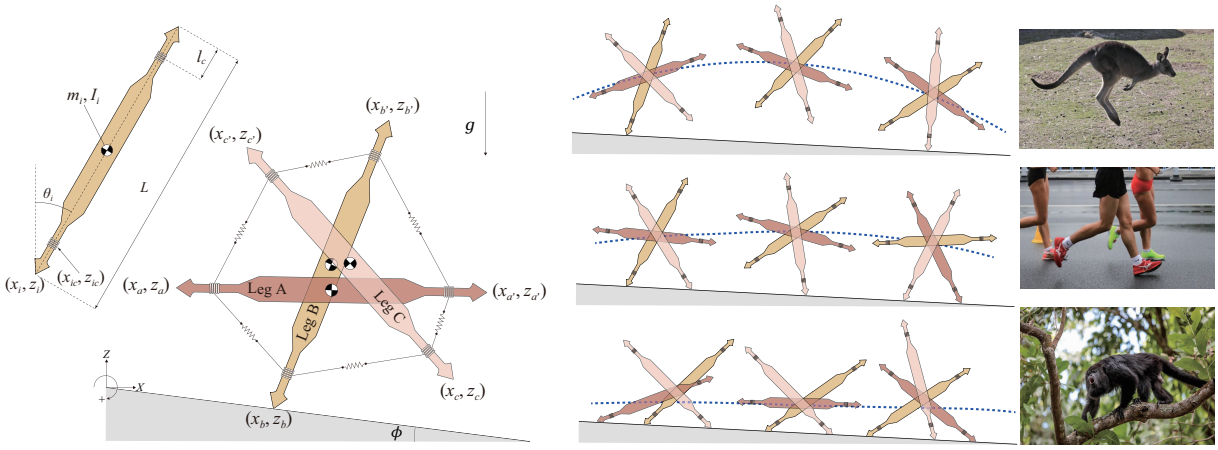

Figure 2.5: Three different morphologies, skipping, walking and crawling that corresponding to different COM positions during locomotion, each representing an independent dynamic property.

By summarizing Eq. (2.53) and Eq. (2.54), the Jacobian vector for Coulomb friction force can be calculated as:

$$\boldsymbol{J}_{\mu b}^{\mathrm{T}} f_g = \begin{bmatrix} \mathbf{0}_{3\times 1} \\ \mu \\ -\mu \tan\phi \\ \mu R\left(\cos\left(\phi - \theta_b\right) - 1\right)/\cos\phi \\ \mathbf{0}_{3\times 1} \end{bmatrix} f_g. \tag{2.55}$$

2.4 Summary and Discussions

The definition of morphology includes both structural characteristics and specific functions generated based on the current structure and shape. The morphology of robots is an effective direction for designing robots, which involves mechanical structure design, dynamic characteristic analysis, and other contents.

Due to the characteristics of tensegrity structures, they not only can simulate biological muscle tissue but also have unique properties such as lightness, toughness, and self-recovery, making them very suitable as the structure of robots.

This chapter proposes the minimal model of robot morphology based on tensegrity structures and provides corresponding dynamic modeling. Furthermore, for practical problems, ex-

panded structures and corresponding mathematical methods are presented.

First, this chapter provides a method for the dynamic modeling of tensegrity robots, which is a challenging problem. The method enables tensegrity robots to achieve high-precision and high-adaptation control based on mathematical models, thus highlighting the unique advantages of tensegrity robots. Second, as the minimal model of robot morphology, this model can not only achieve deformation characteristics by changing the relative positions of bars but also change the inherent dynamic characteristics by adjusting the elasticity coefficient of strings. Unlike structure, morphology is distinguished by whether the corresponding structure has specific functions. Modifying the elasticity and damping coefficients of strings can change the structural characteristics, thus achieving different motion modes such as skipping, walking, and crawling in different environments as shown in Figure 2.5.

As an example, structure of humans and chimpanzees is similar, but when running, humans use two feet while chimpanzees use four. This difference is not only due to the different proportions of limbs but also to the difference in muscle strength. Further, different muscle strength responds differently to body weight, and modifying the elasticity and damping coefficients of strings can simulate this response characteristic.

Based on this, the minimal model proposed in this chapter and its corresponding mathematical modeling can solve the dynamic modeling problem of tensegrity robots, enabling them to achieve high-speed, high-precision, and high-adaptation motion. In addition, this model can also serve as the minimal model of robot morphology, providing a platform for the study of robot morphology.

Chapter 3

Motion Simulation and Dynamic Characteristics Analysis of RWT

3.1 Overview

Robot motion simulation is an essential process for testing the performance of robots in a virtual environment without the need for physical prototypes. In recent years, it has become an essential tool for robotics research, design, and development. Several mainstream robot motion simulation tools are available, including Gazebo, V-REP, Webots, and ROS, each with unique features, advantages, and disadvantages.

Nevertheless, currently, mainstream simulators are based on their own built-in algorithms, such as motion computation and collision detection, which cannot be verified or modified, making it difficult to obtain rigorous and detailed motion results, especially for systems that are sensitive to initial conditions. Additionally, due to their encapsulation, users are unable to make better calls, and cannot embed them as tools into their current working platforms. Moreover, when verifying the motion characteristics of the minimal model, these simulators introduce many objective and realistic physical interferences, which have the opposite effect on exploring motion characteristics and can make it difficult to obtain corresponding theoretical conclusions.

This chapter presents the simulator design of RWT using MATLAB based on the mathematical model introduced in the previous chapter, and gives the corresponding analysis.

3.2 Simulator Design

In MATLAB, different ODE functions can be used to solve nonlinear differential equations, among which commonly used ones include ode45, ode23, ode113, ode15s, etc. The differences and advantages and disadvantages of these functions are as follows:

- ode45: This function uses the fourth-order Runge-Kutta method with adaptive step size and high accuracy, which can quickly solve most non-stiff and stiff differential equations. However, there may be difficulties in solving extremely stiff problems.
- ode23: This function uses the second-order Runge-Kutta method with adaptive step size, which is faster than ode45 but has slightly lower accuracy. It is suitable for solving some less stiff differential equations.
- ode113: This function uses a higher-order Runge-Kutta method and can more accurately solve very complex nonlinear differential equations, but the computation time is longer.
- ode15s: This function uses an implicit solver based on the Backward Differentiation Formula (BDF), which is suitable for solving extremely stiff differential equations. However, compared with other functions, the computation time is longer.

Stiff differential equations refer to a class of differential equations whose solutions change slowly. This is usually due to the presence of some terms that change rapidly and some terms that change slowly in the equation, which leads to numerical solution methods requiring very small step sizes during calculation, resulting in a huge computational load. Strictly speaking, stiff differential equations refer to equations in which the stability of the numerical solution is greatly affected and may even diverge if the step size is not small enough during the solving process.

For RWT, the existence of spring damping term on the string causes a decrease in its stiffness when the coefficient is too large. Additionally, due to its physical characteristics, the numerical solution of RWT does not diverge as the step size decreases but only affects the computation time. Therefore, considering these factors, the ode45 method is adopted in this study to solve the motion equation of RWT.

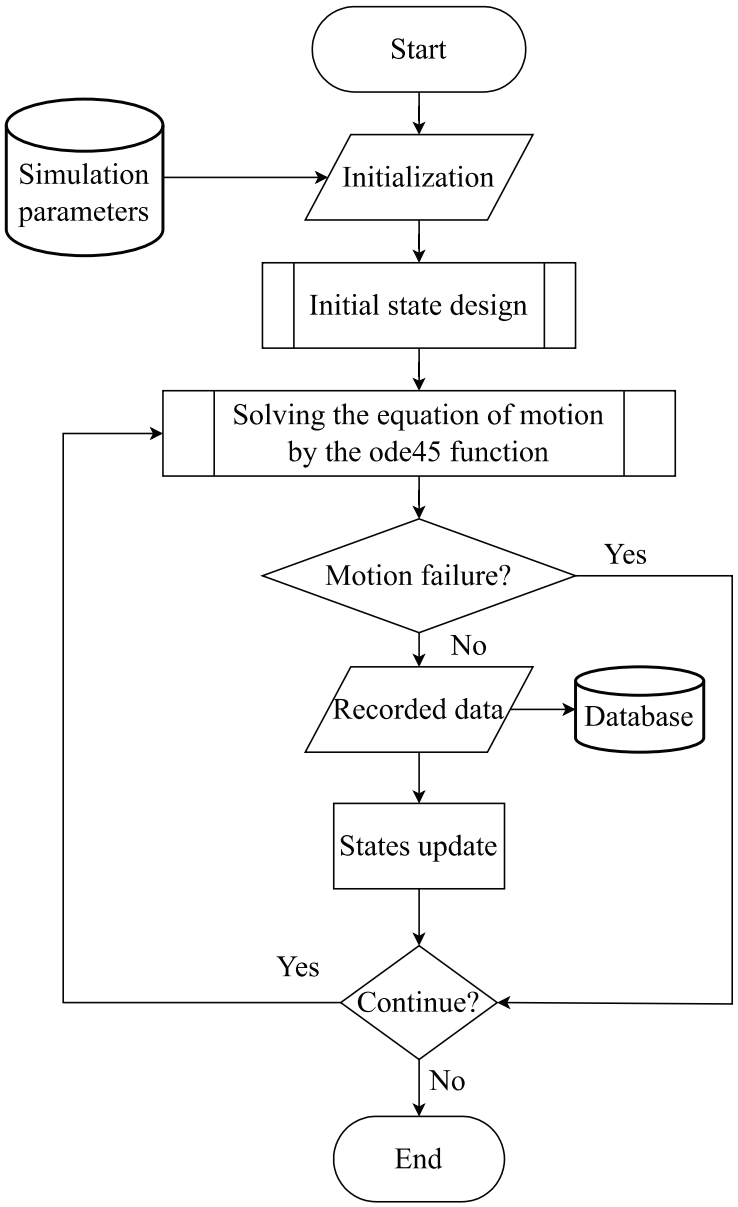

Figure 3.1: Flow chart of the main program of the simulator

3.2.1 Main program design

Figure 3.1 illustrates the flowchart of the main program. Upon program initiation, user-defined simulation parameters are first read for program initialization. Since ode45 is used as the primary function for solving differential equations, simulation parameters specific to ode45 must be set. The specific parameters are listed in Table 3.1.

Note that TimeEnd here refers to the maximum value of a single continuous time simulation, rather than the maximum time of the overall simulation. As legged locomotion is a hybrid system that involves discrete events, i.e., collisions, the total simulation time should be the

Table 3.1: Simulation parameters

Parameters	Value	Description
TimeStart	0	Simulation start time
dt	10^{-2}	Step length
TimeEnd	10	Simulation end time
RelTol	10^{-6}	An optional parameter that specifies the relative error tolerance for the solver. It controls the precision of the solver and defines the threshold for a solution to be considered ”accurate enough”. If the solver's relative error exceeds this threshold, it will attempt to adjust the step size to improve the accuracy of the solution. Therefore, lower values of ”RelTol” can improve the accuracy of the solver but may also increase computational cost and runtime.
AbsTol	10^{-6}	Same as 'RelTol'
Refine	6	An optional parameter that specifies the maximum refinement level of the internal solver used by ode45 at each time step. Specifically, it controls how finely the solver resolves the differential equations within each time step. Higher values of ”refine” can improve the accuracy of the solution but also increase computational cost and runtime.

accumulation of each step. The parameter settings here ensure that the error is less than 10 to the power of negative six at a time step of dt, thus ensuring the accuracy of the simulation.

3.2.2 Initial state design

In nonlinear systems systems, the initial state can affect the long-term behavior of the system, leading to a close correlation between the system's evolutionary path and its initial states. Even if the dynamic equations of the system are known, it is difficult to accurately predict the behavior of the system. This is because, in nonlinear systems, small perturbations or errors can lead to very different behaviors of the system, making the prediction results unreliable.

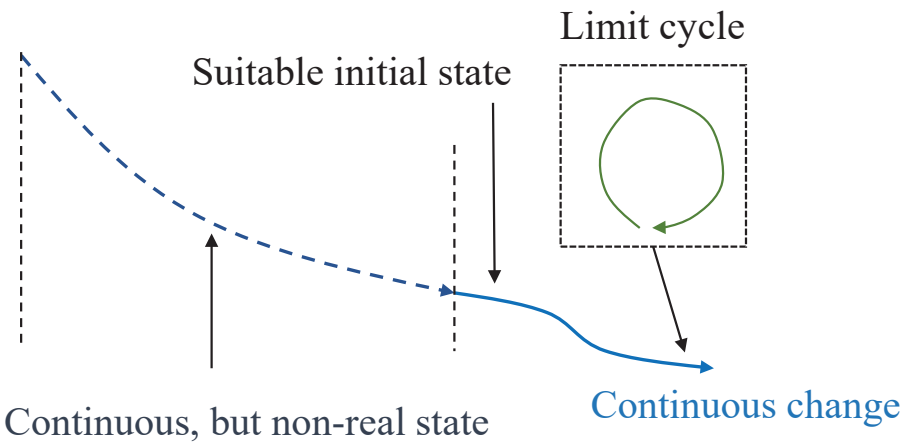

Figure 3.2: Concept map for finding the initial state

In addition, initial conditions can also affect the stability, controllability, and observability of the system. An unstable system may undergo significant changes under small variations of initial conditions, while an uncontrollable system may not be able to be controlled or adjusted as required. Similarly, if the state of the system cannot be determined by observation or measurement, the study and control of the system will also face great challenges.

Basin of attraction (BOA) refers to the region in a nonlinear system where the system will eventually converge to stable points or periodic orbits when evolving from certain initial states. Therefore, for initial states in this study relies on the system's basin of attraction, in order to find the most stable convergent state as the initial state of the system.

Figure 3.2 illustrates the concept of searching for the initial state. The blue line represents the robot's hybrid system, gradually converging within the BOA range, accompanied by discrete and segmented events as shown in Figure 2.2, eventually converging to a limit cycle. At this point, the stability is the highest, and it is the most suitable as the initial state for simulation. Therefore, the design of the initial state should search for the "suitable initial state" area indicated by the black arrow. This range is not small, and some reasonable physical initial states can satisfy it, such as standing on the ground with a little forward momentum. However, such initial states may not satisfy all physical structures. For RWT, when the string tension is different, the system's BOA also changes. The same initial state may not guarantee that it is within the BOA. Therefore, it is necessary to consider the "Continuous, but non-real state" area on the left dotted line.

Mathematically, the change of a motion equation is continuous, but considering the real sit-

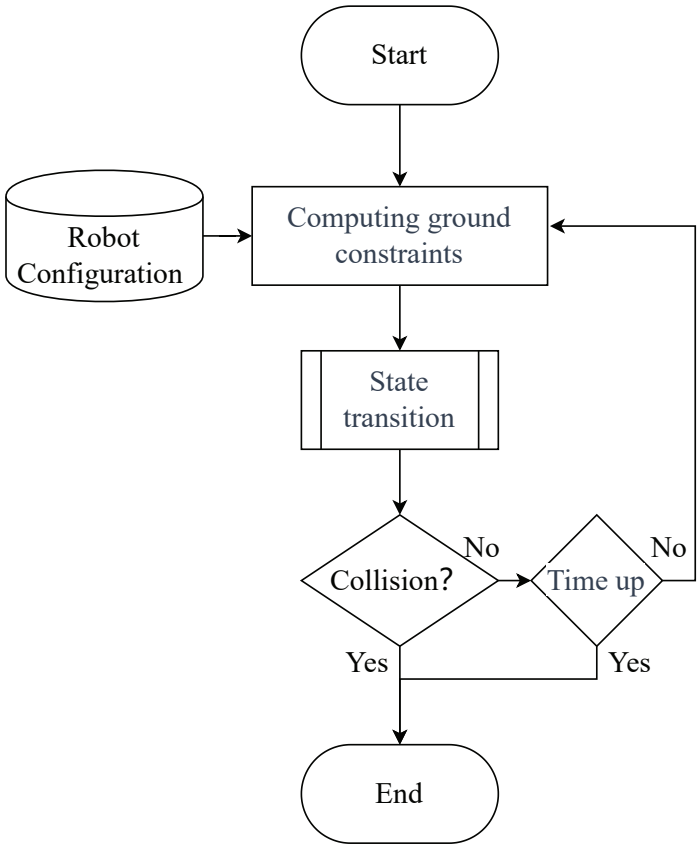

Figure 3.3: Flow chart of solving the equation of motion

uation as shown in Figure 2.2, it is necessary to deal with it in segments so that the range of BOA becomes smaller with consider the real situation. However, in the process of searching for the initial state, this part of the real situation can be completely ignored to ensure the continuity of the change, so that the system can converge to the final stable state in the BOA where only mathematics is considered, and this part of the area range is very large. Specifically, for example, selecting a situation where one stands on the ground with a large amount of kinetic energy, any structure can complete one step, but in reality, this will cause jumping. However, if we assume that it cannot jump, that is, the constraint force of the ground can be negative, then as the gait converges, the final state can be stable and satisfy the positive constraint force of the ground, which is the real situation.

3.2.3 Solving the equation of motion

ODE45 discretizes the ODE problem into a series of small time steps and estimates solutions for different time steps using fourth and fifth order Runge-Kutta methods, adapting the step size

based on the error to obtain more accurate solutions. Figure 3.3 illustrates the process of one iteration of the calculation. First, the current ground constraint force is calculated based on the robot configuration. Then, the current state is determined and the motion equation is calculated according to the state transition diagram, i.e. Figure 2.2. During each iteration, collisions are also checked to see if the robot's motion state has changed, and if so, the ODE45 calculation is terminated.

The collision detection of the robot involves calculating the positions of six endpoints of the robot's three legs. Based on the current state, the grounded endpoints are excluded, and the remaining endpoints are compared with the real-time ground height. A collision is triggered when the endpoint height is less than the ground height. It should be noted that in the computation process of ode45, to ensure accuracy, collision detection is triggered only when multiple loops continuously satisfy the collision condition, resulting in a phenomenon where the robot's toes penetrate the ground. Although the degree of penetration can be negligible, it will affect the next collision detection since the current state will be used in the next iteration of ode45. The solution is to increase the simulation calculation accuracy.

In addition, when the robot experiences walking failure, such as being unable to cross a potential energy barrier or collapsing due to a too-loose structure, corresponding error flag bits need to be set, and then the mechanism in the collision detection module should be called to end the ode45 calculation. As the simulation time is set to 10 seconds, which is enough time for one step to be completed, if an exit is caused by the integration time limit, it indicates that the robot cannot walk to the next step, and the corresponding error flag bits should also be written.

3.2.4 States update

After exiting ode45, the program determines whether to terminate or continue based on whether an error occurred or not. If a collision occurred and the program exited normally, data is recorded and the simulation continues.

Due to the occurrence of collision, it is necessary to calculate the velocity after collision and reset the current position according to the collision equation as Eq. 2.30, in order to ensure the normal operation of the next step.

In this context, there are two types of collisions: the first is a normal collision, which occurs when a swing leg contacts the ground; the second is a backward re-collision, as shown in Figure

2.3, which only results in a loss of kinetic energy without changing the corresponding position. Also, inevitably, such collisions may occur multiple times within a single step.

In this way, the simulation of one step motion is achieved, and by using a loop, continuous walking can be accomplished.

3.3 Simulation Results and Analysis

The simulation experiment on passive gait can be divided into two main parts. The first part focuses on verifying the structural and dynamic characteristics of RWT, which includes the influence of internal structure on walking. In this part, we validate the basic RWT model, the semicircular foot model based on realistic improvements, and the model that considers friction, all of which are based on the model presented in Chapter 2.

The second part aims to explore RWT as the minimal model of a robot morphology, including its various morphologies and corresponding modes of movement.

Table 3.2: Physical parameters setting for simulation

Symbol	Unit	Description
$m_i, i \in [a, b, c]$	1 [kg]	Weight of each leg
$I_i, i \in [a, b, c]$	$mL^2/4[kg \cdot \mathrm{m}^2]$	Inertia moment of each leg
L	1 [m]	Length of each leg
l_c	0 [m]	Length between connection point and tip point of each leg
ϕ	0.1 [rad]	Angle of gentle downhill
k	1000 [N/m]	Elasticity coefficient
c	1 [N·s /m]	Damping coefficient

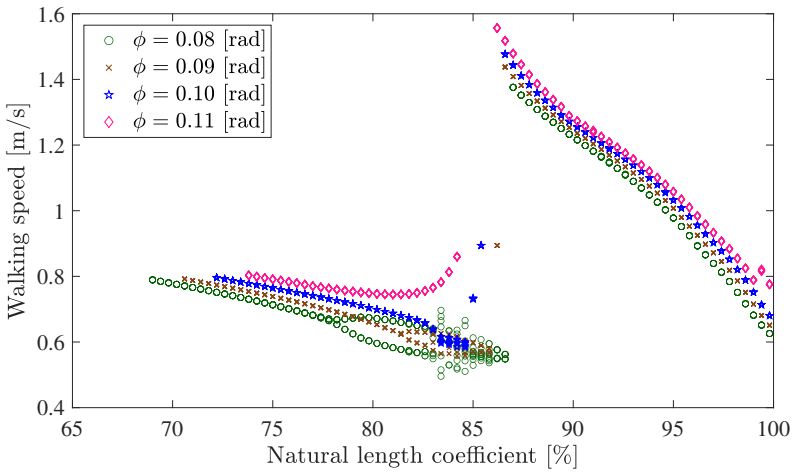

(a) Walking speed

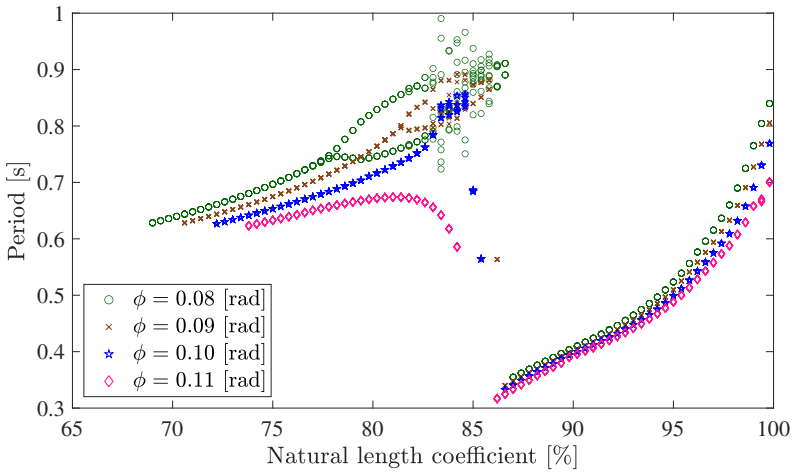

(b) Step period

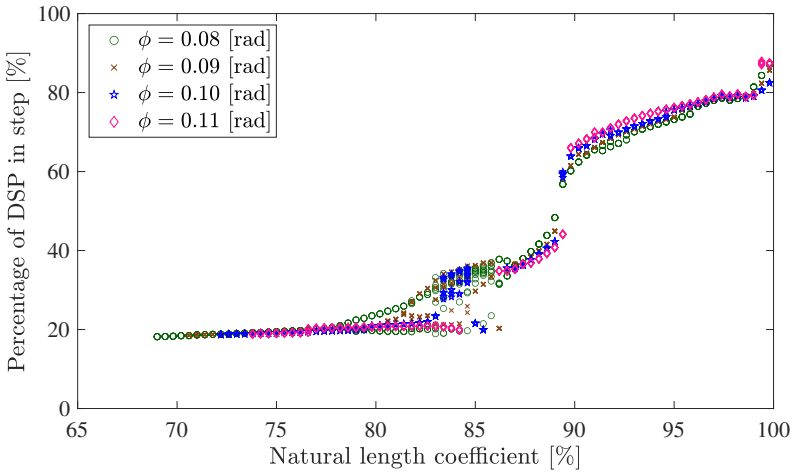

(c) Percentage of DSP

Figure 3.4: Gait descriptors versus natural length coefficient with different ϕ

3.3.1 Point-foot contact

Exploring the Relationship between Self-Structure and Locomotion

The most fundamental morphology of RWT involves point-foot contact. In this subsection, we investigate the influence of the natural length of the internal string on gait performance, based on the physical parameters presented in Table 3.2.

The regular hexagon is the equilibrium shape of RWT, and its natural length is denoted as l_n. Therefore, we base our observations on the assumption that the natural length $L_n = (L - l_c)/2$, and examine the influence of various coefficients L_n on gait performance.

The Figure 3.4 illustrates the relationship between the coefficient of natural length of strings and gait performance. The x-axis represents the coefficient of natural length of strings, while the y-axis represents gait performance,which are walking speed, step period and percentage of SSP in one step.

Through Figure 3.4, we can see that as the natural length increases, i.e. becomes looser, the gait of the RWT undergoes a sudden change, with the emergence of bifurcations and chaotic behavior. This indicates that with the increase of natural length, RWT exhibits new characteristics, and chaotic phenomena only arise during the transition from the current characteristics to the new ones, breaking the constraints of the current characteristics. This result demonstrates the necessary condition for RWT as a robot morphology, that is, as the relative structure changes, the system exhibits new characteristics, which can be seen as products of different morphologies, i.e. changes in morphology occur.

On the other hand, as the slope increases, we can see that bifurcation and chaotic phenomena become less apparent, and at the minimum slope, bifurcation is most pronounced. In the passive gait, slope can be seen as an input of external energy, where large slope or external energy suppresses the characteristic of morphology, thus making chaotic phenomena less pronounced in RWT's motion. This shows that RWT's motion behavior is the result of a balance between internal characteristics and external energy input. When the input energy from the environment is not strong, the internal characteristics dominate, and thus chaotic phenomena are more likely to occur, which is determined by internal characteristics. When the input energy from the environment is high, the system characteristics are suppressed, but this cannot change the change in morphology. Thus, in the process of morphological change, chaotic phenomena are less pronounced.

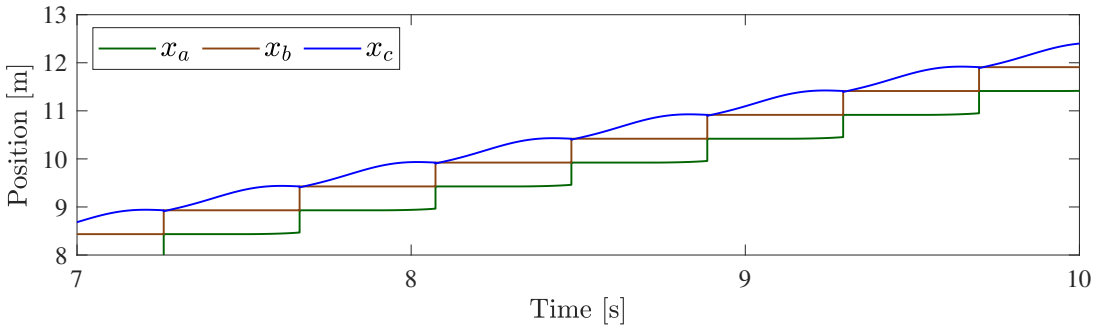

(a) Variation of x over time

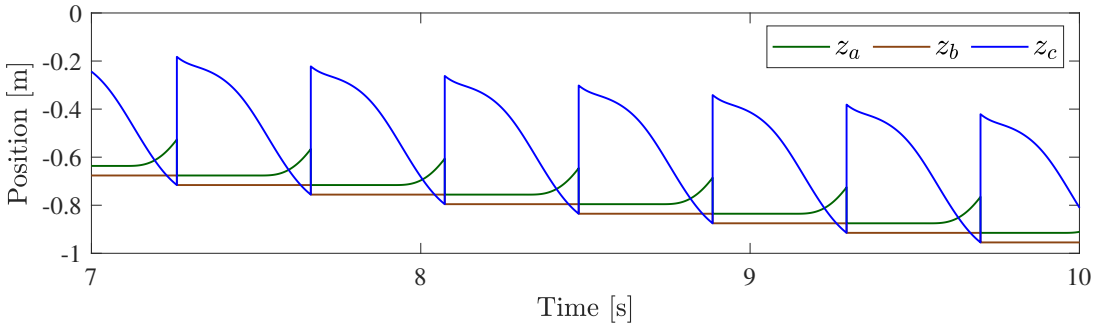

(b) Variation of z over time

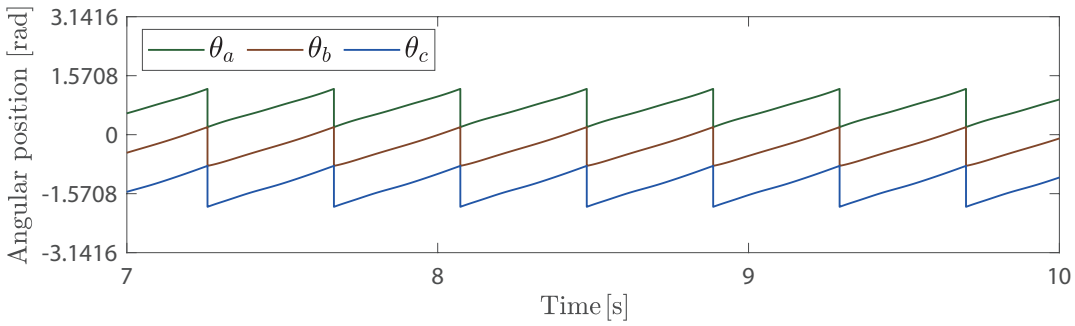

(c) Variation of angular positions over time

Figure 3.5: Variation of position in period-1 gait

Period-1 Walking Gait

Based on Figure 3.4, we discovered period-1 and period-2 gaits, and we conducted investigations on them separately. Figures3.5 and Figure 3.6 show the simulation results of the period-1 gait, which are the changes in position and velocity, respectively. It is worth noting that in the velocity plot, we observed the phenomenon of backward collision, as shown in the zoomed-in Figure 3.6. Figure 3.7 is its phase plot, which shows a stable limit cycle motion, indicating the stability of RWT's movement. Figure 3.8 is its motion stick plot, which shows

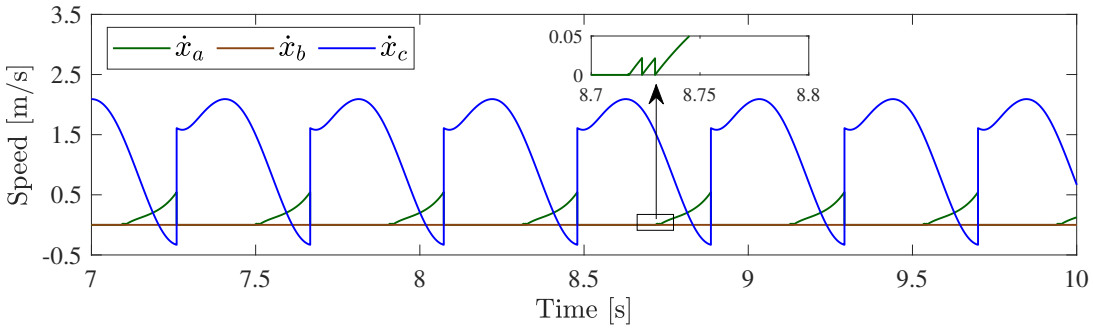

(a) Variation of $\dot{x}$ over time

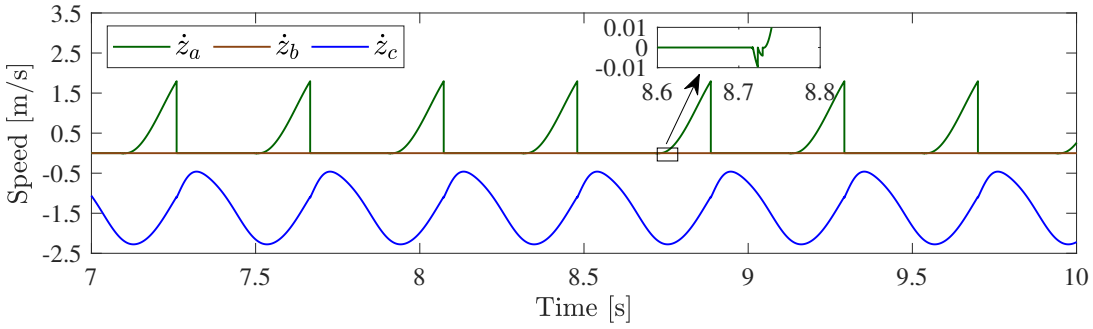

(b) Variation of $\dot{z}$ over time

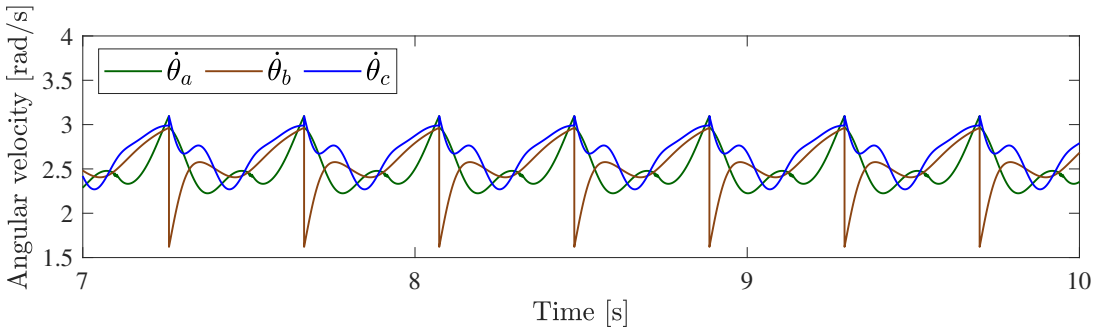

(c) Variation of angular velocities over time

Figure 3.6: Variation of velocity in period-1 gait

the shape of its limit cycle motion. Moreover, from the angular velocity changes in Figure 3.6 (c), we can see that its velocity changes are very unstable, which is determined by its occasional high non-linear elastic force. However, this strong internal instability can form a stable limit cycle gait through continuous walking, which is a very interesting phenomenon.

Period-2 Walking Gait

Like the period-1 gait, Figures 3.9-Figure 3.12 illustrate the corresponding motion changes of the period-2 gait, which show that compared with the period-1 gait, the period-2 gait has

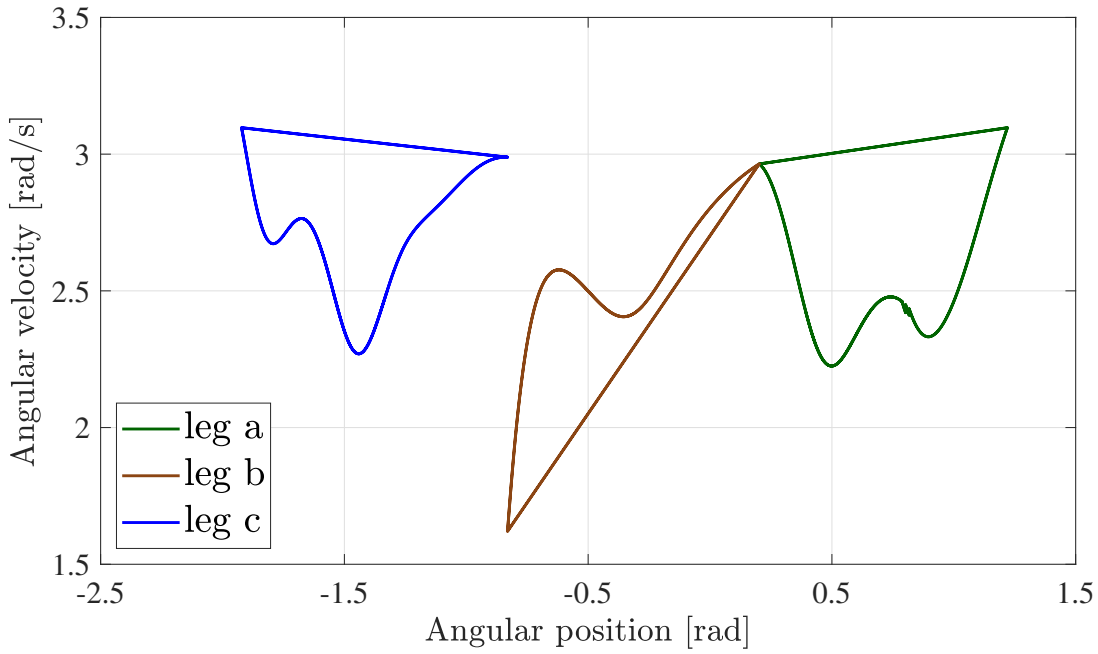

Figure 3.7: Phase diagram of period-1 gait

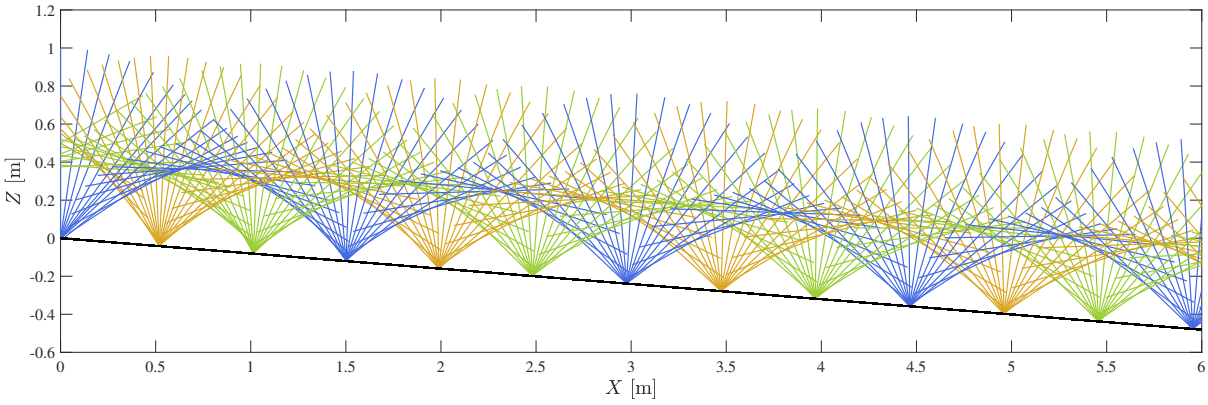

Figure 3.8: Stick diagram of period-1 gait

a slower speed and a larger step period. The period-2 gait is evidence of the broken convergence domain during the transition from morphology 1 to morphology 2, and also evidence that although the RWT appears unchanged, its internal characteristics have been altered. This suggests that changes in morphology are not necessarily obvious, so judging morphology changes based solely on structural changes is inaccurate. Instead, changes in the characteristics of the gait should be used to determine changes in morphology, based on changes in its underlying properties on the basis of structural changes.

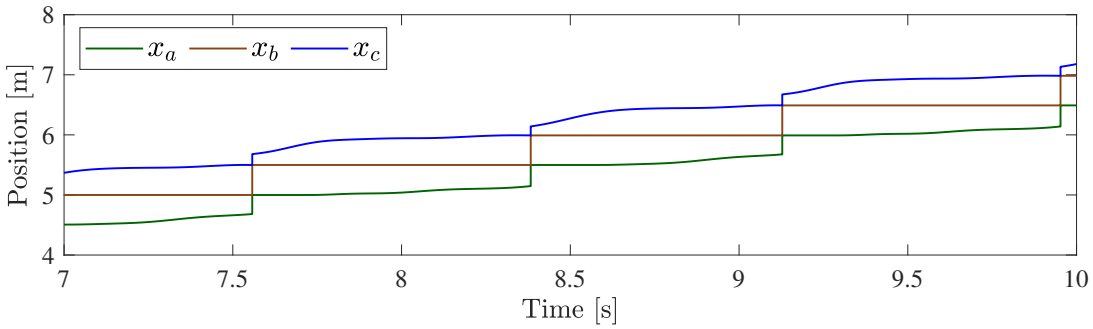

(a) Variation of x over time

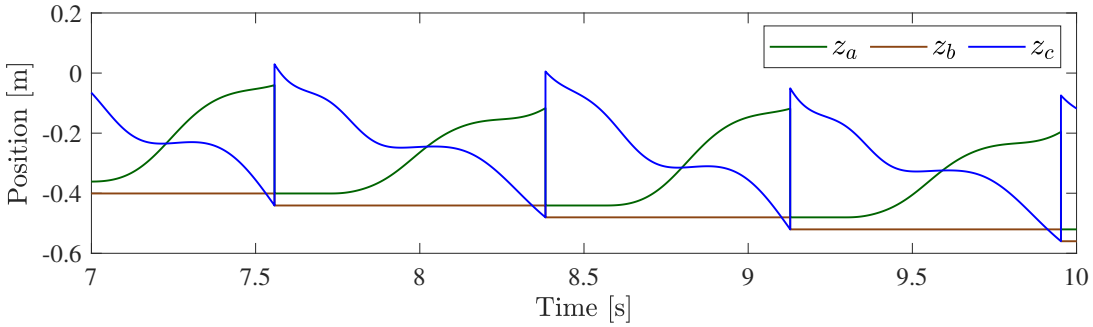

(b) Variation of z over time

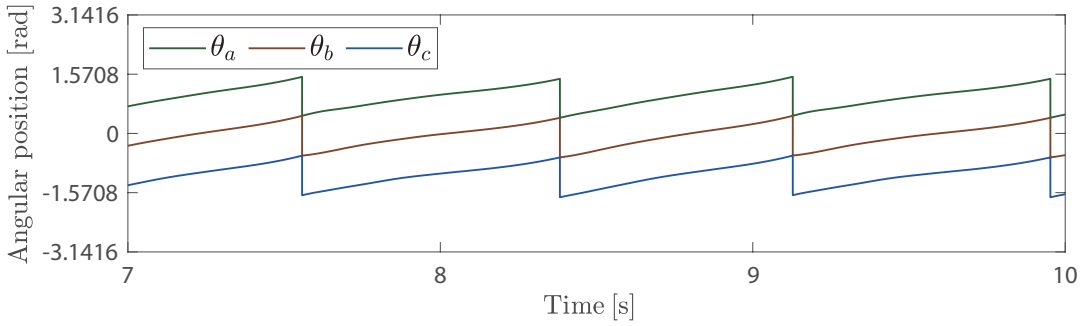

(c) Variation of angular position over time

Figure 3.9: Variation of position in period-2 gait

Relationship Between Connection Position and Locomotion

Apart from the natural length of the spring affecting its intrinsic characteristics and morphology, another structural factor, the connection position l_c, also affects its morphology. Figure 3.13 shows its walking performance under different values of l_c.

It can be observed that a certain morphology is presented around $l_c = 0$, which then abruptly changes to another morphology. Furthermore, as l_c increases, the step period increases and the velocity decreases, and chaotic behavior gradually appears, indicating the end of the current

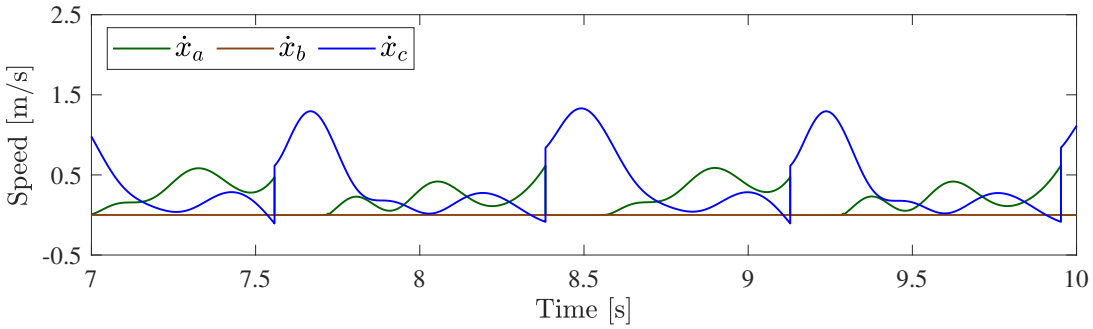

(a) Variation of $\dot{x}$ over time

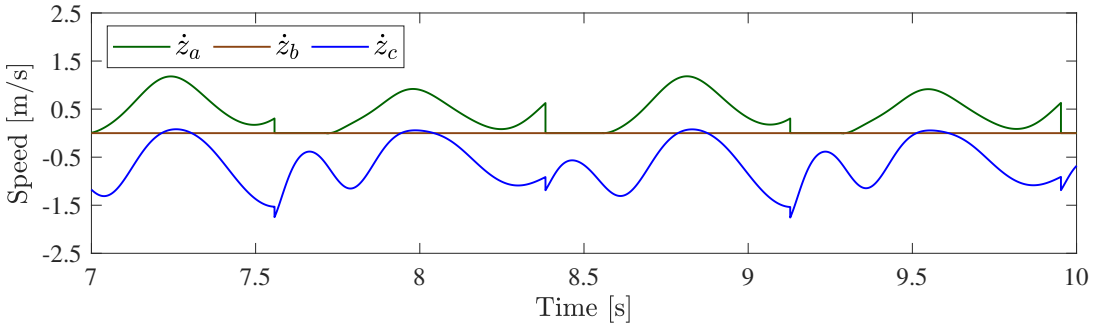

(b) Variation of $\dot{z}$ over time

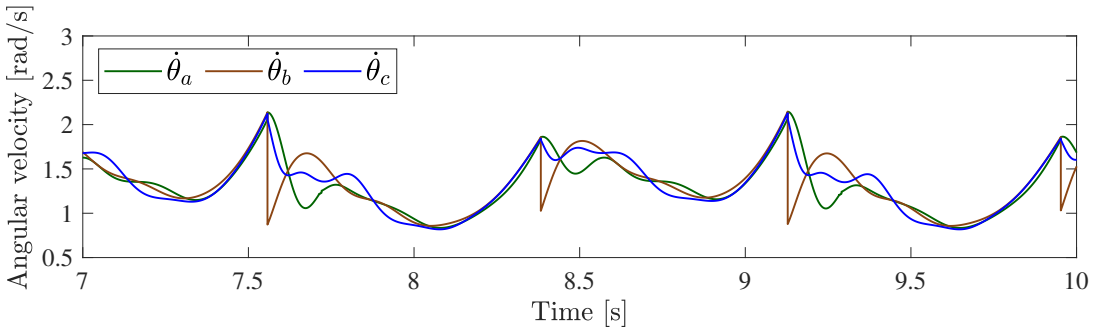

(c) Variation of angular velocity over time

Figure 3.10: Variation of velocity in period-2 gait

morphology. As shown in Figure 3.13(c), the proportion of DSP during the transition between the two morphologies does not change abruptly, indicating the same walking posture. This suggests that different morphologies can produce the same walking pattern, but the performance of the motion under that pattern will be significantly different, i.e., morphology corresponds only to the optimal way of motion. In addition, as the slope increases, i.e., the external energy increases, there is still a phenomenon of excessive energy suppressing the internal characteristics.

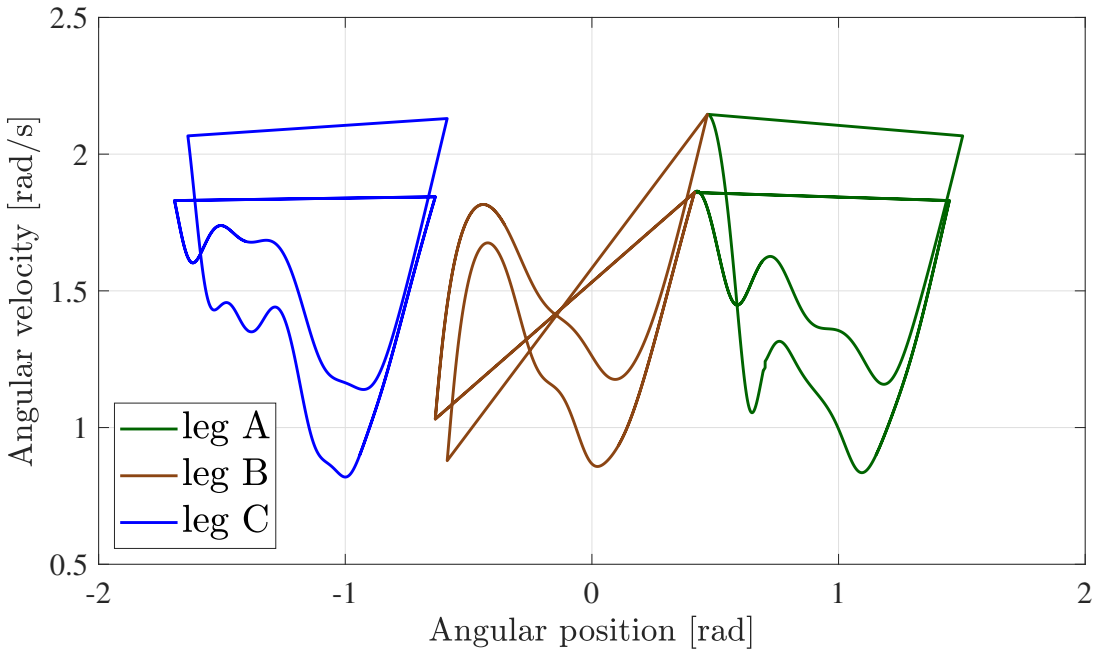

Figure 3.11: Phase diagram of period-2 gait

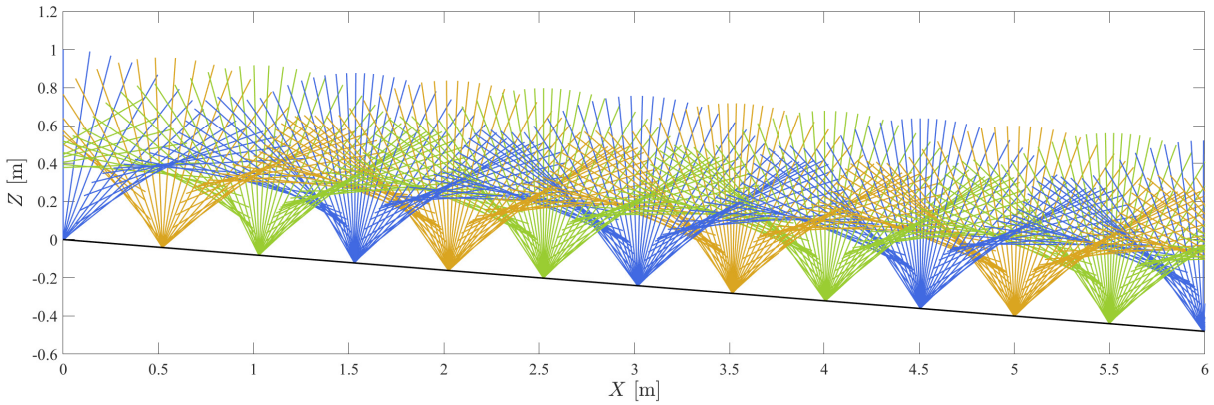

Figure 3.12: Stick diagram of period-2 gait

3.3.2 Semicircular feet

'Semicircular feet' is a typical real-world problem because ideal point contact does not exist. The Relationship between the radius of semicircular feet and walking performance is presented in Figure 3.14 and its walking gait is shown as Figure 3.15. It can be observed that the variation in radius affects its internal characteristics, leading to changes in its morphology. As the radius of the semicircle increases, the step period decreases. However, interestingly, the speed does not increase and gradually decreases. This suggests that the radius of the semicircle primarily affects its stride length, as the stride length decreases with increasing radius. This is

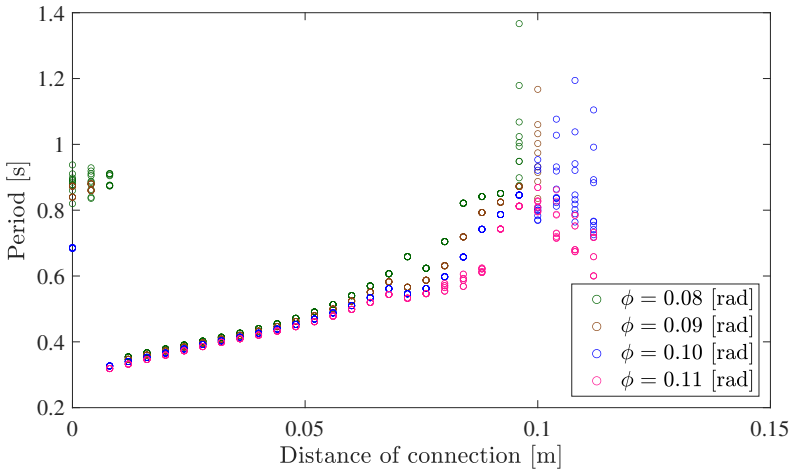

(a) Walking speed

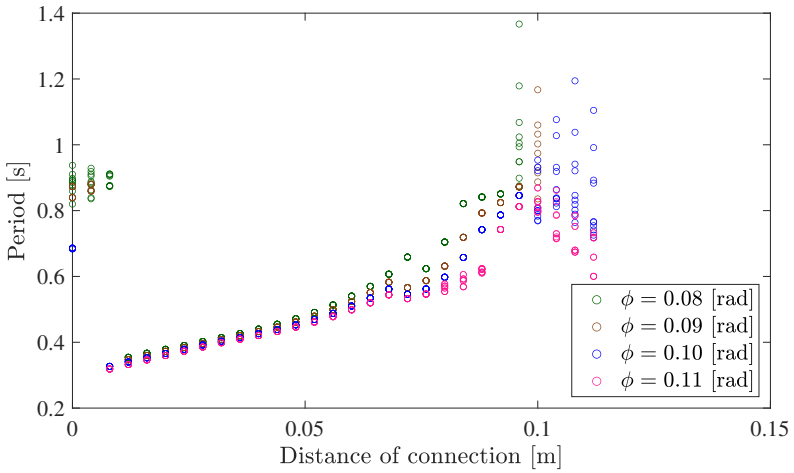

(b) Step period

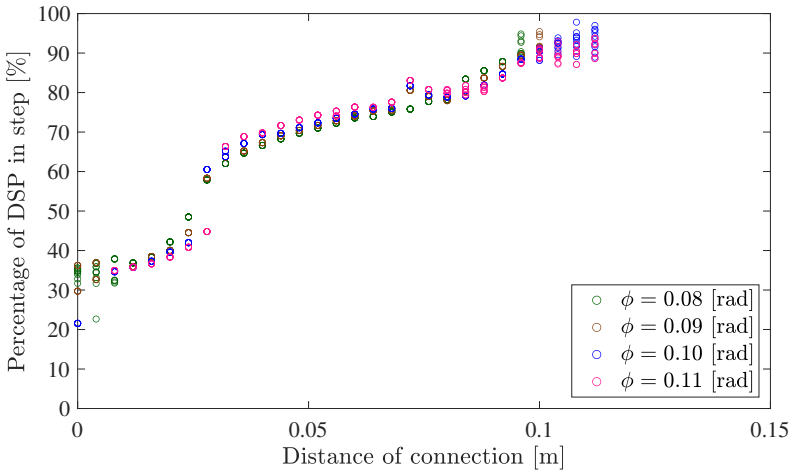

(c) Percentage of DSP

Figure 3.13: Gait descriptors versus distance of connection with different ϕ

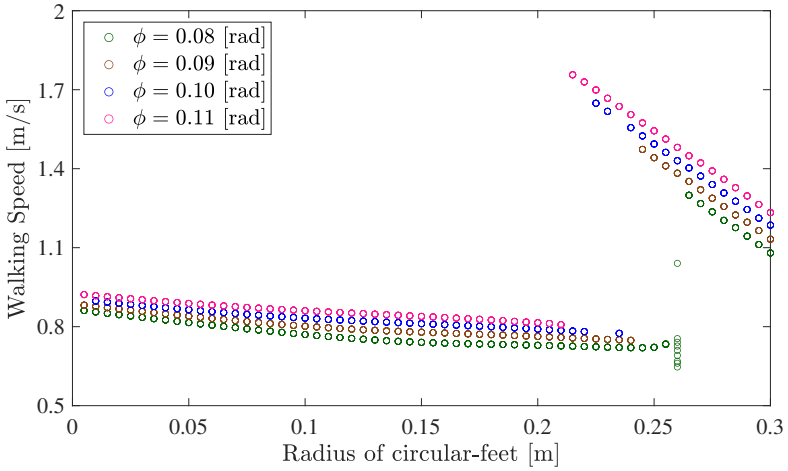

(a) Walking speed

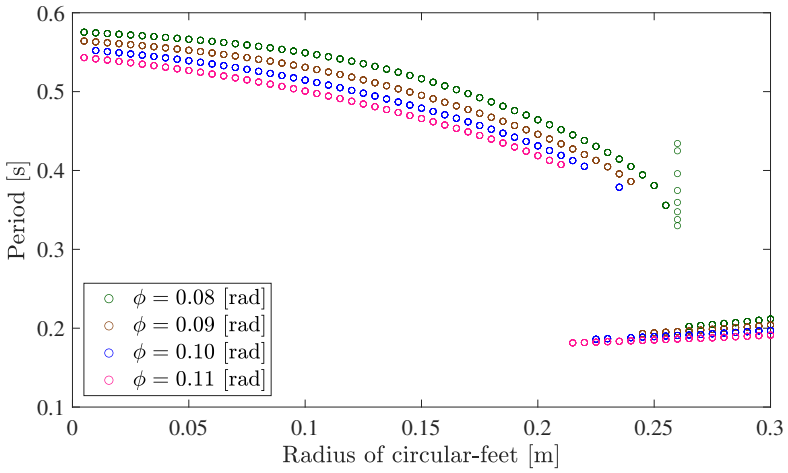

(b) Step period

Figure 3.14: Gait descriptors versus radius of circular-feet with different *r*

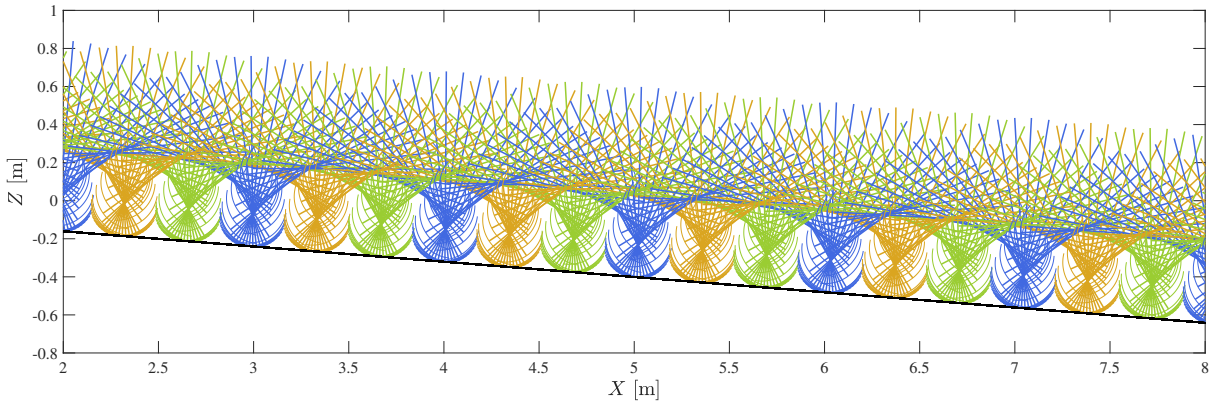

Figure 3.15: Stick diagram of RWT with semicircular feet

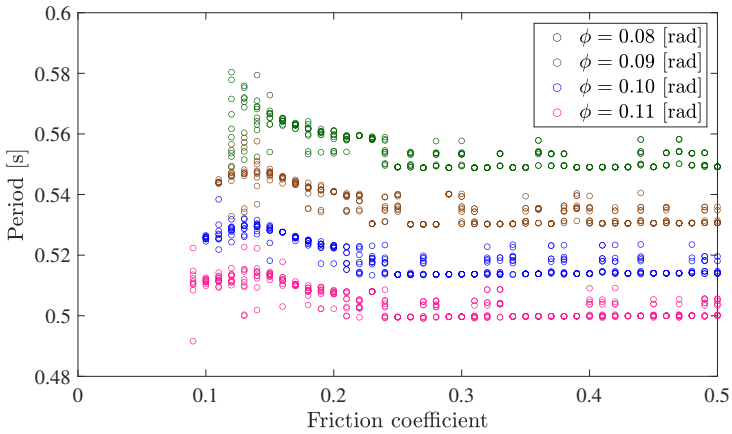

(a) Step period

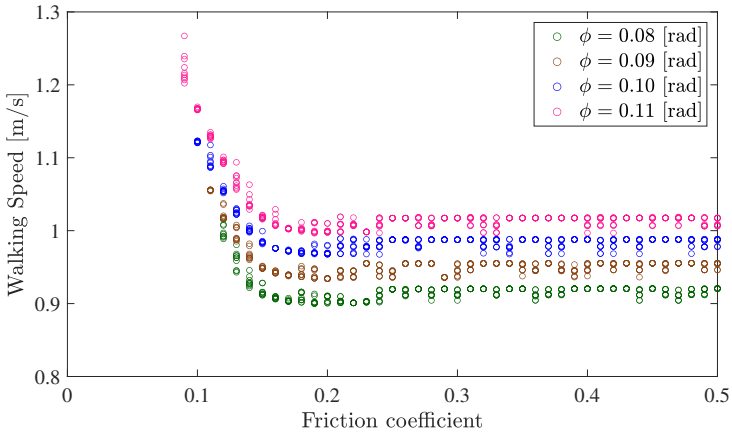

(b) Walking speed

Figure 3.16: Gait descriptors versus friction coefficient with different ϕ

understandable as changes in foot shape are more likely to alter the mode of movement than the morphology. Nonetheless, when the radius becomes too large, it affects its morphology, leading to abrupt changes.

3.3.3 Low friction surfaces

Walking on a frictional surface is a realistic problem, and Figure 3.16 investigates the effect of different levels of smoothness of the surface on gait at various inclinations. It can be seen that RWT can achieve stable walking at a fairly smooth surface with $\mu = 0.1$, and achieve a stable gait (period-1 or multi-period). On a smooth surface, high-speed and stable walking can be achieved by utilizing friction.

Figure 3.17 investigates the performance of different semicircular feet on various smooth

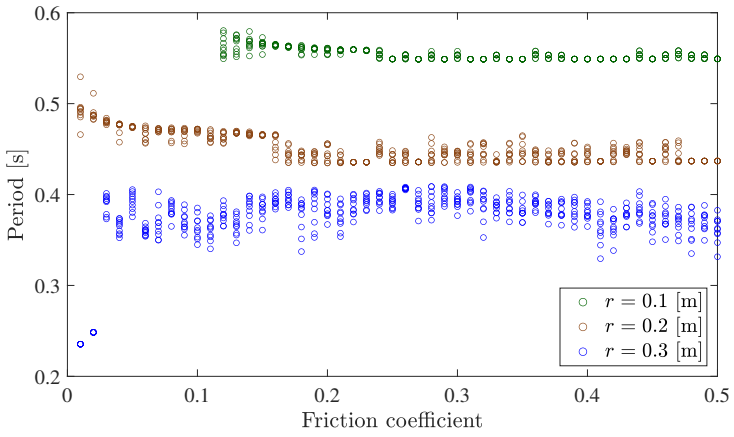

(a) Step period

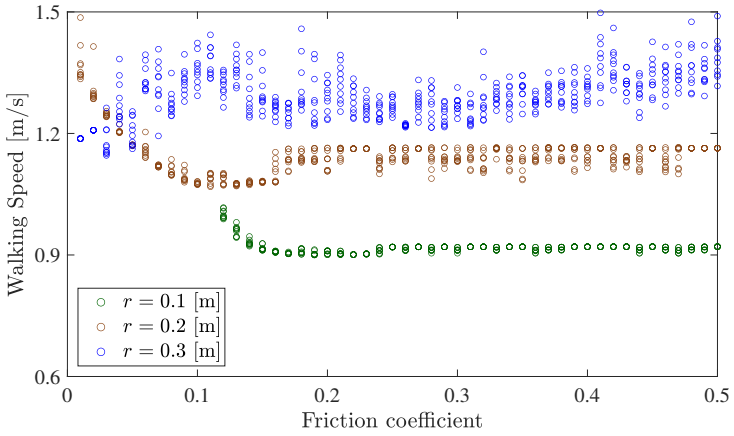

(b) Walking speed

Figure 3.17: Gait descriptors versus friction coefficient with different r

surfaces. When r is small, it is relatively easy to achieve period-1 gait, while with the increase of r, it gradually shows multi-period. This is also understandable, as a too large semicircular radius is more flexible on a frictional surface, but based on the self-convergence of RWT, its gait will not fail.

3.3.4 Morphological exploration

Various Gaits Realization

We recorded the leg support states at each forward collision, mark as 0, 1, 2, 3. It is important to note that the morphological changes are continuous, *i.e.*, as shown Figure 2.2, and non-sequential gait transition are unrealized, thus ultimately, the average value of the markers

can represent the current motion morphology that corresponds the specific motion as shown in Table 3.3. Here, the check mark represents a definite need to occur in one step, the cross mark represents a definite need not to occur in one step, and the question mark represents a possibility of occurrence in one step. It means if the value after averaging is $e.g.$ 0.5, then it must consist of a NSP and a SSP, and must not consist of a DSP and a TSP, it is therefore the morphology corresponding to skipping according to the above definition.

As we can see in Figure 3.18, the vertical and horizontal axes indicate the RWT's connection method and the internal softness, which determine the structural properties, while the colors represent the different states of ground contact. The blank area represents failures of movement, such as collapsing because the structure is too soft to support itself, or being immobile due to insufficient energy.

First of all, we can see that passive gait can be achieved which the slope $\phi = 0.03$ [rad] is relatively small. We use specific resistance $SR = p/(mgv)$ to represent energy efficiency, where p is the average power of gravitational potential energy, and v is the average speed of movement. The smaller the value the higher the energy efficiency, and in passive gait, the magnitude of the slope is equal to the magnitude of SR, so we can see that the energy efficiency of RWT is also very high unlike the other soft robots. Even though part of the kinetic energy will be converted into elastic potential energy, the remaining kinetic energy can still make the RWT overcome the potential energy barrier and complete the locomotion.

On the other hand, here we consider the gravitational potential energy as the external power source, then as the slope becomes larger the RWT gradually changes to different morphologies as the external power source increases. Consequently, it appears that the morphology corresponding to walking is the basic morphology, while the morphology corresponding to crawling is exhibited under high energy input, for stability and adaptability, and the morphology corre-

Table 3.3: Mapping relationship between markers and gaits

Gaits	Marks			
Skipping	0(✓)	1(?)	2(?)	3(×)
Walking	0(×)	1(✓)	2(?)	3(×)
Crawling	0(×)	1(?)	2(?)	3(✓)

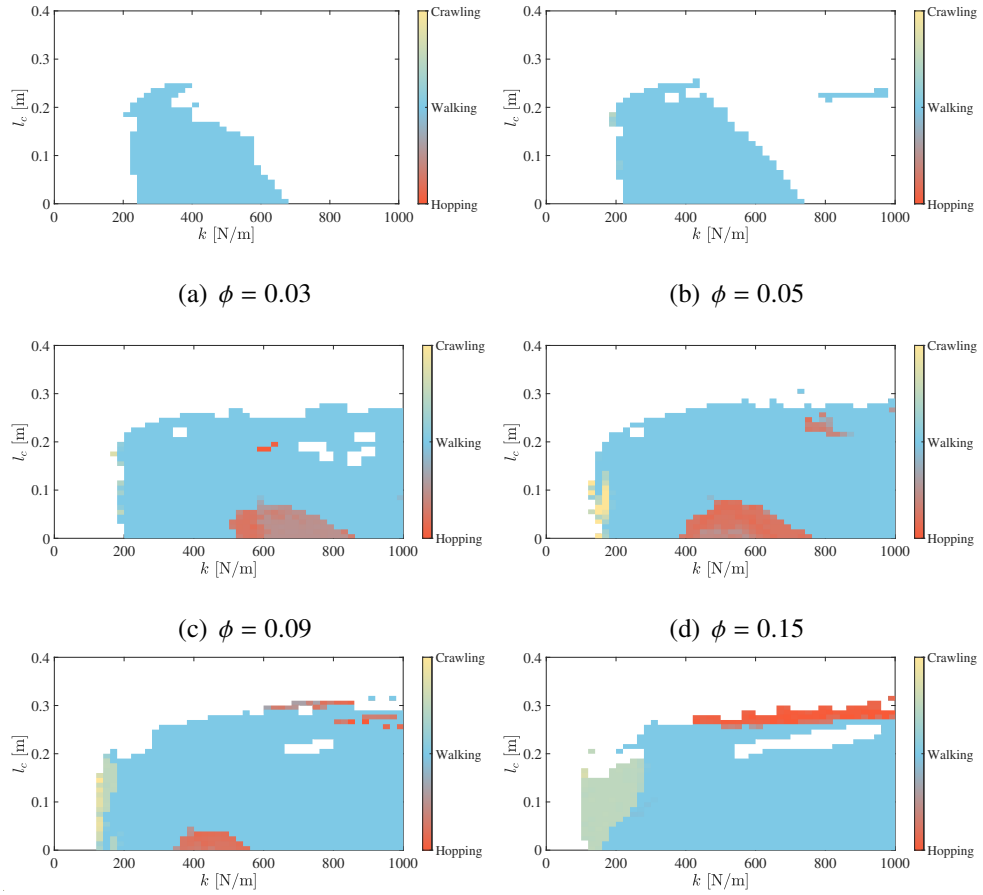

(a) $\phi = 0.03$ (b) $\phi = 0.05$

(c) $\phi = 0.09$ (d) $\phi = 0.15$

(e) $\phi = 0.2$ (f) $\phi = 0.3$

Figure 3.18: Various gaits emerged from passive locomotion under different slopes.

sponding to skipping are exhibited for high speed and agility.

The value of k represents the tightness of the RWT. When k is very small, it cannot support its own structure and collapses, resulting in the move failing. While in Figure 3.18(a) and (b), there is still a failure to move when k is very large. This is due to the fact that under a small energy input, large k leads to an increase in elastic potential energy, thus consuming a large part of the kinetic energy, and thus stopping the movement.

Crawling Gaits Realization and Analysis

According to Figure 3.18, the morphology corresponding to crawling exists in the region of lower internal elasticity, which is associated with a higher degree of independence between each leg's dynamic properties. Figure 3.19 demonstrates the simulation results that shows the emergence of morphology corresponding to crawling . The light yellow area indicates the

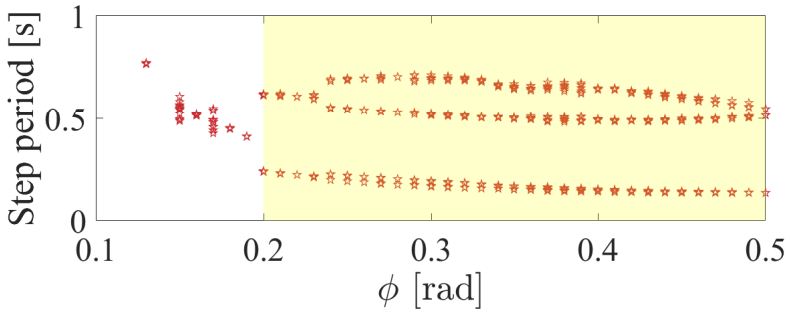

(a) Step period

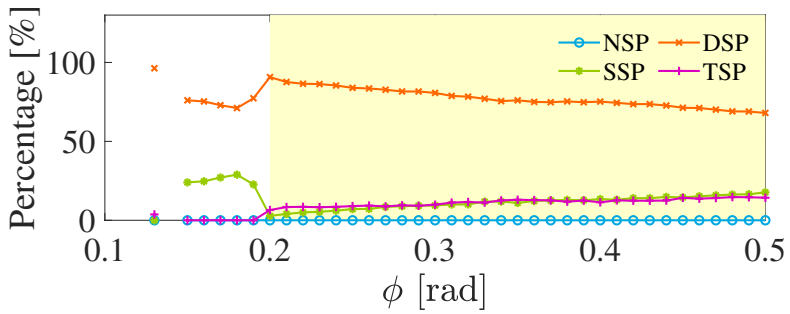

(b) Percentage of leg support phases

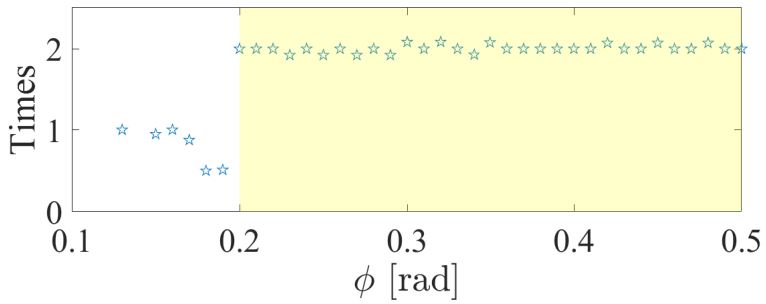

(c) Leg-ground interactions per cycle of the COM

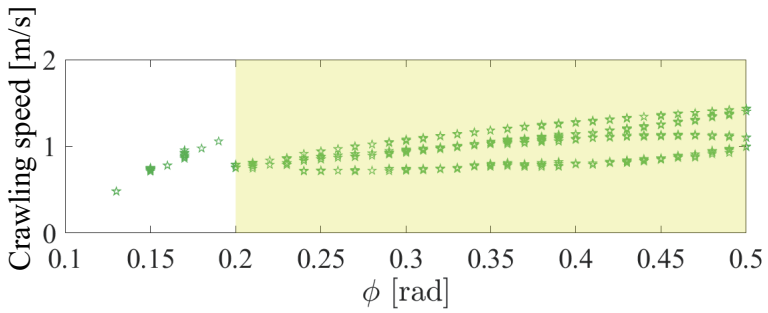

(d) Crawling speed

Figure 3.19: Numerical simulation results of the emergence of crawling gaits.

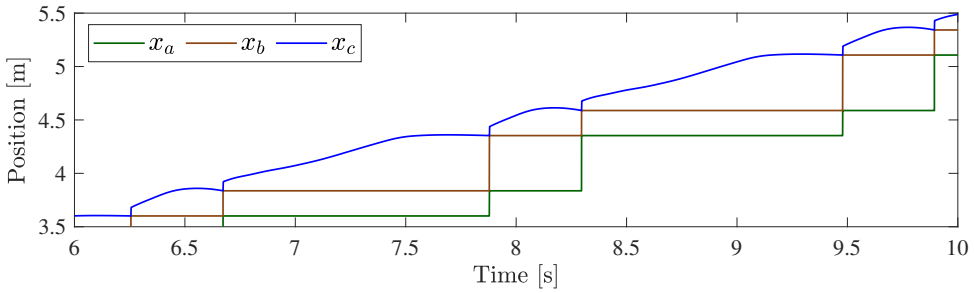

(a) Variation of x over time

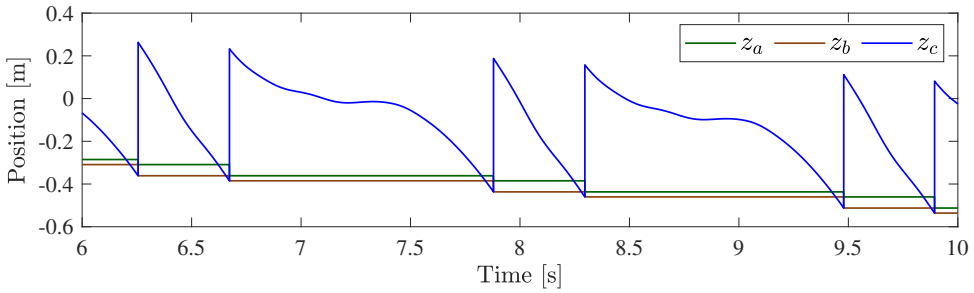

(b) Variation of z over time

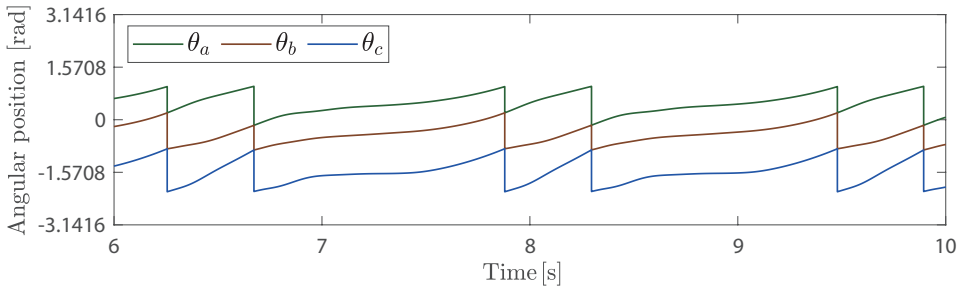

(c) Variation of angular position over time

Figure 3.20: Variation of position over time of crawling gaits

morphology corresponding to crawling and it also can be seen from Figure 3.19(b) that the TSP begins when ϕ exceeds 0.2 [rad]. First, it can be seen from Figure 3.19(a) that the gait of the morphology corresponding to crawling is multi-periodic and tends to converge as the external input energy increases. Legged robot forward locomotion generally involves periodic changes in the trajectory of COM, so we counted the number of leg-ground interactions when the COM cycle changes once, as can be seen in Figure 3.19(c). As a result of the morphology corresponding to crawling , two times leg-ground interactions are maintained, resulting in the multi-periodic gait pattern. Additionally, 1:2 resonance of the change in elastic potential energy with the walking frequency is determined by the robot's structural properties. This demonstrates that resonance phenomena are highly correlated with morphology and can prove that it is based

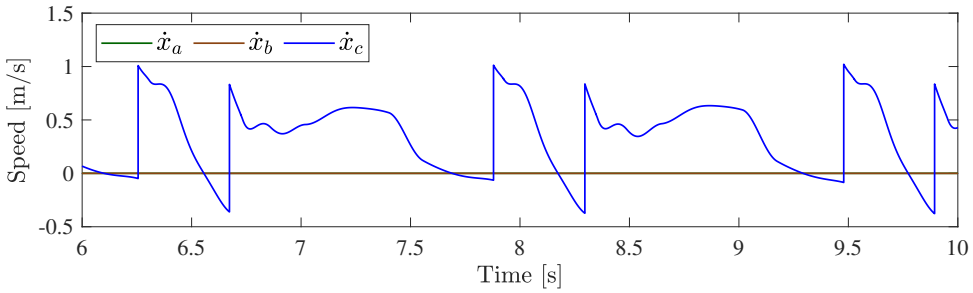

(a) Variation of $\dot{x}$ over time

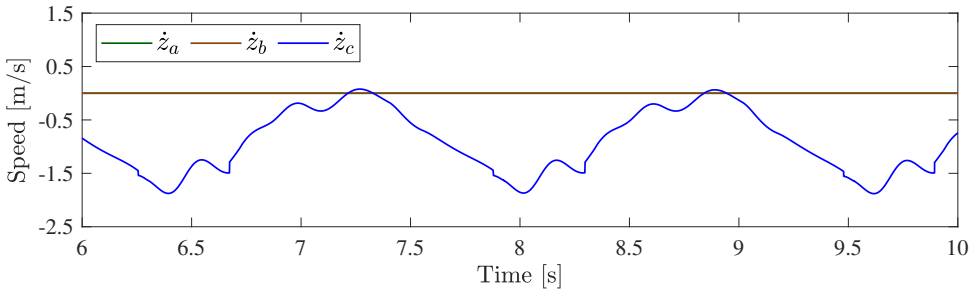

(b) Variation of $\dot{z}$ over time

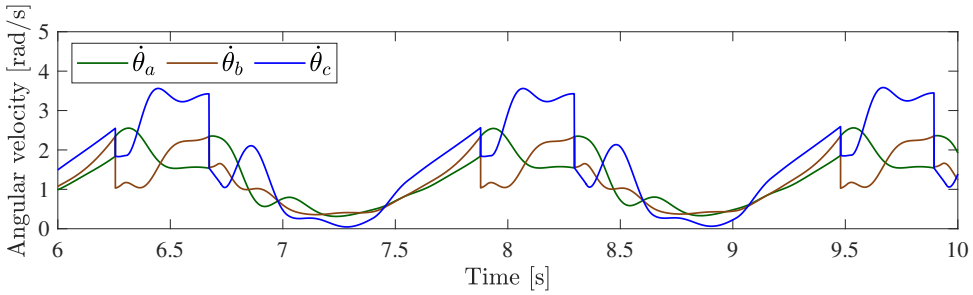

(c) Variation of angular velocity over time

Figure 3.21: Variation of velocity over time of crawling gaits

on its own structural properties.

And the specific simulation results of crawling are shown in Figure 3.20-3.23.

Walking Gaits Realization and Analysis

As the basic morphology, walking is more easily recognizable as the light yellow area in Figure 3.24. From Figure 3.24(a), we can see that the typical limit cycle gait is achieved. This gait is efficient and stable and is determined by its own morphology. The abrupt change around $\phi = 0.1$ [rad] is the result of the different slopes, namely the external power source, that affect the resonance and lead to changes in gait. Such a change in gait can be clearly seen in 3.24(b),

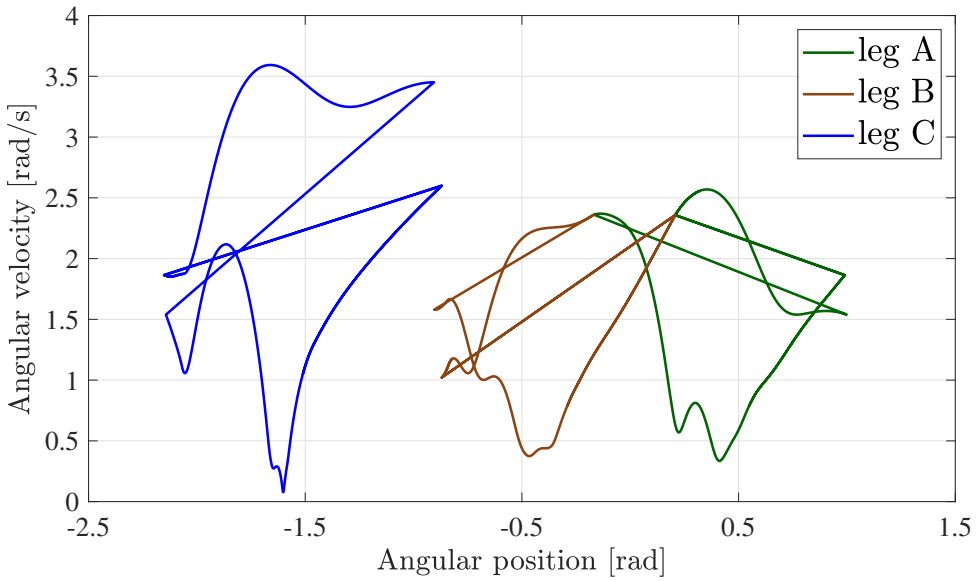

Figure 3.22: Phase diagram of crawling gaits

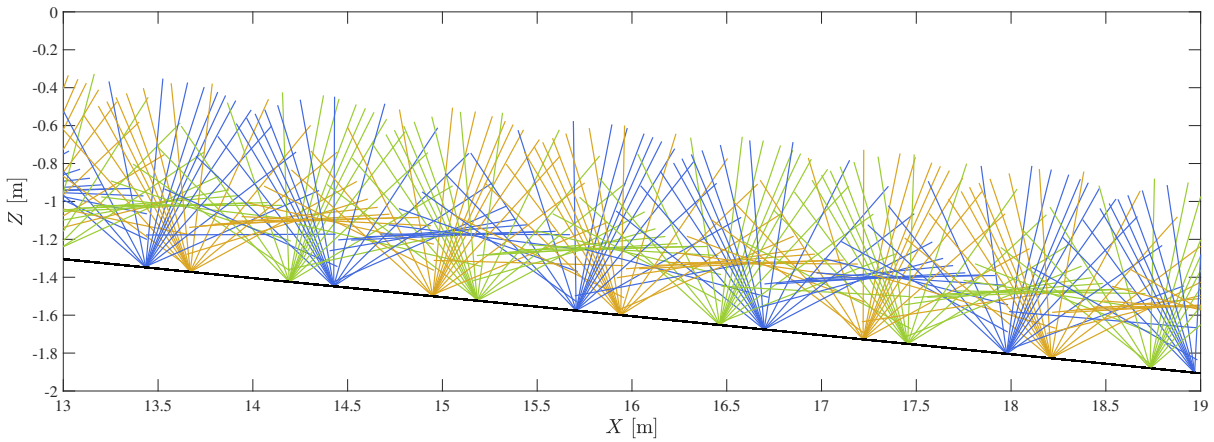

Figure 3.23: Stick diagram of crawling gaits

where the percentage of SSP and DSP crosses about this point. Accordingly 1:1 resonance is a relatively stable state, which can be used as evidence that the morphology corresponding to walking is a very basic morphology.

Skipping Gaits Realization and Analysis

As shown in Figure 3.18, as ϕ increases, morphology corresponding to skipping will appear in the lower middle of the graph and then disappear, which we call it typical morphology corresponding to skipping , while morphology corresponding to skipping will also appear in the upper right corner when ϕ is relatively large. A large slope, that the large external power

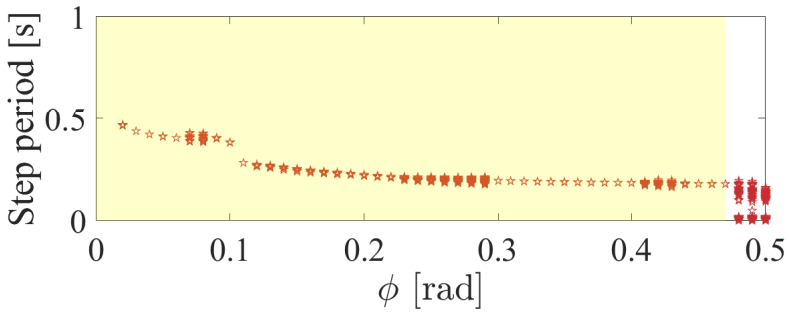

(a) Step period

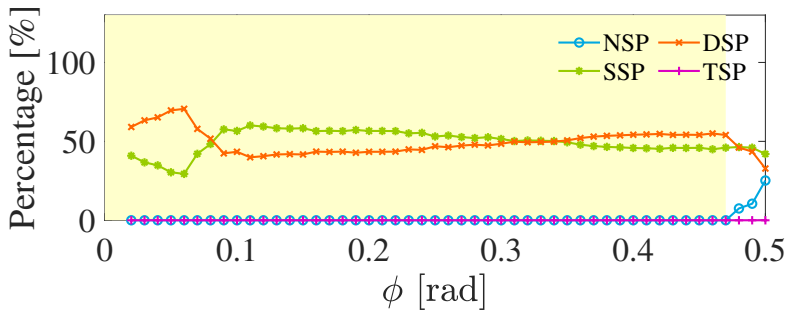

(b) Percentage of leg support phases

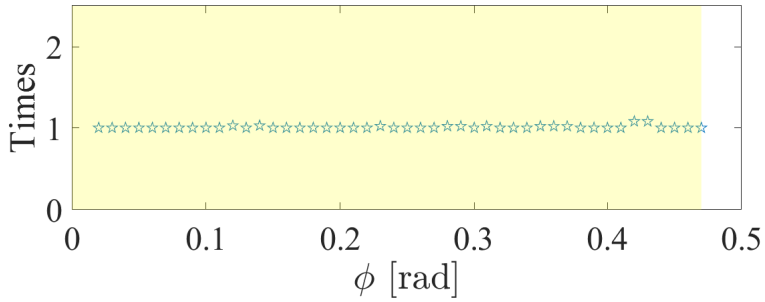

(c) Leg-ground interactions per cycle of the COM

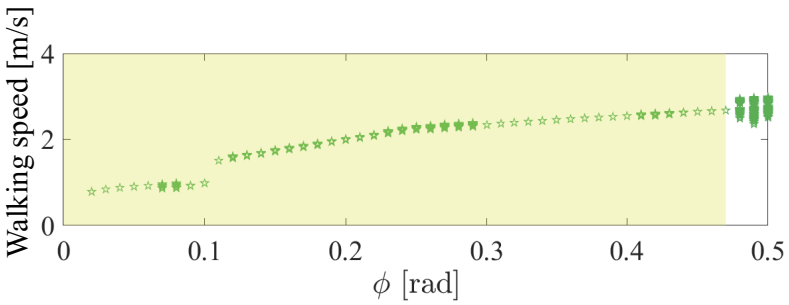

(d) Walking speed

Figure 3.24: Numerical simulation results of walking gaits.

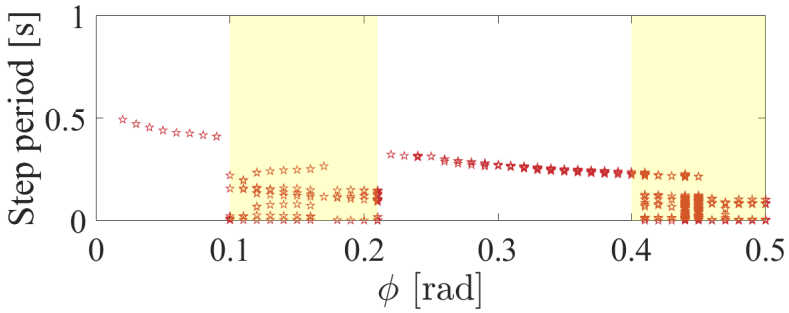

(a) Step period

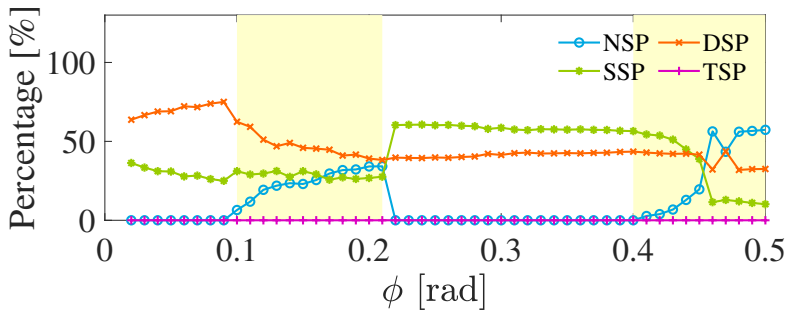

(b) Percentage of leg support phases

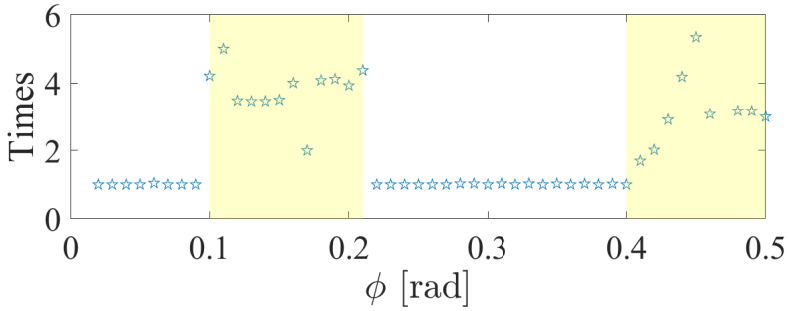

(c) Leg-ground interactions per cycle of the COM

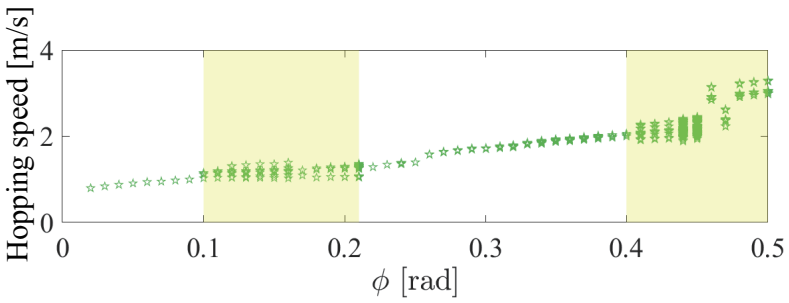

(d) Skipping speed

Figure 3.25: Numerical simulation results of skipping gaits appearances and disappearances

source, will result in the robot yielding to the morphology corresponding to skipping . Such yielding can reasonably dissipate the excess energy and express as morphology corresponding to skipping , but it does not indicate that the morphology corresponding to skipping is general at this time based on its extremely low energy efficiency, thus only the typical morphology corresponding to skipping is reasonable and general, so we investigated it specifically.

Figure 3.25 shows the results of morphology corresponding to skipping and the left light yellow area is the typical morphology corresponding to skipping which is generated due to 1:4 resonance as shown in Figure 3.25(c). We can see that the morphology corresponding to skipping also includes SSP and DSP, which indicates that the robot will not pick up immediately after landing, but will have a boosting process, which is the difference between skipping and running.

3.4 Summary and Discussions

In this chapter, a simulator was first designed using MATLAB, which not only validated the mathematical model but also explored the motion characteristics of the RWT. Passive walking can ingeniously convert energy into motion through its own structural characteristics, and the current morphological characteristics make full use of external energy to produce corresponding walking movements. This study found that the structural characteristics of the RWT do not have continuity through passive walking, indicating that the change in its structure leads to the production of different characteristics, i.e., different morphologies. This demonstrates the RWT's ability to serve as a minimal model for robot morphology research. On the other hand, in the simulation results, period-1, period-2, and chaotic gaits were also observed, which appeared in the morphological transitions, supporting the above views. Based on this, this study delved into the different morphologies of the RWT, finding that different morphologies were suitable for different types of movement, such as crawling, walking, and skipping, and provided specific differentiation and analysis. The content of this chapter validated the mathematical model of the RWT and demonstrated its feasibility as a model for robot morphology research.

In addition, it is also necessary to improve the minimal model to study special scenarios. Therefore, in this chapter, we provide specific analyses and corresponding conclusions on semi-circular feet and frictional surfaces.

Chapter 4

Morphology-Based Control and Analysis

4.1 Overview

Traditional control methods often rely on reducing the order or using approximation techniques for higher-order nonlinear systems. However, these methods are only applicable to systems with weak nonlinearity or lower order. When it comes to systems with higher order or strong nonlinearity, traditional control methods are often inadequate. Nevertheless, higher-order nonlinear systems are not unsolvable. Although the precise state changes may be elusive, their ultimate convergence trends, known as attractors, may objectively exist. The proposed MBC in this study takes into account the morphological characteristics to generate or modify the attractors of the system, enabling control of high-order nonlinear systems towards the desired state. Due to the inherent presence of time and uncertainty in converging towards attractors, MBC control faces challenges such as low response and precision. However, these challenges are unavoidable when dealing with higher-order nonlinear systems. The tensegrity robot studied in this research is a typical example of such a higher-order nonlinear system, with its internally coupled elastic elements introducing higher nonlinearity and complexity to its motion. Therefore, MBC is the appropriate approach to address the control of the tensegrity robot.

In this chapter, firstly MBC is applied to the control of a spring-mass car model in order to achieve different types of locomotion, from walking to crawling, by transforming the morphology of the system. The effectiveness of this method is demonstrated through experiments on a RWT system, where MBC is used to control the transition from one morphology to another,

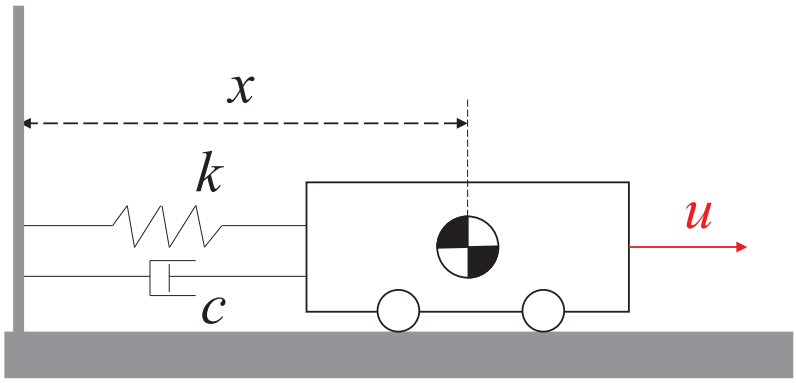

Figure 4.1: Spring-mass-damper system

resulting in different types of locomotion.

Furthermore, the authors propose a simpler SRWT model that is capable of moving on flat terrain, and exhibit typical period-1 and period-2 gaits with stability analysis. Finally, the authors provide several examples of potential applications, such as walking on uneven terrain or in low gravity environments.

Compared to traditional position control methods, MBC is more indirect in that it controls the morphology of the system rather than the posture directly. This approach has the advantage of being more adaptable and requiring less complexity.

4.2 Introduction of MBC Through Simple Model

As shown in Figure 4.1, a spring-mass-damper system is considered with a distance of x from the fixed point, k and c representing its elastic and damping coefficients, respectively. The natural length of the spring is denoted as l_1. The input u controls its movement in the x direction.

Morphology refers to the characteristics that correspond to a certain structure, and the most common spring-damper system can also be seen as the smallest unit that makes up the morphology. The position x can represent its structure, and k and c can determine its characteristics.

The morphology of rigid robots is fixed due to the absence of the spring-damper term, or the negligible effect of this term, which prevents changes in their characteristics. On the other hand, soft robots can exhibit multiple morphologies because their corresponding characteristics can change with alterations in their structure.

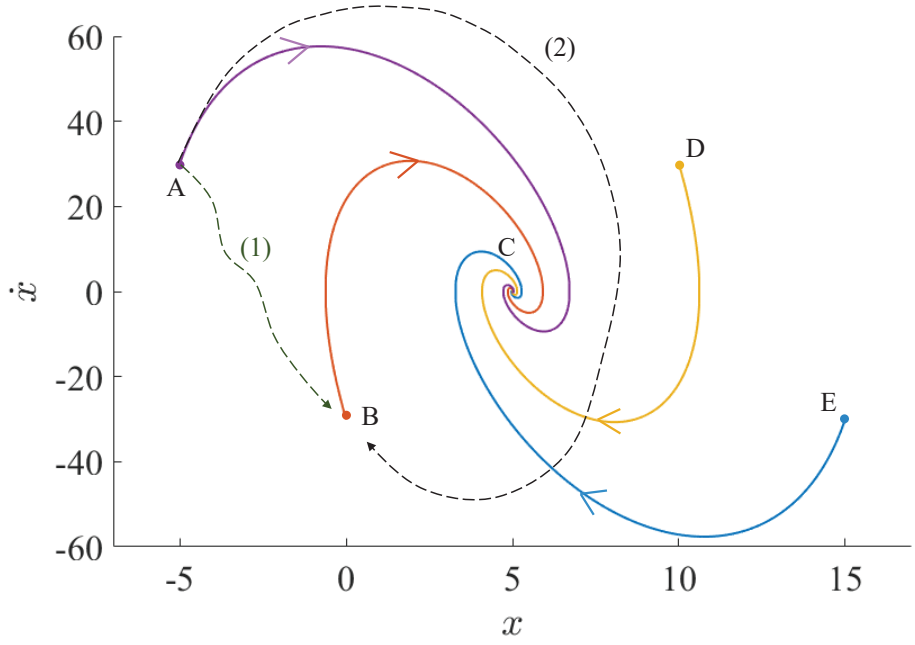

Figure 4.2: Phase diagram, it exhibits the motion characteristics, namely the spiral convergence, of the system. The four solid lines in the diagram represent the motion behaviors under different initial conditions, while the dashed lines show the trajectories under two different control strategies.

Then considering a mass m on a frictionless surface, the equation of motion is given by:

$$m\ddot{x} + c\dot{x} + k(x - l_1) = u. \tag{4.1}$$

Therefore, its state-space equation can be written as:

$$\begin{bmatrix} \dot{x}_1 \\ \dot{x}_2 \end{bmatrix} = \begin{bmatrix} 0 & 1 \\ -\frac{k}{m} & -\frac{c}{m} \end{bmatrix} \begin{bmatrix} x_1 \\ x_2 \end{bmatrix} + \begin{bmatrix} 0 \\ \frac{1}{m} \end{bmatrix} u + \begin{bmatrix} 0 \\ \frac{kl_1}{m} \end{bmatrix}, \tag{4.2}$$

where

$$x_1 := x, \quad x_2 := \dot{x}. \tag{4.3}$$

As the spring-damper system is the smallest unit of morphology, we can refer to the current system as morphology No. 1.

It can be easily observed from Eq. 4.2 that without external input, the morphology No. 1 will ultimately converge to state $[l_1, 0]^{\mathrm{T}}$ by its own dynamic characteristics when m, k and c are positive.

Its simulation results are shown by the solid line in Figure 4.2, where the simulation parameters are set as follows: $m = 1, c = 10, k = 100, l_1 = 5$.

In this figure, points A, B, D, and E represent four different arbitrary initial states, and it can be observed that under the dynamic characteristics of the current morphology, all states converge to point C. If we want to control state A to reach state B, there are generally two typical control methods, corresponding to the two dashed lines (1) and (2) in Figure 4.2.

The dashed line (1) refers to PID control, which uses the difference between the current state and the target state as feedback to directly reach point B. From the phase diagram, this trajectory is the shortest. However, this type of control can be seen as a real-time confrontation between control and system characteristics, just like constantly resisting the vortex convergence characteristics of the system during the process from A to B. This real-time resistance will increase the control cost and reduce the control effect. In addition, PID control is heavily dependent on feedback coefficients. After tuning a set of feedback coefficients, it only adapts to the current system, which means it balances and resists the system's convergence characteristics. When replaced with another system, the control effect brought by the current PID feedback coefficients also drops significantly.

This type of control does not need to consider the system characteristics, which is both a disadvantage and an advantage. It is a disadvantage because it lacks repeatability and accuracy, but it is an advantage because it is straightforward and can be used in situations where precision is not critical.

Control that takes into account the system characteristics, as shown by the dashed line (2), is often based on the solution or approximate solution of the system's motion equations, to determine the motion or motion trend, and to design the target trajectory or control input. Although such control involves complex calculations and high difficulty, it produces good control effects by utilizing the system characteristics. Dashed line (2) uses the characteristic of spiral convergence, and although the distance seems much longer than (1), it works with the system's tendencies and produces better results with less effort.

MBC is different from these two types of control. Its ultimate goal is to change the current system's dynamic characteristics by manipulating the inputs, in this case, the convergence characteristics, to enable the system to converge to state B from any initial state A.

This is an example of controlling the morphology No. 1 , the spring-damping system with nature length l_1, to reach the state $[x_d, 0]^{\mathrm{T}}$ through MBC.

Here, considering the control target as $[x_d, 0]^{\mathrm{T}}$, we can design the morphology No. 2, i.e., a

spring-damper system with natural length x_d without any external input. Its state-space equation can be written as

$$\begin{bmatrix} \dot{x}_1 \\ \dot{x}_2 \end{bmatrix} = \begin{bmatrix} 0 & 1 \\ -\frac{k}{m} & -\frac{c}{m} \end{bmatrix} \begin{bmatrix} x_1 \\ x_2 \end{bmatrix} + \begin{bmatrix} 0 \\ \frac{kx_d}{m} \end{bmatrix}, \tag{4.4}$$

It will naturally converge to the target $[x_d, 0]^{\mathrm{T}}$ as mentioned before. In practical situations, it is not feasible to change the morphology of a spring by replacing it. Therefore, the core idea of MBC is to control the input to transform morphology 1 into morphology 2. To make Eq. 4.2 equal to Eq. 4.4, we can obtain u in Eq. 4.2 as follows:

$$u = k(x_d - l_1). \tag{4.5}$$

This means that by adding input u to morphology No. 1, it can have the same characteristics as morphology No. 2, thus changing its morphology characteristics, namely the convergence characteristics, through control input, and naturally achieving the control target.

Here, as a summary of the MBC method, the first step is to determine the self-morphology, which is morphology No. 1. The second step is to design the ideal morphology No. 2, so that it can achieve the control objective through its own characteristics, and its self-convergence characteristics should meet the requirements of control, such as response speed and control precision. The third step is to use the control input u of morphology No. 1 to transform it into morphology No. 2, thereby obtaining the self-convergence characteristics of morphology No. 2.

4.3 Morphological Changes of RWT

In the previous chapter, the morphologies corresponding to walking and crawling are discovered and discussed separately. In this section, we use the aforementioned MBC to achieve the morphological changes of the RWT, and validate them through passive gaits.

The implementation of different morphologies is based on different structural characteristics, so we provide the equations of motion for the morphology and the crawling morphology separately:

$$\boldsymbol{M}\ddot{\boldsymbol{q}} + \boldsymbol{h} = \boldsymbol{F}_{w-\mathrm{con}} + \boldsymbol{F}_{w-\mathrm{cou}}, \tag{4.6}$$

$$\boldsymbol{M}\ddot{\boldsymbol{q}} + \boldsymbol{h} = \boldsymbol{F}_{c-\mathrm{con}} + \boldsymbol{F}_{c-\mathrm{cou}}. \tag{4.7}$$

The subscripts w and c represent morpholog corresponding to walking and crawling morphology, respectively. Based on Eq. 2.2 in Chapter 2, the motion equations can be rewritten as follows:

$$\boldsymbol{M}\ddot{\boldsymbol{q}} + \boldsymbol{h} = \boldsymbol{F}_{w-\mathrm{con}} + \boldsymbol{S}_w \boldsymbol{f}_w, \tag{4.8}$$

$$\boldsymbol{M}\ddot{\boldsymbol{q}} + \boldsymbol{h} = \boldsymbol{F}_{c-\mathrm{con}} + \boldsymbol{S}_c \boldsymbol{f}_c \tag{4.9}$$

where

$$\boldsymbol{S}_w := \boldsymbol{J}_w^{\mathrm{T}} \boldsymbol{D}_w \boldsymbol{T}_w, \tag{4.10}$$

$$\boldsymbol{S}_c := \boldsymbol{J}_c^{\mathrm{T}} \boldsymbol{D}_c \boldsymbol{T}_c. \tag{4.11}$$

Considering the control input as the tension in each string, denoted by $\boldsymbol{u}_w/\boldsymbol{u}_c$, the motion equations can be written as:

$$\boldsymbol{M}\ddot{\boldsymbol{q}} + \boldsymbol{h} = \boldsymbol{F}_{w-\mathrm{con}} + \boldsymbol{S}_w(\boldsymbol{f}_w + \boldsymbol{u}_w), \tag{4.12}$$

$$\boldsymbol{M}\ddot{\boldsymbol{q}} + \boldsymbol{h} = \boldsymbol{F}_{c-\mathrm{con}} + \boldsymbol{S}_c(\boldsymbol{f}_c + \boldsymbol{u}_c). \tag{4.13}$$

Here, we set the control objective as using the control input $\boldsymbol{u}_w$ to enable the morphology of RWT that corresponding to walking change to crawling.

The first step is to determine the current morphology, which is represented by Eq. 4.12. The second step is to identify the target morphology, represented by Eq. 4.13. It should be noted that the implementation of crawling is achieved through self-convergence characteristics without any external input in this morphology, so $\boldsymbol{u}_c$ is set to $\boldsymbol{0}$. The third step is to design $\boldsymbol{u}_w$ to add to the morphology corresponding to walking, in order to achieve the crawling gait characteristics. So we obtain the equation for morphology of walking:

$$\ddot{\boldsymbol{q}} = \boldsymbol{M}^{-1}(\boldsymbol{F}_{w-\mathrm{con}} + \boldsymbol{S}_w(\boldsymbol{f}_w + \boldsymbol{u}_w) - h). \tag{4.14}$$

We set the motion of crawling morphology as our target motion, then

$$\ddot{\boldsymbol{q}}_t = \boldsymbol{M}^{-1}(\boldsymbol{F}_{c-\mathrm{con}} + \boldsymbol{S}_c \boldsymbol{f}_c - h), \tag{4.15}$$

Here, the subscript "t" represents the target. Then, to achieve $\ddot{\boldsymbol{q}} \rightarrow \ddot{\boldsymbol{q}}_t$, the control inputs $\boldsymbol{u}_w$ can be obtained. After obtaining the crawling morphology characteristics by controlling the morphology of walking, it can achieve crawling gait with a different initial state than that of the crawling morphology through its own convergence properties.

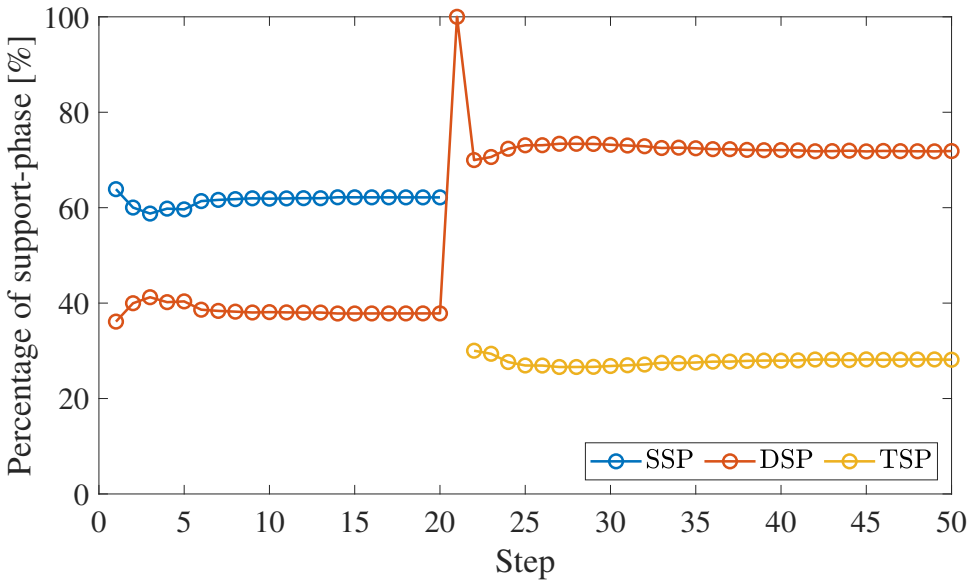

Figure 4.3: Percentage of different support phases over the number of steps

Through the simulations presented in the previous chapter, we selected stable limit cycle gaits for different morphologies that correspondinng to walking and crawling. They correspond to our current and target morphologies, respectively. Starting from an arbitrary initial state in the current morphology, we first achieved the limit cycle gait, which has the highest stability. Then, we applied control input $\boldsymbol{u}$ to change its characteristics and observed the gait pattern.

Figure 4.3 shows the corresponding simulation results, where the x-axis represents the step number, and the y-axis represents the percentage of each support phase in each step. We can observe that the walking gait consists of SSP and DSP, gradually forming a stable limit cycle gait before 20 steps. After that, we applied input $\boldsymbol{u}_w$, and in the current step, the morphology began to transform. The transition is accomplished by the DSP reaching 100% and later evolved into a crawling gait consisting of DSP and TSP. As the step number increased, the gait gradually formed a stable limit cycle gait, indicating that we successfully achieved the crawling gait characteristics in the current morphology by applying control input $\boldsymbol{u}_w$ and implemented the corresponding movement. This demonstrates that MBC can enable a transformation of one morphology to another single morphology.

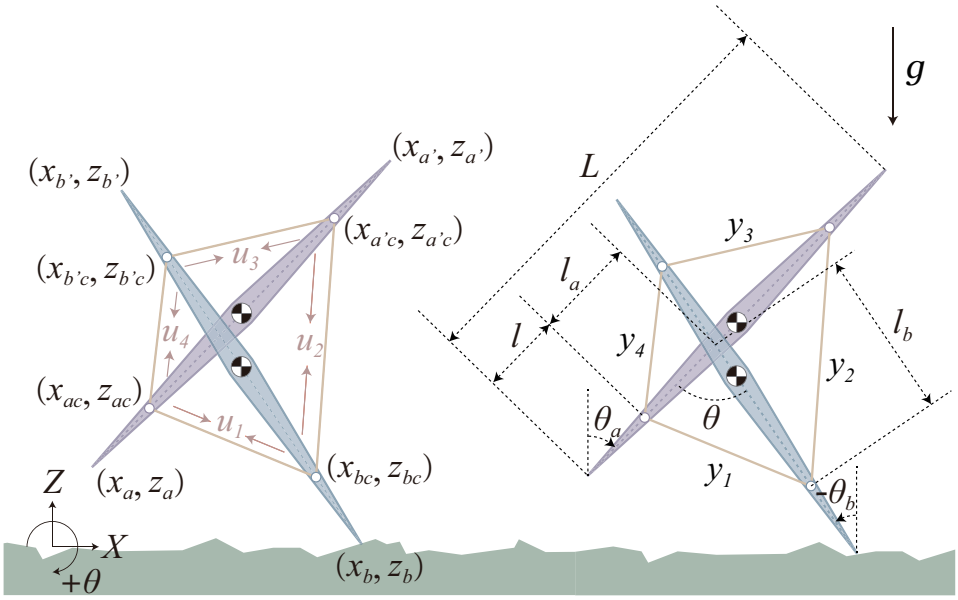

Figure 4.4: Simplified RWT model for control

4.4 A Simplified RWT Model and Flatland Locomotion

MBC can not only transform one morphology into another as demonstrated in the previous section but also be used to track continuous changes in morphology/shape. Therefore, in this section, we will utilize MBC to control the SRWT to achieve different morphologies/shapes and thus enable locomotion.

4.4.1 Model introduction

As the minimal model of passive gaits, RWT requires that the leg angle at touchdown is less than 90 degrees to preserve some kinetic energy when the swing leg collides with the ground, hence the necessity of three legs. However, as a control model, this condition is no longer required, and therefore, two rods are sufficient, which can further simplify the model's complexity.

As depicted in Figure 4.4, the Simplified RWT (SRWT) consists of two identical rods, labeled as Leg A and Leg B, which are connected by four massless flexible strings. These strings can be pulled by an actuator using a control input u_j [N], where $j \in [1, 4]$. The distance from the connection point to the end of each rod is l [m]. The rods have a length of L [m], weight of m [kg], and moment of inertia of I [kg·m^2]. Additionally, their angular positions with respect to the vertical axis are denoted as θ_a [rad] and θ_b [rad], respectively.

Let $\boldsymbol{q} = \begin{bmatrix} x_a & z_a & \theta_a & x_b & z_b & \theta_b \end{bmatrix}^{\mathrm{T}}$ be the generalized coordinate vector, and the equation of motion for the robot during the SSP or DSP is given by:

$$\boldsymbol{M}\ddot{\boldsymbol{q}} + \boldsymbol{h} = \boldsymbol{F}_{\mathrm{con}} + \boldsymbol{S}\boldsymbol{u}. \tag{4.16}$$

The specific constraint force calculation and collision calculation are consistent with the methods described in the second chapter, and the detail of control inputs is same as Eq. 4.8-4.11, therefore it will not be repeated here.

Here we have four inputs, but there is no direct correlation between the four inputs and the forward motion. Therefore, we will focus on exploring the relationship between the inputs and forward motion. We use the clockwise torque of the stance leg as the standard for forward movement. For the control matrix $\boldsymbol{S}\boldsymbol{u}$, the bottom row represents the impact of the four control inputs on the forward torque.

$$\tau = \begin{bmatrix} \mathbf{0}_{5\times 6} \\ \mathbf{1}_{1\times 6} \end{bmatrix} \boldsymbol{S}\boldsymbol{u}, \tag{4.17}$$

The τ represents the clockwise torque on the stance leg, then taking the partial derivatives of a with respect to $\boldsymbol{u}$ yields the influence of the control inputs on the clockwise torque, which can be calculated as followed.

$$\begin{bmatrix} \tau_{u_1} \\ \tau_{u_2} \\ \tau_{u_3} \\ \tau_{u_4} \end{bmatrix} = \begin{bmatrix} \frac{\partial \tau}{\partial u_1} \\ \frac{\partial \tau}{\partial u_2} \\ \frac{\partial \tau}{\partial u_3} \\ \frac{\partial \tau}{\partial u_4}. \end{bmatrix} \tag{4.18}$$

Figure 4.5 illustrates the influence of the four inputs on the clockwise moment of the stance leg for various postures based on Eq. 4.18. The red color represents positive influence, while the blue color represents negative influence. To calculate i-th percentage, we use the following formula:

$$i-\text{th Percentage} = \frac{\tau_{\mathrm{u_i}}}{\sum_{\mathrm{i}=1}^{4} |\tau_{\mathrm{u_i}}|}. \tag{4.19}$$

In Figure 4.5, the vertical leg represents the stance leg. It can be observed that the tension in the two strings to the right of the stance leg contributes to the forward motion of the SRWT, but the effect varies depending on the SRWT's posture.

Based on Figure 4.5, we can design its shape change to actively maximize the utilization of the contraction of the two strings on the right and achieve forward motion. It should be noted that here we can only ensure the necessary condition for forward movement: the forward torque

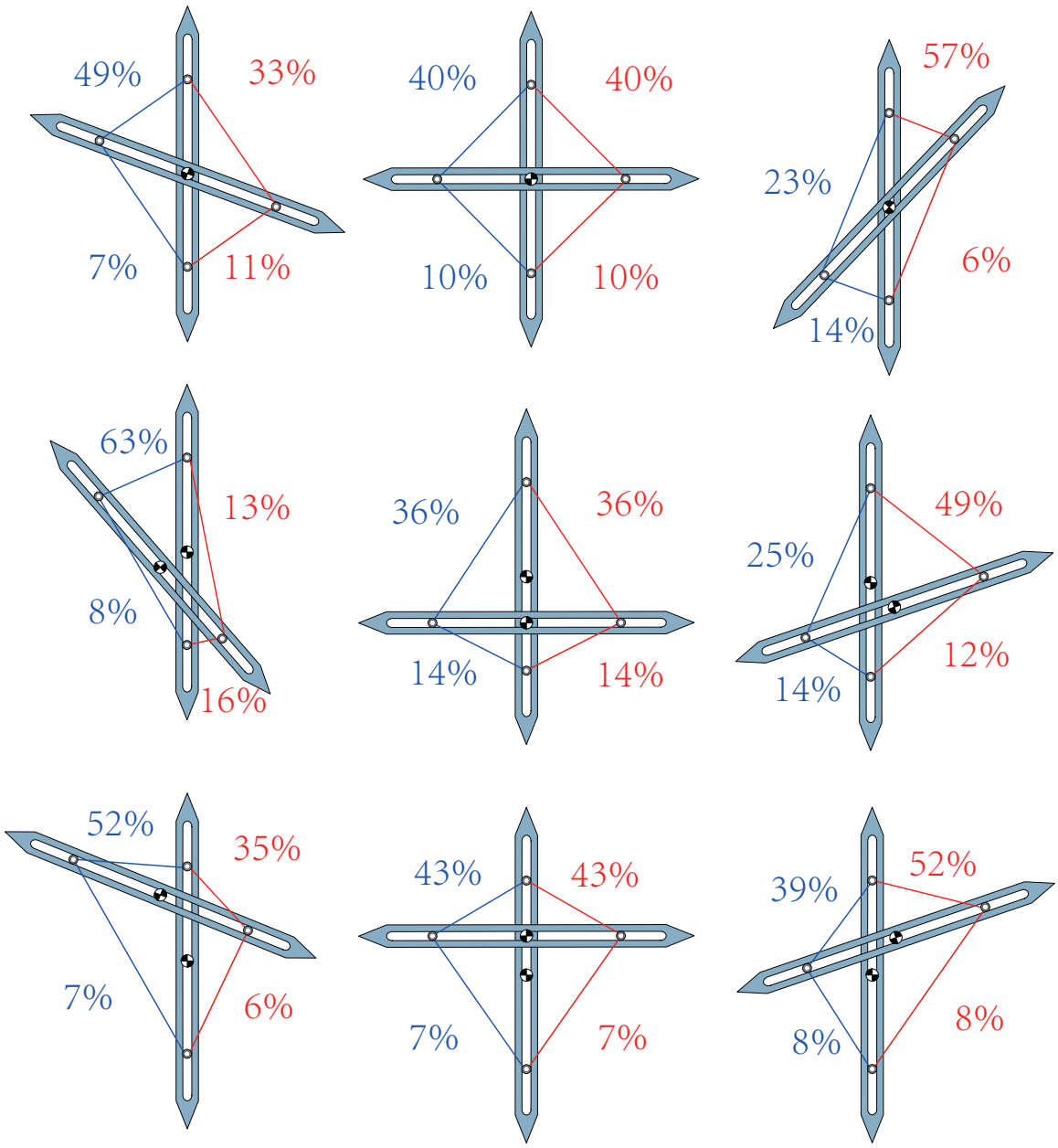

Figure 4.5: Effect of tension on the forward torque in different postures.

of the supporting leg, while other factors such as the motion of the swing leg are unknown. Therefore, the overall stability of SRWT still needs to be ensured by its own characteristics.

4.4.2 Design of motion postures

To achieve an arbitrary posture, only a maximum of three string tensions (control inputs) are needed. Any additional control inputs will be set to zero during the robot's continuous motion. Note that this indeterminate redundancy in control inputs is unavoidable, therefore we need to

simplify its degrees of freedom.

The length of the four strings $\boldsymbol{y}$ can be determined by three parameters: l_a [m], l_b [m], and θ [rad], as shown in Figure 4.4. The geometric relationships are as follows:

$$\boldsymbol{y} := \begin{bmatrix} y_1 \\ y_2 \\ y_3 \\ y_4 \end{bmatrix} = \begin{bmatrix} \sqrt{l_a^2 + l_b^2 - 2l_a l_b \cos\theta} \\ \sqrt{l_b^2 + \hat{l_a}^2 - 2l_b \hat{l_a} \cos(\pi - \theta)} \\ \sqrt{\hat{l_a}^2 + \hat{l_b}^2 - 2\hat{l_a}\hat{l_b} \cos\theta} \\ \sqrt{l_a^2 + \hat{l_b}^2 - 2l_a \hat{l_b} \cos(\pi - \theta)} \end{bmatrix}, \tag{4.20}$$

where

$$\hat{l_a} := L - 2l - l_a, \tag{4.21}$$

$$\hat{l_b} := L - 2l - l_b. \tag{4.22}$$

In this study, the variation of string length is to follow a fifth-order function of time, given by:

$$\boldsymbol{y}_d(t) = \begin{cases} \sum_{k=0}^{5} a_k t^k, & 0 < t \leqslant T_{set} \\ \sum_{k=0}^{5} a_k T_{set}^k, & t > T_{set} \end{cases}, \tag{4.23}$$

where T_{set} [s] is the target control period and determined with the consideration of smoothly connecting the initial position and initial velocity. Thus following boundary conditions should be satisfied:

$$\begin{aligned} &\boldsymbol{y}_d(0) = \boldsymbol{y}(0), \quad \dot{\boldsymbol{y}}_d(0) = \boldsymbol{0}, \quad \ddot{\boldsymbol{y}}_d(0) = \boldsymbol{0}, \\ &\boldsymbol{y}_d(T_{set}) = \boldsymbol{y}(T_{set}), \quad \dot{\boldsymbol{y}}_d(T_{set}) = \boldsymbol{0}, \quad \ddot{\boldsymbol{y}}_d(T_{set}) = \boldsymbol{0}. \end{aligned} \tag{4.24}$$

Accordingly, each coefficient of Eq. (4.23) can be obtained by combining Eq. (4.23) and Eq. (4.24). Here, $\boldsymbol{y}(0)$ represents the current position after one step, while $\boldsymbol{y}(T_{set})$ represents the target position that the robot should reach after one control period.

In order to achieve cyclic walking of SRWT, it is necessary that the posture after one step is equal to the posture at the beginning of the next step, as shown in Figure 6.9. However, since the coordinates are reset after each step, i.e., $L - 2l - l_a^- \rightarrow l_b^+$, $l_b^- \rightarrow l_a^+$, $\pi - \theta^- \rightarrow \theta^+$. A fixed target posture can ensure continuous cyclic walking, i.e., limit cycle gait. Through the geometric relationship in Figure 4.5, we can conclude that an increase in l_a during one step is a necessary condition, while a smaller l_b can provide enough space for l_a to increase in the next step.

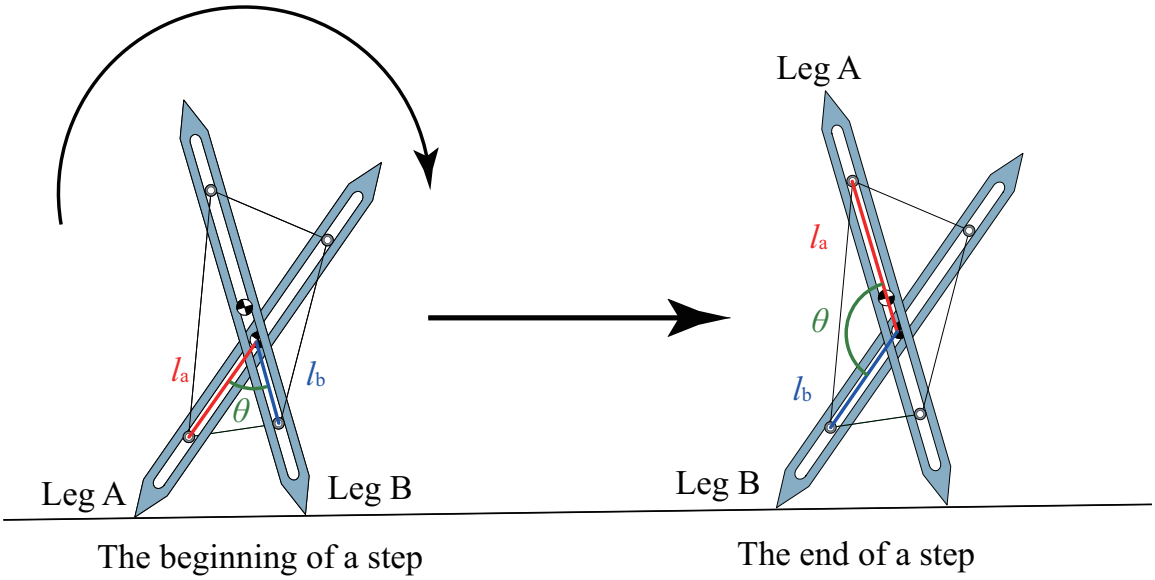

Figure 4.6: Posture change in one step

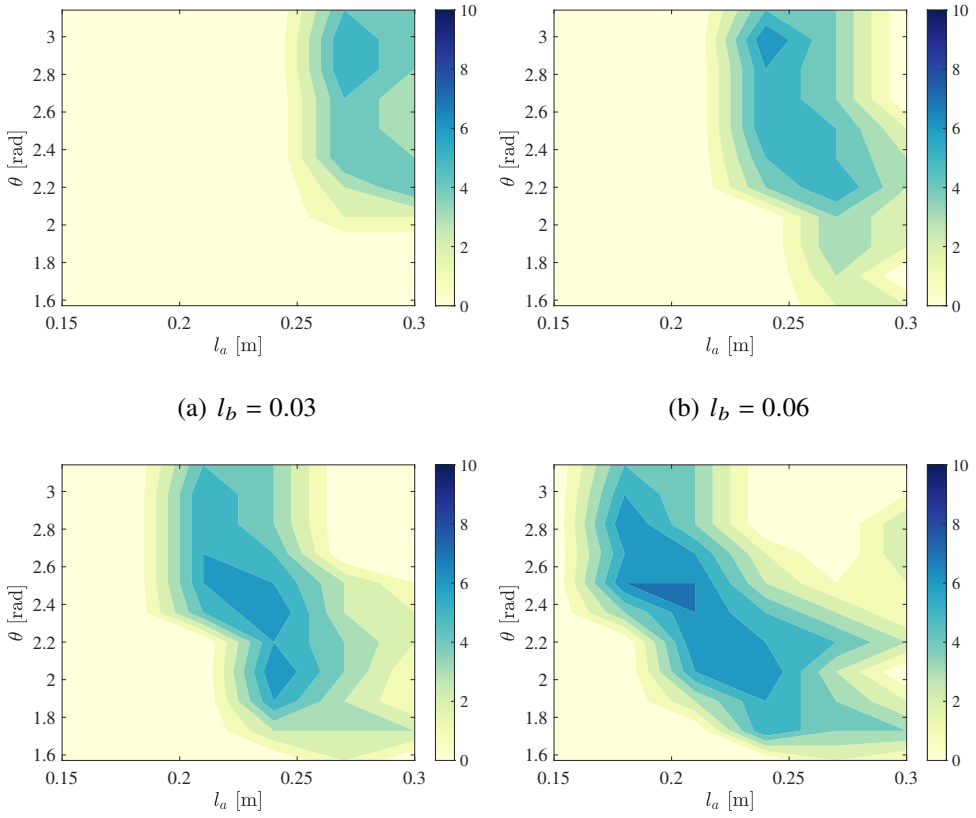

Figure 4.7: Simulation results of walking based on different target postures

4.4.3 Implementation of mobility

Based on the above variation criteria, we investigated the walking outcomes of various target postures under MBC with the parameter setting as Table 4.1. The results are shown in Figure

4.7. Here, the variation speed of the target posture is constrained by T_{set}, while the convergence speed of the corresponding posture is determined by its own ideal characteristics. The range of T_{set} is from 0.3 [s] to 2 [s] with an interval of 0.1. The colorbar in the graph represent the number of successful trials which indicate the convergence range of the corresponding posture, with higher values indicating larger convergence range, and 0 indicating a failed trial.

4.4.4 Typical gait

Among these feasible regions, we also observed period-1 gait, period-2 gait, and chaotic gait. Figure 4.8 shows the simulation results of period-1 gait. From this simulation results, we can observe that the velocity curve is not very smooth, which is determined by its own convergence characteristics. Compared to traditional position control, actively utilizing its own convergence characteristics can greatly enhance the adaptability of the robot and reduce control complexity.

Similarly, Figure 4.9 shows the typical simulation results of its period-2 gait, where two steps are completed within one period. As mentioned earlier, although the robot can converge from any state to the target posture, the process from the current posture to the target posture may not necessarily lead to successful walking due to the conditions required for actual walking and the discrete impact from collisions. The appearance of the period-2 gait is a sign of failure in this regard.

Table 4.1: Physical parameters setting of SRWT for simulation

Symbol	Unit	Description
$m_i, i \in [a, b, c]$	1.5 [kg]	Weight of each leg
$I_i, i \in [a, b, c]$	$mL^2/4[kg \cdot \mathrm{m}^2]$	Inertia moment of each leg
L	0.5 [m]	Length of each leg
l_c	0.1 [m]	Length between connection point and tip point of each leg

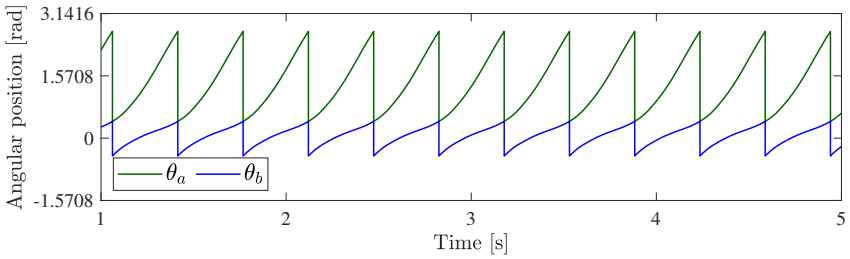

(a) Angular position

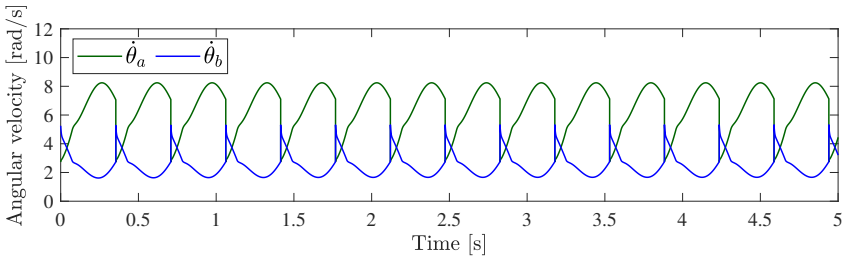

(b) Angular velocity

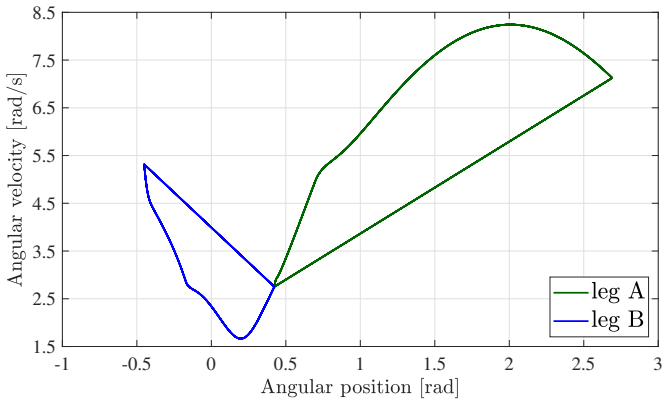

(c) Phases diagram

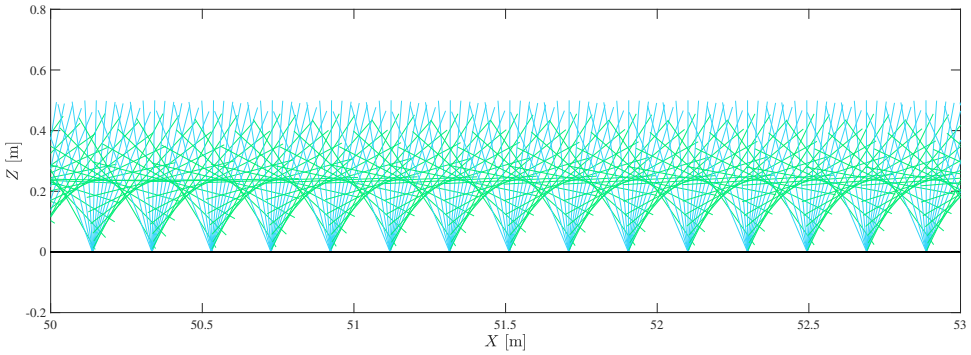

(d) Stick diagram

Figure 4.8: Simulation results of period-1 gait

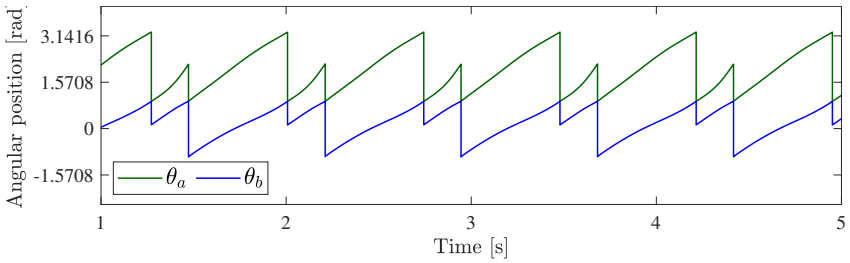

(a) Angular position

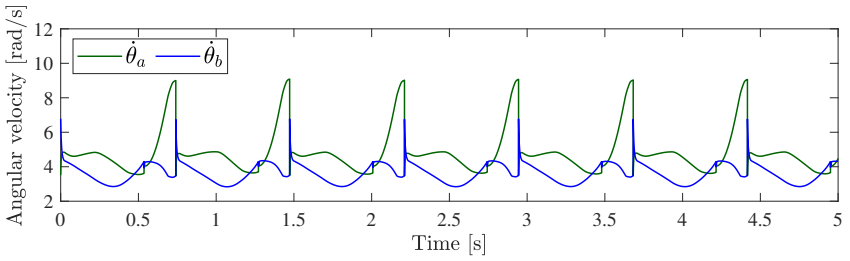

(b) Angular velocity

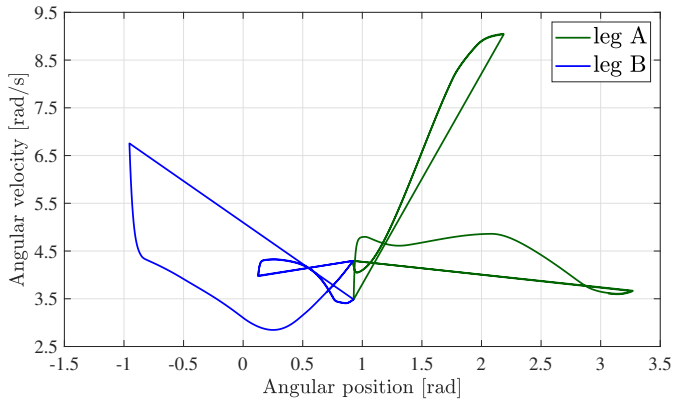

(c) Phases diagram

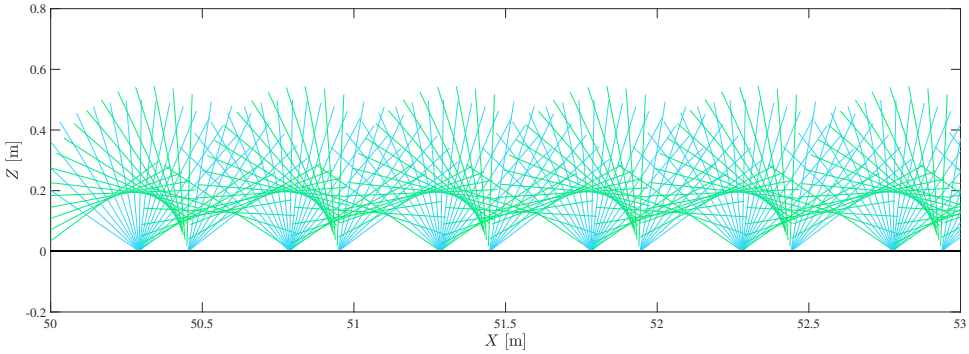

(d) Stick diagram

Figure 4.9: Simulation results of period-2 gait

4.4.5 Stability analysis

The Poincaré mapping method is a commonly used dynamic analysis method, widely applied in the research of robot gait stability. In a robot's single-cycle gait, the Poincaré mapping method describes the robot's motion trajectory by mapping each state vector in one gait to the next. Typically, the Poincaré mapping method is applied immediately after the leg collision to ensure the robot's periodic motion. By analyzing the Poincaré mapping method, the stability of the robot's single-cycle gait can be obtained. Specifically, by introducing slight perturbations, the perturbation vectors corresponding to each state vector can be obtained, and then the Jacobian matrix of the state vector can be calculated based on the relationship between the perturbation vector and the mapped state vector. The eigenvalues of the Jacobian matrix can be used to determine whether the robot's single-cycle gait is stable. The Poincaré mapping method provides an effective analytical tool for the study of robot gait stability, with high theoretical research and practical value.

$$\boldsymbol{Q}_{n+1} = \boldsymbol{P}(\boldsymbol{Q}_n). \tag{4.25}$$

The state vector at the beginning of the n^{th} step is denoted as $\boldsymbol{Q}_n$, as the Poincaré section of the Poincaré map of leg motion is typically defined as the instant immediately after the leg collision. The Poincaré map $\boldsymbol{P}$ represents the state vector $\boldsymbol{Q}$ from the current step n to the next step $n+1$. The state vectors are selected in the following manner.

$$\boldsymbol{Q}^* = \boldsymbol{P}(\boldsymbol{Q}^*). \tag{4.26}$$

In the case of periodic motion, the state vectors are self-mapped and the step count is disregarded. However, when a small disturbance is introduced to the steady-state dimension i^{th}, the resulting output of the Poincaré map can be expressed as follows.

$$\boldsymbol{Q}^* + \boldsymbol{\delta}_1^i \;=\; \boldsymbol{P}(\boldsymbol{Q}^* + \boldsymbol{\delta}_0^i) \approx \boldsymbol{P}(\boldsymbol{Q}^*) + \left.\frac{\partial \boldsymbol{P}}{\partial \boldsymbol{Q}}\right|_{\boldsymbol{Q}^*} \boldsymbol{\delta}_0^i \tag{4.27}$$

Represented by the vector $\boldsymbol{\delta}_0^i$, the perturbations in the steady-state i^{th} dimension give rise to a resulting deviation defined as $\boldsymbol{\delta}_1^i$. By replacing equation (4.26) with equation (4.27) and applying it to the perturbations in each dimension separately, we can obtain the gradient matrix.

$$\left.\frac{\partial \boldsymbol{P}}{\partial \boldsymbol{Q}}\right|_{\boldsymbol{Q}^*} \approx \begin{bmatrix} \boldsymbol{\delta}_1^1 & \boldsymbol{\delta}_1^2 & \cdots & \boldsymbol{\delta}_1^n \end{bmatrix} \begin{bmatrix} \boldsymbol{\delta}_0^1 & \boldsymbol{\delta}_0^2 & \cdots & \boldsymbol{\delta}_0^n \end{bmatrix}^{-1} \tag{4.28}$$

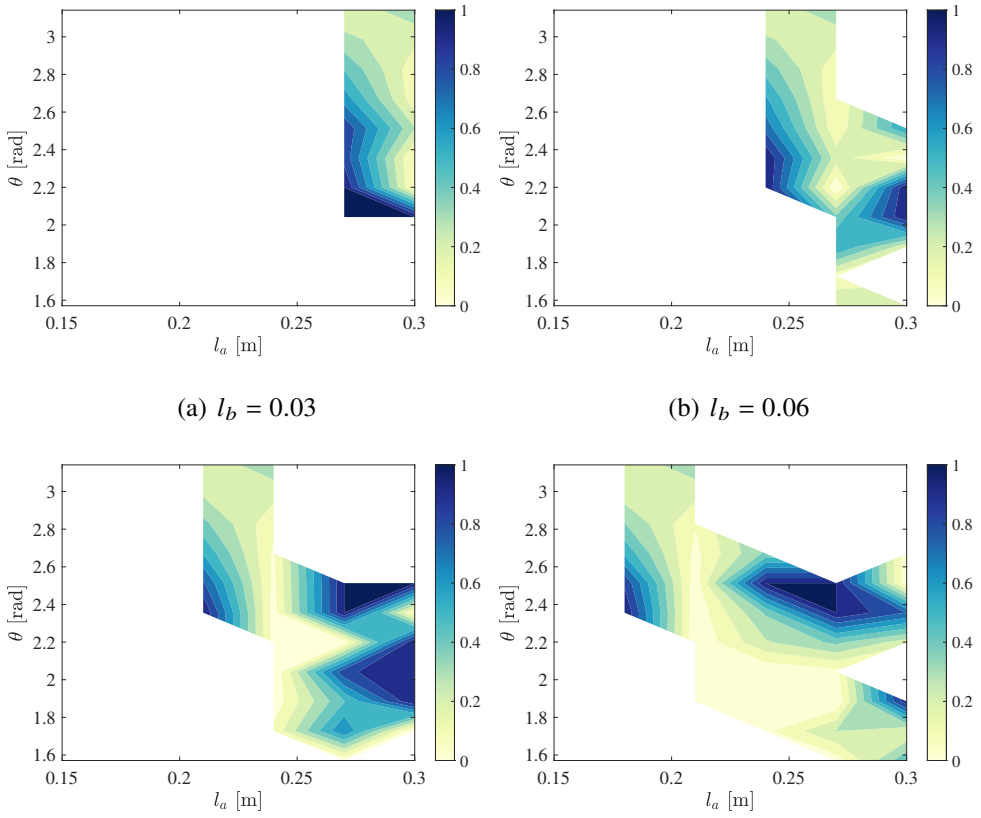

(a) $l_b = 0.03$ (b) $l_b = 0.06$

(c) $l_b = 0.09$ (d) $l_b = 0.12$

Figure 4.10: Different stability under various target postures

To determine the local stability of the gait of the robot under entrainment control, we examine the eigenvalues λ_i of the matrix $\frac{\partial \boldsymbol{P}}{\partial \boldsymbol{Q}}\Big|_{\boldsymbol{Q}^*}$, which define the response of the i^{th} dimension to a perturbation. If $\max|\lambda_i| < 1$, then the gait is considered locally stable. By applying a small perturbation at the instant after the leg collision and calculating the maximum eigenvalue, we can determine if the gait is stable under entrainment control.

Compared to Figure 4.7, Figure 4.10 incorporates the analysis using the Poincaré map, where blank spaces represent non-periodic gaits or failed walking. The colors less than 1 indicate stability, while the parts of the figure greater than 1 are all represented by 1 to indicate non-convergence. This Figure 4.10 further explains the degree of stability under different control target postures.

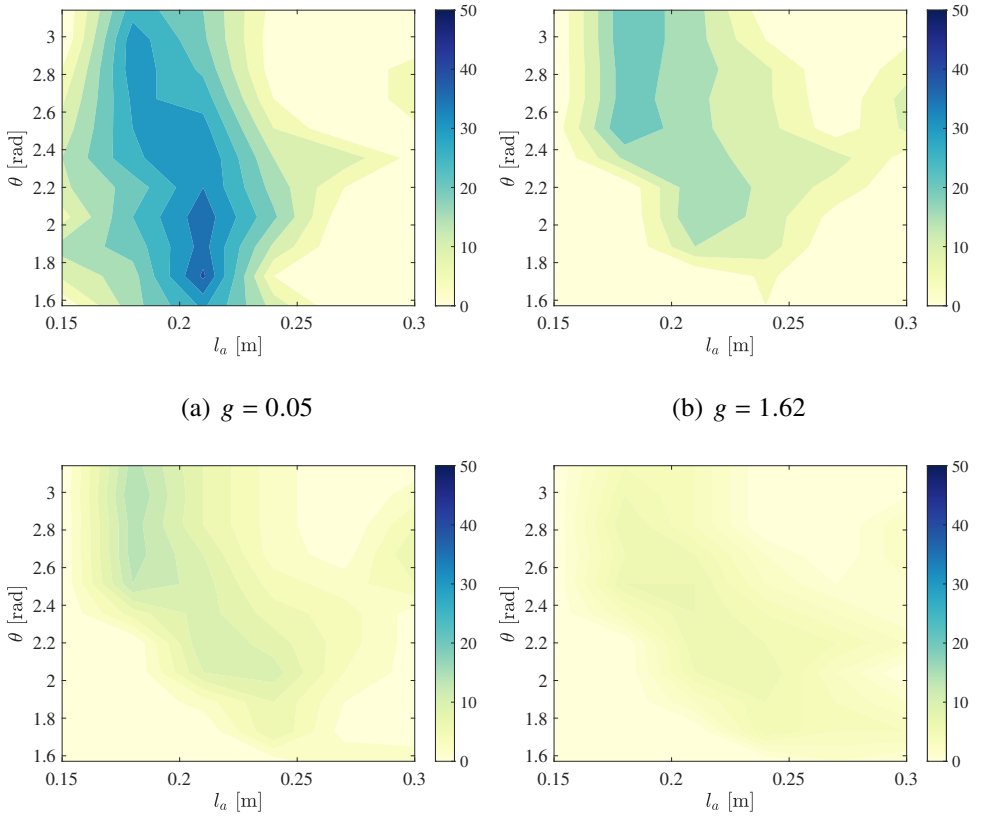

(a) $g = 0.05$ (b) $g = 1.62$

(c) $g = 3.72$ (d) $g = 9.81$

Figure 4.11: Various gravities affect walking success range

4.4.6 Application of SRWT: walking on low-gravity and uneven terrain.

The simulation results of SRWT are presented in Figure 4.7, where the color scale indicates the number of successful trials, demonstrating the range of successful control. Among them, the best result is shown in Figure 4.7(d), which is used as a reference to explore the success rate under different gravities in Figure 4.11. The color scale in Figure 4.11 ranges from 0 to 50, compared to the original range of 0 to 10, showing that SRWT performs better in low-gravity environments. This advantage is based on its self-convergence property, which can better balance various internal forces, such as the constraint force with the ground or the internal coupling elastic force.

We generated the height of the uneven terrain randomly at a ratio of one-tenth of the robot's height and simulated its walking performance. Figure 4.12 (a) displays the altitude of the robot's contact points while walking, while Figure 4.12 (b) shows the speed of each step. The results indicate that the robot can walk on uneven terrain utilizing its own dynamic properties with a

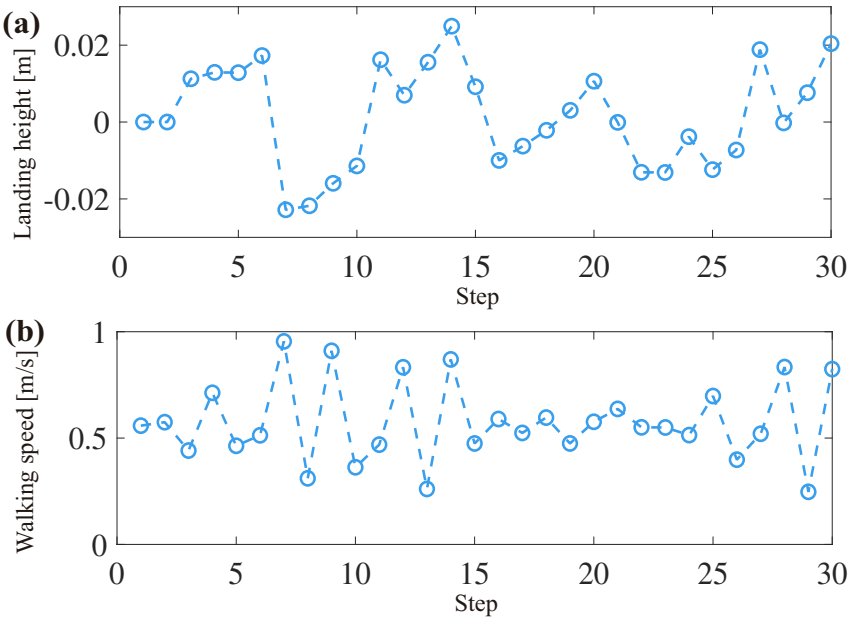

Figure 4.12: Landing height over steps

forward moment.

4.5 Summary and Discussions

Morphology-based control (MBC) is applicable to higher-order or difficult-to-linearize systems, which are often challenging to control directly. In the case of the model in this study, its motion equations are more complex and nonlinear compared to traditional second-order equations due to the high coupling of internal elastic elements. Direct control of such systems is not feasible; however, the convergence characteristics, including convergence speed and target convergence state, can be altered by controlling the inputs. Despite its indirect nature, MBC offers a viable approach. Employing conventional control methods would lead to significant structural variations in this highly sensitive nonlinear system, even if control were achieved, due to any slight disturbance during the experimental process. Optimization can enhance control stability, but it does not bring about substantial changes to such systems. On the other hand, with the use of MBC, the control objective shifts from controlling the position to managing the convergence characteristics of the system. This enables the elimination of any disturbance through the system's inherent convergence property. Though indirect, this method ensures the achievement of the target state and controls the convergence speed, i.e., the motion speed, indirectly.

This is chapter, MBC is applied to the RWT, enabling it to transform its shape from passive

walking to different movement modes, such as crawling, which demonstrates the effectiveness of the control method. This approach enables the control of RWT's single-morphology-to-another-morphology transformation. Moreover, MBC can also realize continuous tracking of the target morphology, achieving the transformation of its posture. Therefore, a simpler SRWT model is proposed based on this approach, which can move on flat ground. The typical period-1 and period-2 gaits are demonstrated and their stability analysis is provided. Finally, some special applications are given, such as adaptation to uneven terrain or better walking performance in low-gravity environments. Compared with traditional position control, MBC is more indirect. It does not directly control the posture, but rather the morphology, which affects the posture through the convergence properties of the morphology. This method has higher adaptability and lower control complexity.

Chapter 5

Necessary Conditions for Limit Cycle Gait

5.1 Overview

The previous chapter introduced the implementation of gait based on MBC and the stability of gait under different desired postures, while the reasons why gait is stable will be described in detail in this chapter.

As previously mentioned, the difference between MBC and general rigid-body robot control lies in the fact that MBC controls the morphology, and through morphological characteristics such as convergence, achieves the desired posture. This is because the presence of elastic elements leads to a higher-order nonlinear relationship between the control inputs (force or torque) and the control outputs (trajectory position), due to the high coupling of elasticity, resulting in strong nonlinear characteristics. Thus, conventional methods like position control cannot be used, and instead, the system's characteristics must be utilized. MBC leverages the unique properties of the morphology, specifically its convergence properties, to control the convergence position of a high-order strongly nonlinear system by modifying the morphology, thereby achieving changes in position.

In this study, the proposed method controls the magnitude of elasticity by controlling the length of the string, which in turn allows for different morphological characteristics and ultimately achieves different equilibrium postures, i.e., controlling the desired posture. Although the system obtains different morphological characteristics through control, its behavior is manifested in the change of its own posture, and the influence on gait is solely related to changes in self-posture. To further study the necessary conditions for posture changes and gait stability,

the control effect produced by MBC can be ignored, and only the rigid structural changes can be considered. Hence, this study proposes the following rigid model, where the posture changes can be equivalent to the control results generated by MBC, thus enabling the investigation of factors affecting gait.

Using this model allows us to avoid the influence of elastic elements on control and focus more on the variations in motion. Furthermore, the motion variations can be achieved through virtual inputs, which provide control results similar to MBC but in a simpler and more implementable manner. In the previous chapter, controlling the SRWT required four inputs, and due to the complex mapping relationship between the inputs and generalized coordinates caused by controlling only the strings, it was challenging. However, the rigid model proposed in this chapter reduces the redundancy and complexity of the mapping by lowering the number of inputs. Additionally, although the inputs of this rigid model are virtual based on MBC, meaning the effect of four redundant actual inputs can be achieved through three virtual inputs, these virtual inputs still possess general physical significance and can be implemented in practice, making them reasonable.

Therefore, in this chapter, the proposed model is used to validate the achievement of limit cycle gaits for different control objectives, thereby demonstrating the necessary conditions for generating limit cycle gaits.

5.2 Mathematical Modeling

The model shows in Figure 5.1 consists of two rods with the same degrees of freedom as SRWT, with the only difference being the absence of elastic elements and the method of input. There are three control inputs in this case, each controlling the length of l_a, l_b, and the angle of θ.

Let $\boldsymbol{q} = \begin{bmatrix} x & z & \theta_1 & l_a & l_b & \theta_2 \end{bmatrix}^{\mathrm{T}}$ be the generalized coordinate vector, the robot equation of motion then becomes:

$$\boldsymbol{M}\ddot{\boldsymbol{q}} + \boldsymbol{h} = \boldsymbol{J}^{\mathrm{T}}\boldsymbol{\lambda} + \boldsymbol{S}\boldsymbol{u}, \tag{5.1}$$

where $\boldsymbol{M}$ represents the inertia matrix, $\boldsymbol{h}$ represents the combination of central force, Coriolis force and gravity terms. $\boldsymbol{J}^{\mathrm{T}}\boldsymbol{\lambda}$ is the constraint forces term. In this case, the three control inputs respectively govern the lengths of l_a and l_b as well as the angle $\theta := \theta_1 - \theta_2$. Then the control

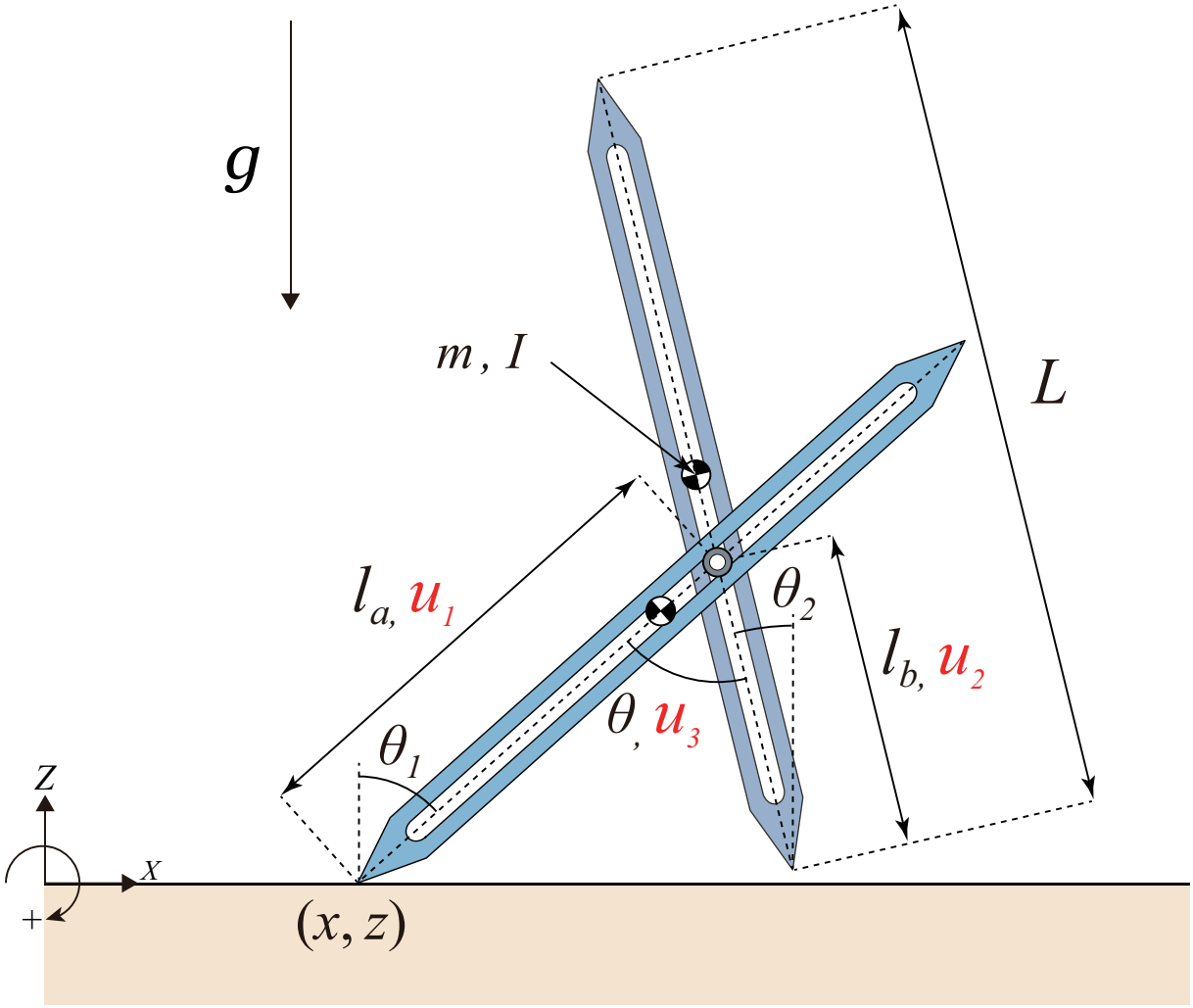

Figure 5.1: Mathematical model for rigid structures

torque vector $\boldsymbol{Su}$ is then determined as

$$\boldsymbol{S}u = \begin{bmatrix} 0 & 0 & 0 & 1 & 0 & 0 \\ 0 & 0 & 0 & 0 & 1 & 0 \\ 0 & 0 & 1 & 0 & 0 & -1 \end{bmatrix}^{\mathrm{T}} \begin{bmatrix} u_1 \\ u_2 \\ u_3 \end{bmatrix}. \tag{5.2}$$

Considering the constraint that the grounding point do not experience relative sliding, according to the previous method, the constraint force $\boldsymbol{\lambda}$ can be determined as

$$\boldsymbol{\lambda} = -\boldsymbol{X}^{-1}\boldsymbol{J}\boldsymbol{M}^{-1}(\boldsymbol{Su} - \boldsymbol{h}), \tag{5.3}$$

where $\boldsymbol{X} := \boldsymbol{J}\boldsymbol{M}^{-1}\boldsymbol{J}^{\mathrm{T}}$ and

$$\boldsymbol{J} = \begin{bmatrix} 1 & 0 & 0 & 0 & 0 & 0 \\ 0 & 1 & 0 & 0 & 0 & 0 \end{bmatrix}^{\mathrm{T}}. \tag{5.4}$$

The control output is

$$\boldsymbol{y} = \begin{bmatrix} l_a \\ l_b \\ \theta \end{bmatrix}. \tag{5.5}$$

By taking the second derivative of the control output with respect to time, we can get

$$\ddot{\boldsymbol{y}} = \boldsymbol{S}^{\mathrm{T}} \ddot{\boldsymbol{q}}. \tag{5.6}$$

Therefore, for achieving $\boldsymbol{v} := [v_1, v_2, v_3]^{\mathrm{T}} \rightarrow \ddot{\boldsymbol{y}}$, the control inputs can be derived as

$$\boldsymbol{u} = \boldsymbol{A}^{-1} \left(\boldsymbol{v} + \boldsymbol{B} \right), \tag{5.7}$$

where

$$\boldsymbol{A} := \boldsymbol{S}^{\mathrm{T}} \boldsymbol{M}^{-1} \boldsymbol{Y} \boldsymbol{S}, \tag{5.8}$$

$$\boldsymbol{B} := \boldsymbol{S}^{\mathrm{T}} \boldsymbol{M}^{-1} \boldsymbol{Y} \boldsymbol{h}, \tag{5.9}$$

$$\boldsymbol{Y} := \boldsymbol{I}_6 - \boldsymbol{J}^{\mathrm{T}} \boldsymbol{X}^{-1} \boldsymbol{J} \boldsymbol{M}^{-1}. \tag{5.10}$$

In this model, we have three control inputs, and for the sake of example, let's focus on u_1 to explain the control method. Considering the effectiveness of control during trajectory variations, we employ Discrete-time Output Deadbeat Control (DODC). We define

$$\xi := l_a - (l_a(T) - l_a(0)). \tag{5.11}$$

Here, T is defined as the control period. It's important to note that the real-time variable t is reset after each step, and its range is limited to 0 to T. When t exceeds T, the system will be locked to ensure the maintenance of its own posture. During this time, the control does not generate any energy output as it is effectively inactive.

The first and second derivatives of ξ are

$$\dot{\xi} = \dot{l}_a, \tag{5.12}$$

$$\ddot{\xi} = \ddot{l}_a = v_1. \tag{5.13}$$

Then the state equation is

$$\frac{\mathrm{d}}{\mathrm{dt}} \begin{bmatrix} \xi \\ \dot{\xi} \end{bmatrix} = \begin{bmatrix} 0 & 1 \\ 0 & 0 \end{bmatrix} \begin{bmatrix} \xi \\ \dot{\xi} \end{bmatrix} + \begin{bmatrix} 0 \\ 1 \end{bmatrix} v_1. \tag{5.14}$$

To satisfy the conditions for Eq. (5.14), the following criteria must be met:

The initial state:

$$\xi(0) = -(l_a(T) - l_a(0)),\ \dot{\xi}(0) = \dot{l}_a(0). \tag{5.15}$$

The target state:

$$\xi(T) = 0,\ \dot{\xi}(T) = 0. \tag{5.16}$$

By discretizing the state equation Eq. (5.14) with respect to $T/2$, we can obtain

$$\begin{bmatrix} \xi[i+1] \\ \dot{\xi}[i+1] \end{bmatrix} = \begin{bmatrix} 1 & T/2 \\ 0 & 1 \end{bmatrix} \begin{bmatrix} \xi[i] \\ \dot{\xi}[i] \end{bmatrix} + \begin{bmatrix} T^2/8 \\ T/2 \end{bmatrix} v_1[i]. \tag{5.17}$$

Here,

$$\xi[i] = \xi(iT/2),\ \dot{\xi}[i] = \dot{\xi}(iT/2),\ v_1[i] = v_1(iT/2). \tag{5.18}$$

Thus, the discretized state space Eq. (5.17) can be organized as

$$\boldsymbol{x}[i+1] = \boldsymbol{A}_d \boldsymbol{x}[i] + \boldsymbol{B}_d v_1[i]. \tag{5.19}$$

Let's define control output as $v_1[i] = \boldsymbol{F}\boldsymbol{x}[i]$, in order to satisfy condition $\boldsymbol{x}[2] = \boldsymbol{0}$ all eigenvalues of $\boldsymbol{A}_d + \boldsymbol{B}_d\boldsymbol{F}$ should be equal to 0. In this case, the feedback gain $\boldsymbol{F}$ is

$$\boldsymbol{F} = \begin{bmatrix} -4/T^2 & -3/T \end{bmatrix}. \tag{5.20}$$

Based on this method, we can obtain the $\boldsymbol{v}$ for each control output.

5.3 Control Purpose and Numerical Results

The stability of limit cycle gait can be reflected using the following formula for the variation of kinetic energy.

$$E_k^-[j+1] = \kappa[j] E_k^-[j] + \Delta E[j+1]. \tag{5.21}$$

In this equation, $E_k^-[j+1]$ represents the kinetic energy at the end of the $j+1$ step, just before the swing leg collides with the ground. $\kappa[j]$ denotes the proportion of kinetic energy loss due to collisions in the j-th step, ranging from 0 to 1 where a value closer to 1 indicates less energy loss, the value of $\kappa[j]$ is related to the posture at the moment of collision, specifically the position of the instantaneous center of mass relative to the contact point of the swing leg with

the ground. $\Delta E[j]$ represents the recovered energy obtained in the j-th step, such as energy provided by the motor.

It is evident that the convergence condition for the series in this equation is for $\kappa[j]$ or $\Delta E[j]$ to be constant. The physical interpretation of this convergence is the achievement of a limit cycle gait. Therefore, in this study, the aim is to investigate the necessary conditions for the limit cycle gait of the current structure by employing different control strategies to make $\kappa[j]$ and $\Delta E[j]$ constant. The objective is to demonstrate the stability conditions for the gait.

5.3.1 Landing posture constant control

The objective of this control is to ensure a consistent posture upon landing. However, mobile robot models are generally underactuated, making it challenging to maintain their motion states. Therefore, this study divides the control into two stages. The first stage focuses on controlling the posture change, aiming to achieve the target posture at time T. It is important to note that the current step cannot end at this point, allowing for transition to the second stage. The second stage aims to maintain the current posture, enabling the robot to fall onto the ground in a fixed posture. This ensures a consistent posture at each collision during the gait.

The physical parameters and control parameters presented in Table 5.1. Here, the setting of the target position is based on the conclusions from the previous chapter, and choosing a relatively small value for T ensures the smooth execution of the first stage.

Table 5.1: Physical parameters and control parameters setting for simulation

Symbol	Unit	Description
m	1 [kg]	Weight of each leg
I	$mL^2/4[kg \cdot \mathrm{m}^2]$	Inertia moment of each leg
L	1 [m]	Length of each leg
T	0.3 [s]	Control period
$l_a(T)$	$0.6L$ [m]	Target position
$l_b(T)$	$0.4L$ [m]]	Target position
$\theta(T)$	$\pi/3$ [rad]	Target position

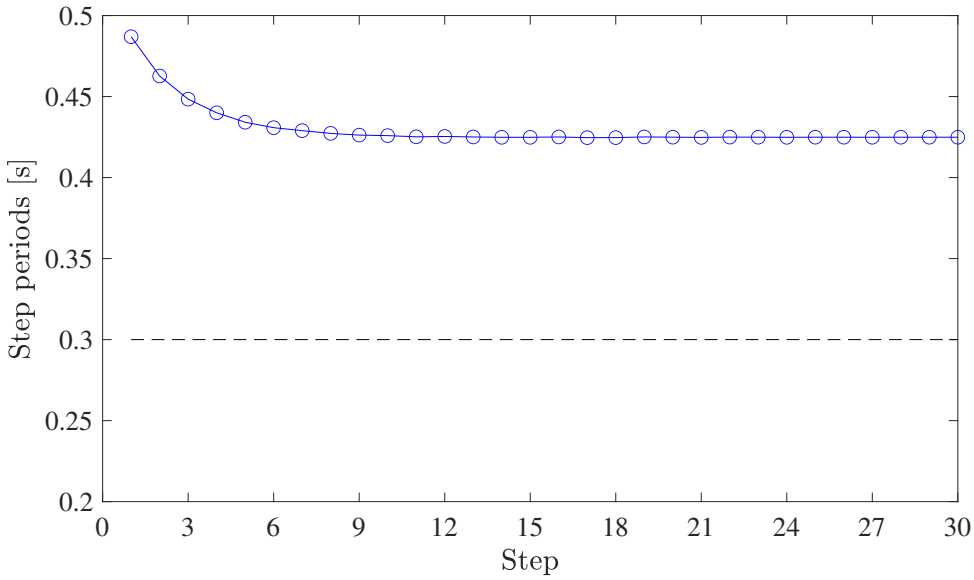

Figure 5.2: Step periods over the number of steps

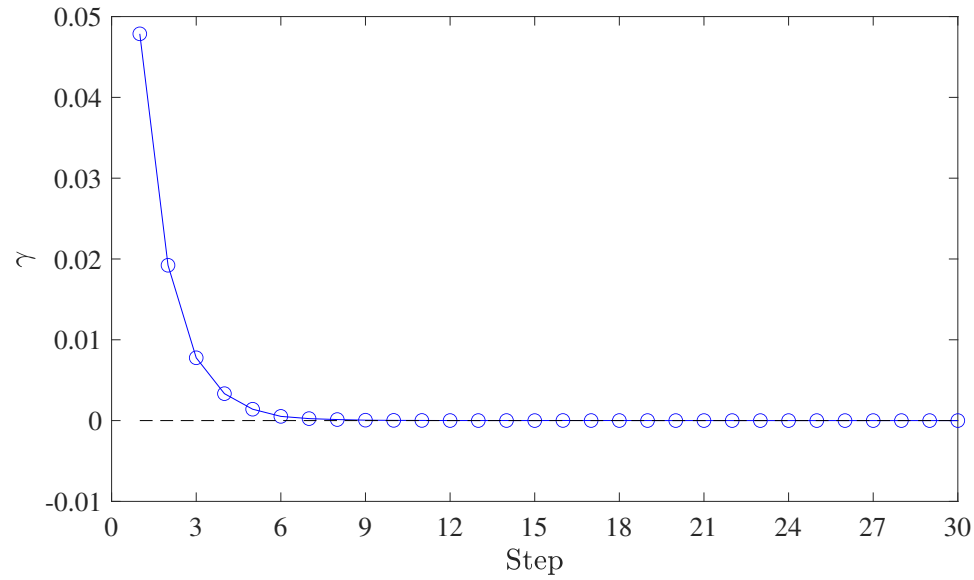

Figure 5.3: State difference over the number of steps

Starting the simulation from any reasonable physical initial state, the simulation results shown in Figure 5.2 illustrate the time for each step, while the dashed line represents the set control period T. It can be observed that the actual time for each step is greater than T, indicating the presence of the two aforementioned stages, namely the control stage and the lock-in stage, which ensure the fixed posture upon touchdown. From the results, a converging trend in the gait can be observed. Figure 5.3 displays the state difference, where we use γ to represent the state

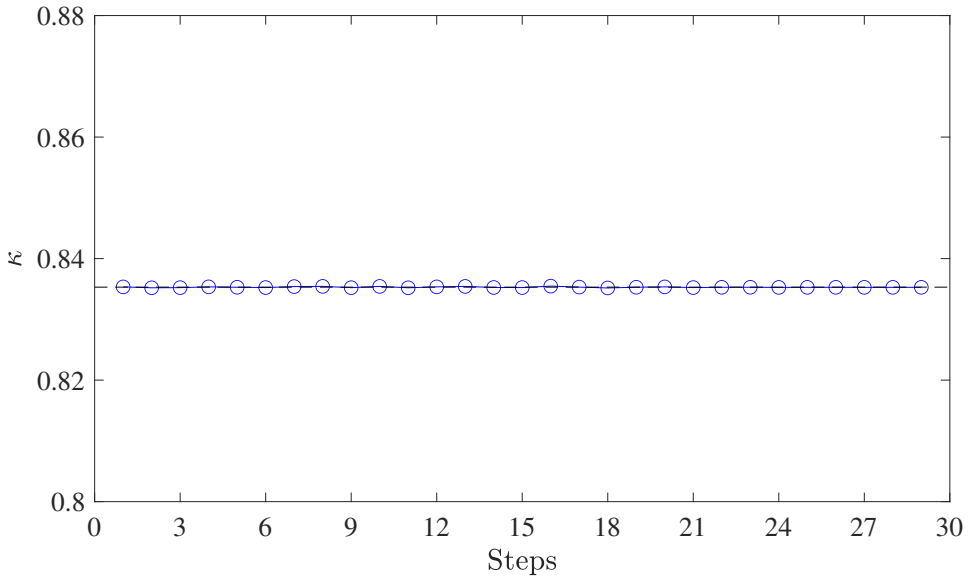

Figure 5.4: Proportion of kinetic energy loss over the number of steps

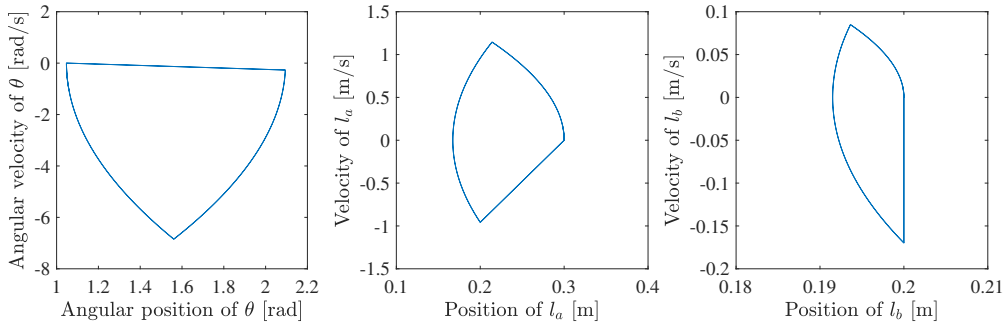

Figure 5.5: Phase diagram with landing posture constant control

difference, specifically defined as follows:

$$\gamma[j+1] = \sqrt{(l_a[j+1] - l_a[j])^2 + (l_b[j+1] - l_b[j])^2 + (\theta[j+1] - \theta[j])^2}. \tag{5.22}$$

It is evident that the state difference converges to zero, indicating that the state of each step has achieved complete consistency, forming a limit cycle gait. The same landing posture results in the same kinetic energy loss ratio, κ. Therefore, from Figure 5.4, it can be observed that when the landing posture is the same, indicating the achievement of the control objective, κ becomes a constant value.

Additionally, Figure 5.5 provides a direct visualization of the realization of the limit cycle gait.

The above results demonstrate the achievement of the control objective, which is to ensure a fixed posture upon landing, thereby ensuring the stability of κ. The fixation of κ enables the

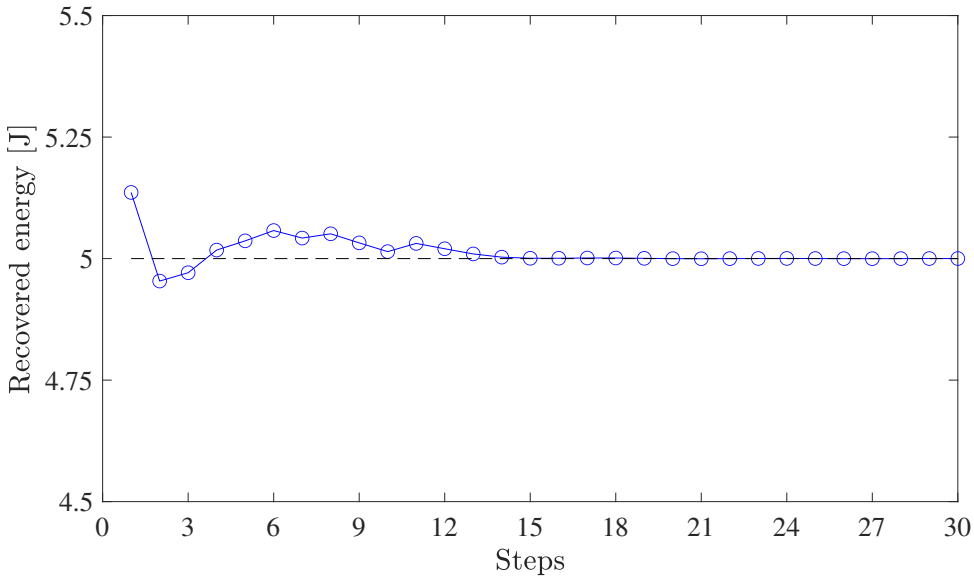

Figure 5.6: Recovered energy over the number of steps

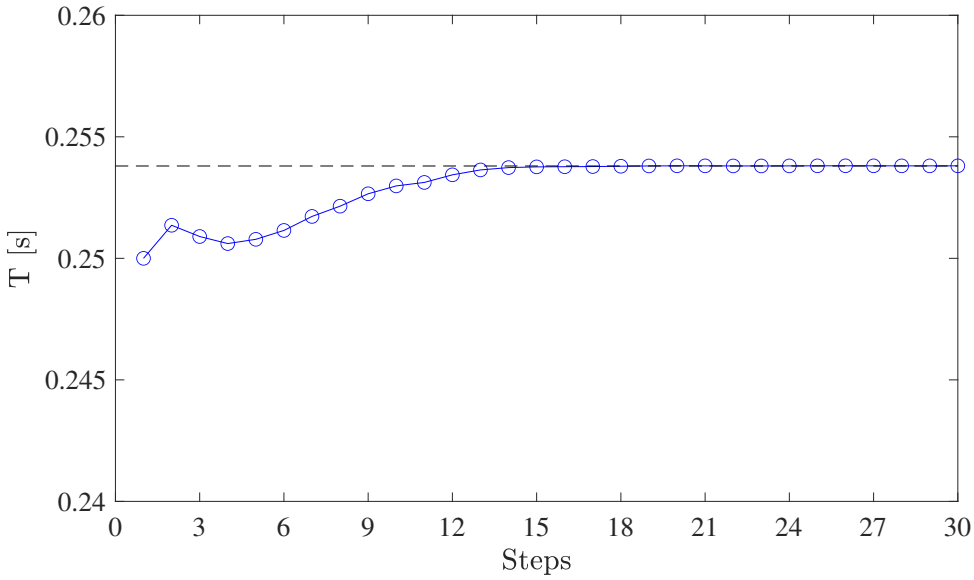

Figure 5.7: Control period over the number of steps

realization of a limit cycle gait, as evidenced by the simulation results. This indicates that for the current shape, maintaining consistent landing postures can contribute to achieving a stable limit cycle gait.

5.3.2 Recovered energy constant control

Given a constant control objective, which is the desired posture, different control periods will result in different amounts of recovered energy. The purpose of this control is to adjust

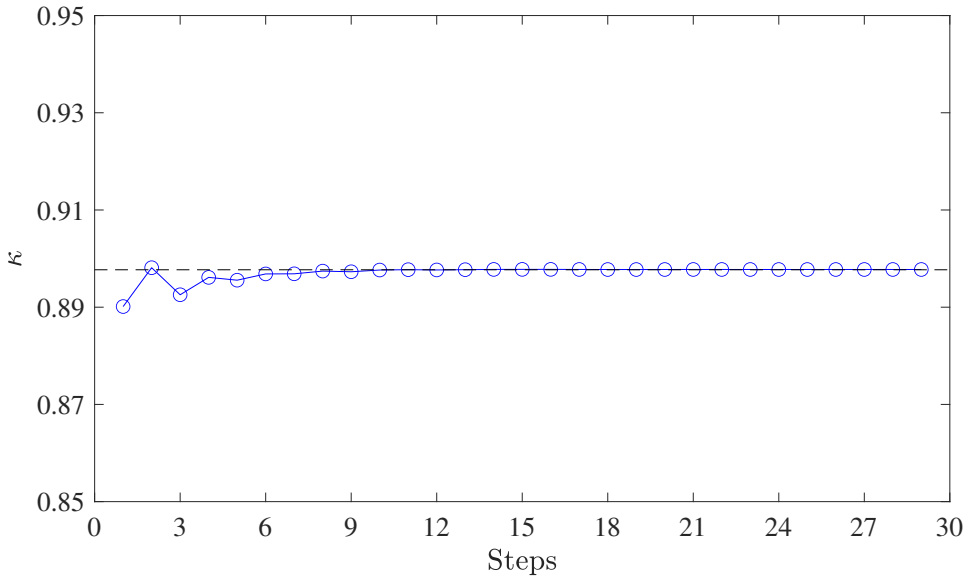

Figure 5.8: Proportion of kinetic energy loss over the number of steps

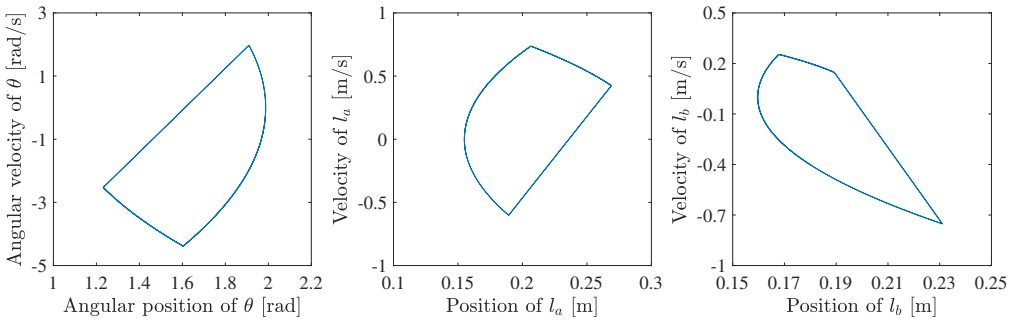

Figure 5.9: Phase diagram with recovered energy constant control

the control period in such a way that the recovered energy for each step remains consistent and matches a predetermined value.

Here, based on the previous control approach, we introduce feedback adjustment of the control period, as described by the following formula:

$$T[j+1] = T[j] + k_p \Delta E[j], \tag{5.23}$$

where k_p is the gain that we set it as 0.01, $\delta E[j]$ is the error between the recovered energy of current step and the target energy input, and the recovered energy is obtained the following formula:

$$\Delta E[j] = \int_0^{T[j]} (|\dot{l}_a u_1| + |\dot{l}_b u_2| + |\dot{\theta} u_3|) \mathrm{d}t. \tag{5.24}$$

Here we set the target input energy is 5 [J], starting the simulation from any initial state, Figure 5.6 represents the input energy for each step. As observed in the figure, the input energy tends

to approach the dashed line, which represents the set value of target input energy 5 [J]. This indicates that the current control objective has been achieved.

Figure 5.7 depicts the adjustment of the control period through feedback, and Figure 5.8 depicts the proportion of kinetic energy loss over the number of step, which are ultimately stabilizes. This results in the achievement of the limit cycle gait shown in Figure 5.9.

This control demonstrates that when the recovery energy for each step is consistent, the achievement of a limit cycle gait can be realized.

5.4 Summary and Discussions

This chapter primarily aims to verify the generation conditions of the limit cycle gait of SRWT. Due to the soft characteristics of tensegrity, namely, the strong nonlinearity resulting from the internal coupling elasticity, its motion is difficult to be directly controlled. The MBC proposed in this study indirectly controls the position by manipulating its morphological characteristics, specifically convergence position and convergence velocity.

The stability of the gait is related to both morphological characteristics and the target position. The previous chapter provided a method for finding the target position and numerically simulated the optimal target position that can achieve the limit cycle. However, the fundamental reasons behind it were not thoroughly explored.

In order to explain the essence of the limit cycle occurrence, this chapter focuses on the kinetic energy variation and proposes two necessary conditions for the limit cycle gait: the kinetic energy loss rate during collisions, determined by the landing posture, and the recovery energy in each step, determined by the motor. To investigate these two necessary conditions, a model composed of rigid structures is proposed in this chapter, enabling precise control. By achieving different control objectives, we discover that both necessary conditions can realize the limit cycle, demonstrating that the determinants of the limit cycle are the consistent landing posture and constant input energy, thus providing guidance for gait trajectory design.

Chapter 6

Experimental Validation

6.1 Overview

Robot experiments play a crucial role in the development and advancement of robots.

Through experiments, researchers can test the performance, accuracy, and safety of robots, as well as identify areas for improvement. Additionally, experiments help researchers validate theoretical concepts and models, which is crucial for designing and developing robots. Therefore, robot experiments are essential for improving their performance, reliability, and safety. This chapter discusses two types of experiments: validation experiments and engineering experiments. Validation experiments aim to test the correctness of theoretical concepts and models through passive gaits. On the other hand, engineering experiments aim to demonstrate that RWT, as a robot platform, can perform dynamic walking.

6.2 Preliminary Experimental Study

As shown in Figure 6.1, we constructed three interlocking frames using aluminum alloy, connected by rubber bands. The three interlocking frames ensure stability in the Y direction, thus ensuring motion in the XOZ plane, as in the planar model of RWT discussed in Chapter 2. The rubber bands act as strings, providing only tensile forces. It is about 25cm tall and weighs less than 1kg. The sequence photographs of experimental passive dynamic walking in one cycle are shown in Figure 6.3, where one can observe that the limbs keep rotating during the DSP phase by comparing the first and second sequence of Figure 6.3.

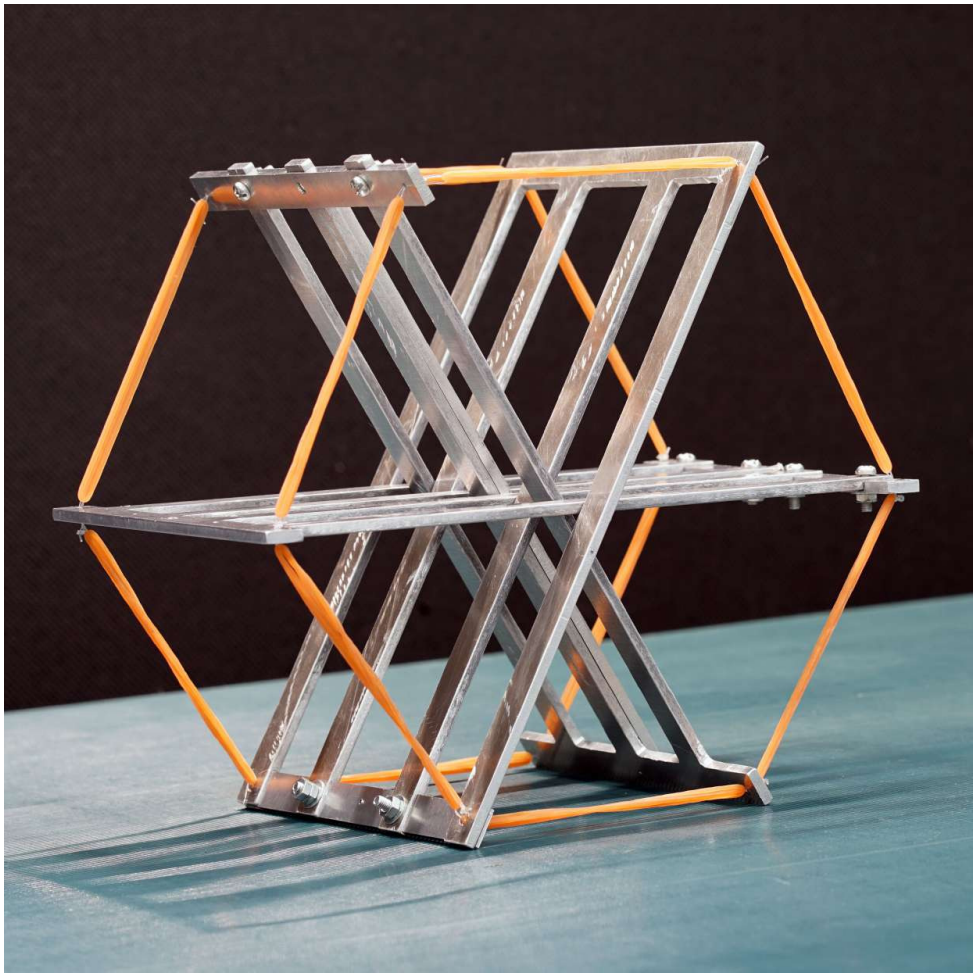

Figure 6.1: Prototype planar RWT.

Our study focuses on investigating the effect of string tension on walking periods using numerical simulations. To achieve this goal, we compare two sets of tension levels while varying the slope angle of the ground, as it is easier to manipulate the slope angle than the tension experimentally. We collect more than 50 sets of data for each state, and the results are presented in Figure 6.2.

From the mean values presented, we observe that a slack string results in a longer walking period compared to the tight string condition. When the robot is in the tightly strung state and walking on a low slope, the data exhibits a large standard deviation, indicating a multi-cycle gait. However, as the slope increases, the energy generated by collisions increases, resulting in a rapid decrease in standard deviation, and eventually reaching a stable value after $\phi = 0.085$, indicating a limit cycle gait. On the other hand, when the string is slack, the standard deviation remains constant, indicating that the robot has reached a limit cycle gait state.

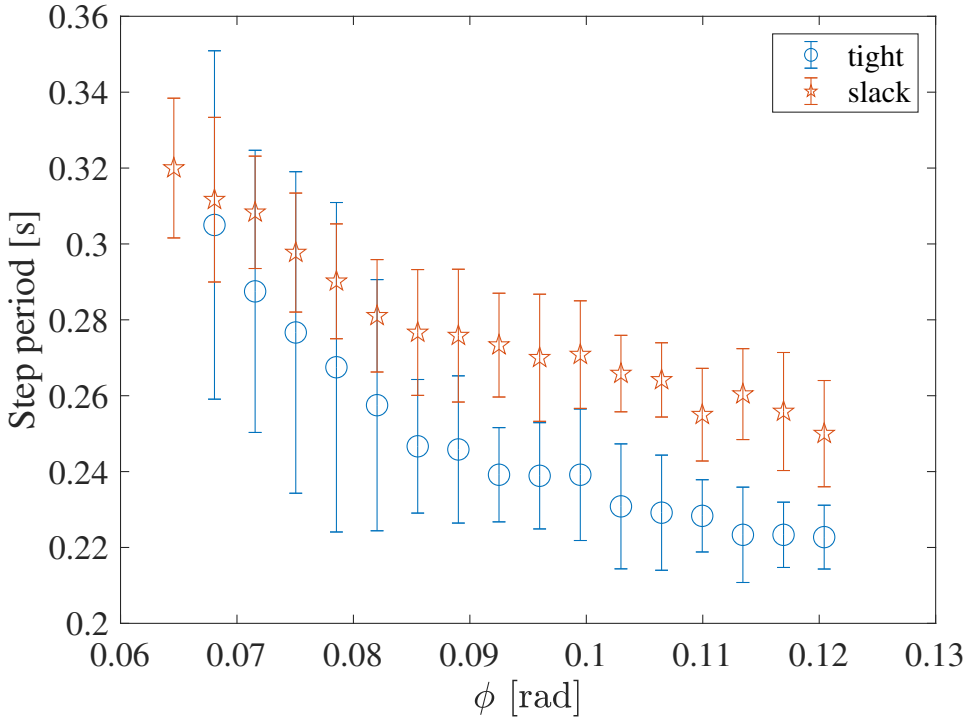

Figure 6.2: Experimental results of crawling morphology

These experimental results demonstrate that the robot exhibits chaos, but the energy generated by collisions can cancel out the chaos. We conclude that as the slope angle increases, the standard variance decreases, suggesting that chaotic gaits are suppressed and converge towards limit cycles. These observations are in agreement with the simulation results, and provide new insights into the effect of string tension on walking gaits.

6.3 Morphological Verification

To validate the mathematical model and the numerical simulation results, we conducted a preliminary experimental study using the prototype machine depicted in Figure 6.4 and Figure 6.5. Although adjusting all structural parameters to search for the optimal design is impractical, we were able to successfully identify crawling and walking morphologies, even when the physical parameters of the experiment differed greatly from those in the theoretical simulation. Interestingly, the crawling and walking morphologies produced 1:1 and 1:2 resonances, respectively, which facilitated implementation. However, the skipping morphology required a 1:4 resonance, making it more challenging to achieve. Overall, our findings confirm the validity of the mathematical model and the accuracy of the numerical simulation results.

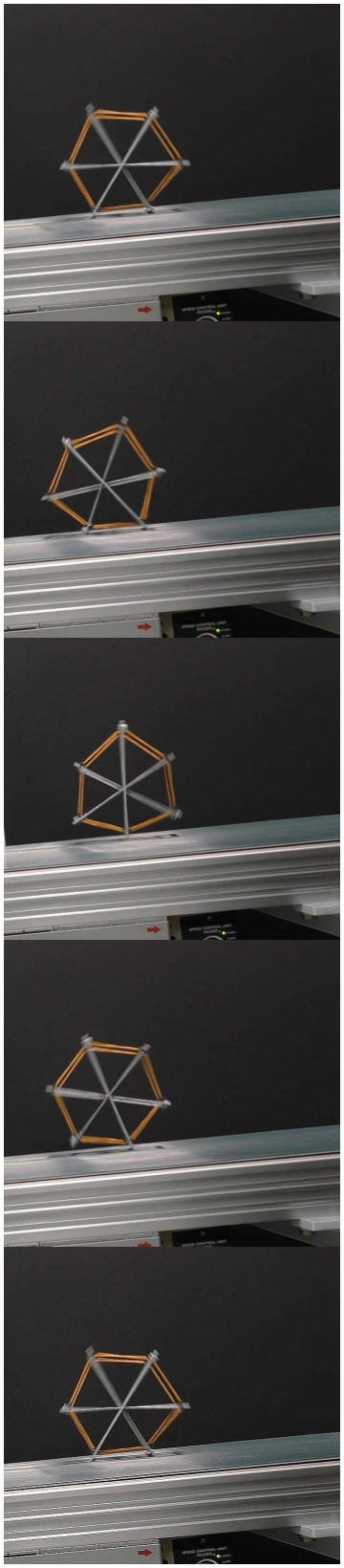

Figure 6.3: Sequence photographs of experimental passive dynamic walking in one cycle

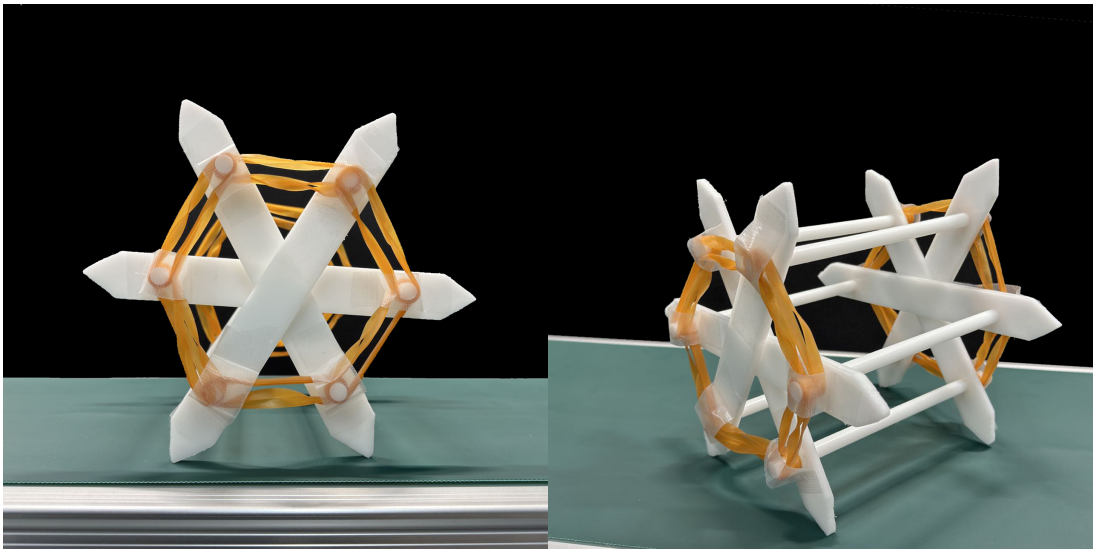

Figure 6.4: Prototype of the morphology that corresponding walking gait

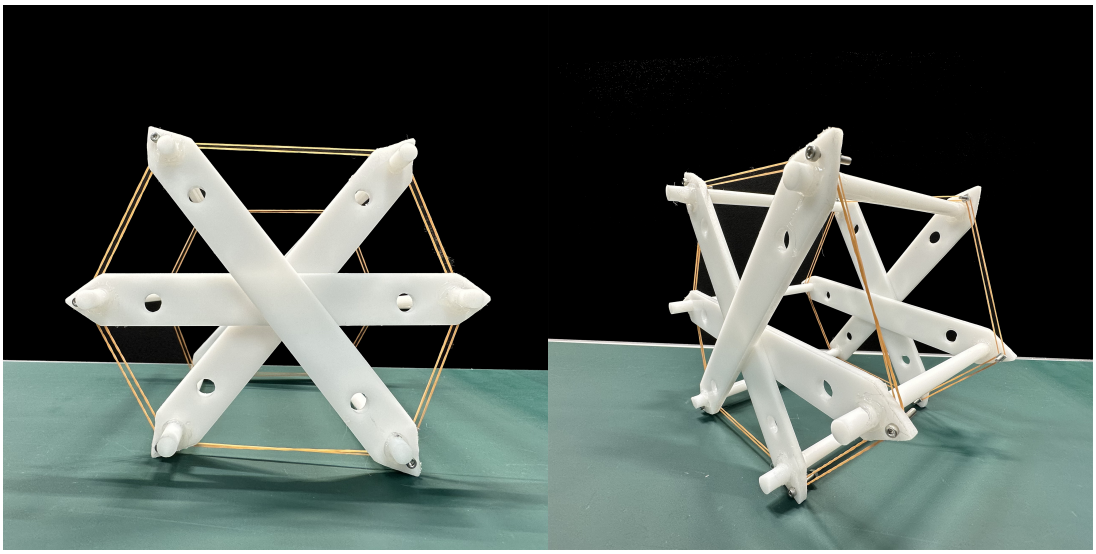

Figure 6.5: Prototype of the morphology that corresponding crawling gait

Morphology corresponding to walking

To construct the leg mechanisms, we employed resin material to create three individual frames each with a length of approximately 0.3 [m]. These frames were then connected using rubber bands. To optimize the design of the connection point, we referred to the trend and ultimately selected a connection point located one-quarter of the length of each leg. The elasticity coefficient of each set of rubber bands was carefully measured and found to be approximately 585 [N/m].

The landing time of each step was determined by analyzing the sound of walking, and the

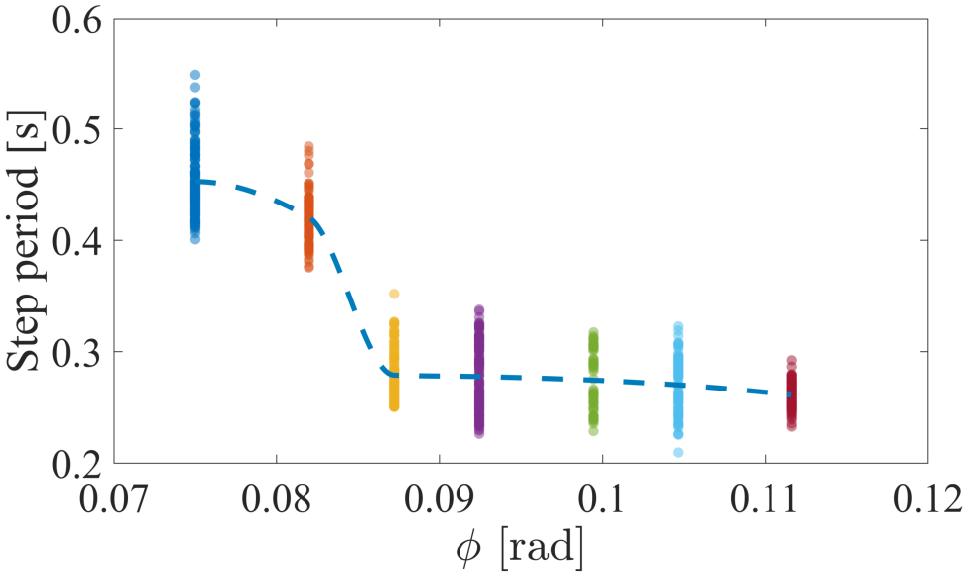

Figure 6.6: Experimental results of walking gaits

results are presented in Figure 6.6. The figure shows that the walking morphology exhibits a limit-cycle gait, as there is minimal variation in the landing time of each step. Interestingly, there is a noticeable jump in the landing time around $\phi = 0.85$ [rad], which was detected through fitting local averages using a Cubic Hermite spline. This phenomenon is consistent with the observations in numerical simulation results, thus further confirming the accuracy of the simulation.

Morphology corresponding to crawling

The trends observed in the previous experiments led us to conduct further experiments with reduced elasticity coefficient and placing the connection points at the end points of the legs. The results are presented in Figure 6.7.

When the slope angle exceeds 0.3 [rad], we observed a bifurcation phenomenon where the robot transitions from walking to a TSP, which is the crawling morphology. This phenomenon is also observed in the simulation results, confirming the accuracy of the simulation. However, in this crawling morphology, the gait does not exhibit a limit-cycle, as there is a large range of variation in the walking period. This result is consistent with the simulation, which predicted that the robot cannot maintain a limit cycle gait beyond a certain slope angle.

Through these experiments, we were able to demonstrate the validity of the numerical simulation results, as we observed the same tendency even with different physical parameters. This

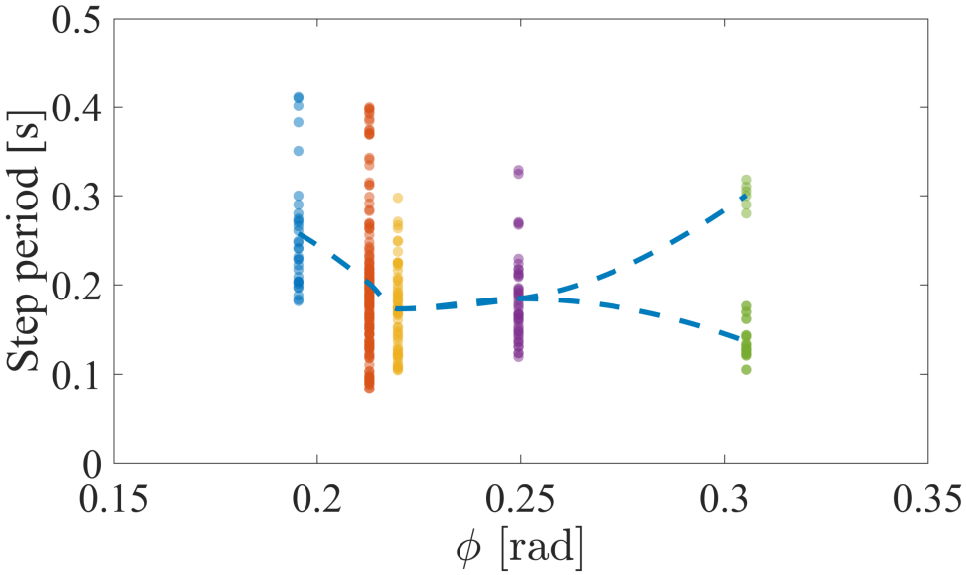

Figure 6.7: Experimental results of crawling gait generation

suggests that our mathematical model is robust and can accurately predict the behavior of the robot under different conditions.

We have previously presented the experimental results of robot walking, and now we showcase the experimental results of robot crawling, as shown in Figure 6.8. The experimental results indicate that, under the current robot morphology, the crawling of the robot consists of two configurations: DSP and TSP.

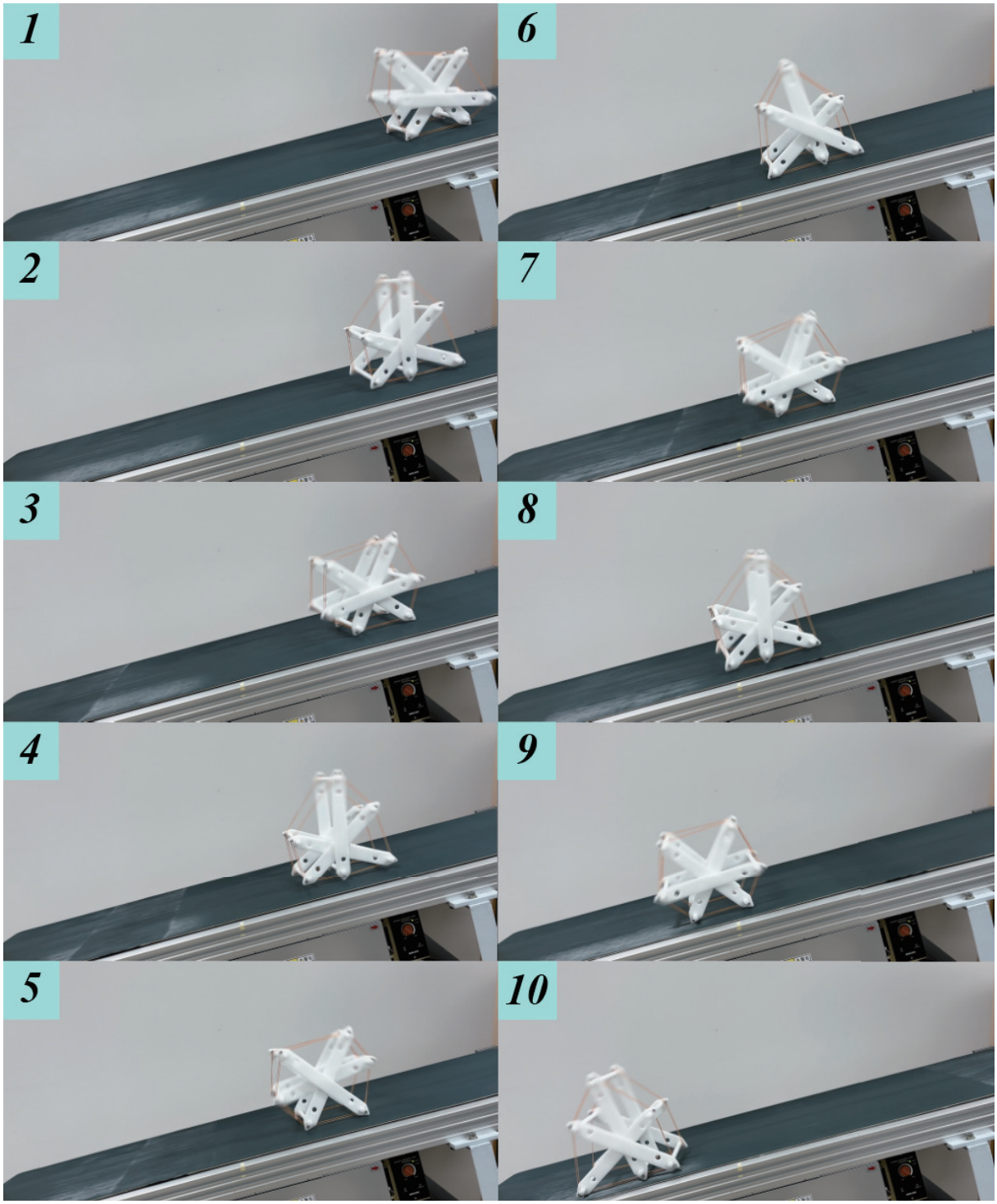

Figure 6.8: Sequence photographs of experimental passive dynamic walking of crawling Morphology

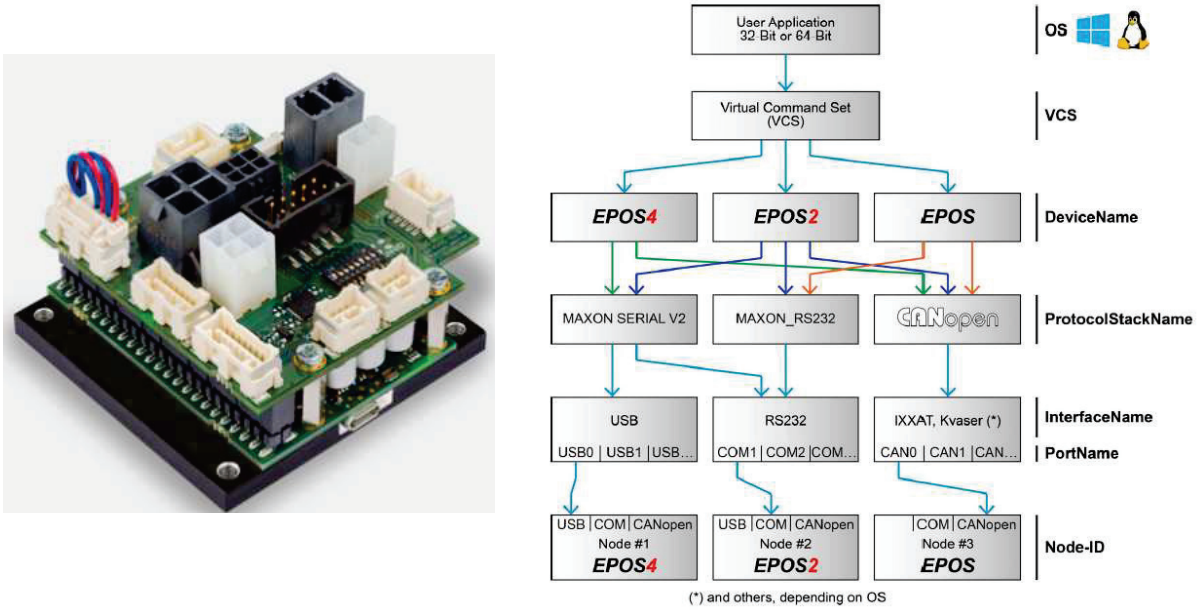

Figure 6.9: Motion controller and its communication structure

6.4 Walking Realization of SRWT

This section validates the engineering application of the robot through experiments, achieving large strides in walking by means of electric motors.

The robot body is made of steel and aluminum to ensure maximum light weight while maintaining rigidity. It has a height of 0.5 [m] and weighs approximately 2.635 [kg]. To simulate the structure in the mathematical model, two frames are used to eliminate the effect of the Y-direction. The frames are connected by two linear bearings that allow for rotation against each other, ensuring free movement of the frames in the XOZ plane. The winder is attached to the motor and has a radius of 0.02 [m], which is used to control the length of the strings. Springs shown in Figure 6.11 are employed to increase the internal elasticity and achieve the elastic properties of the strings. This construction allows for guaranteed intrinsic compliance.

6.4.1 Motor drive

This experiment used Maxon motors, which are high-performance brushless DC motors with characteristics such as high efficiency, high precision, and high reliability, making them suitable for various fields such as robotics, medical equipment, industrial automation, and

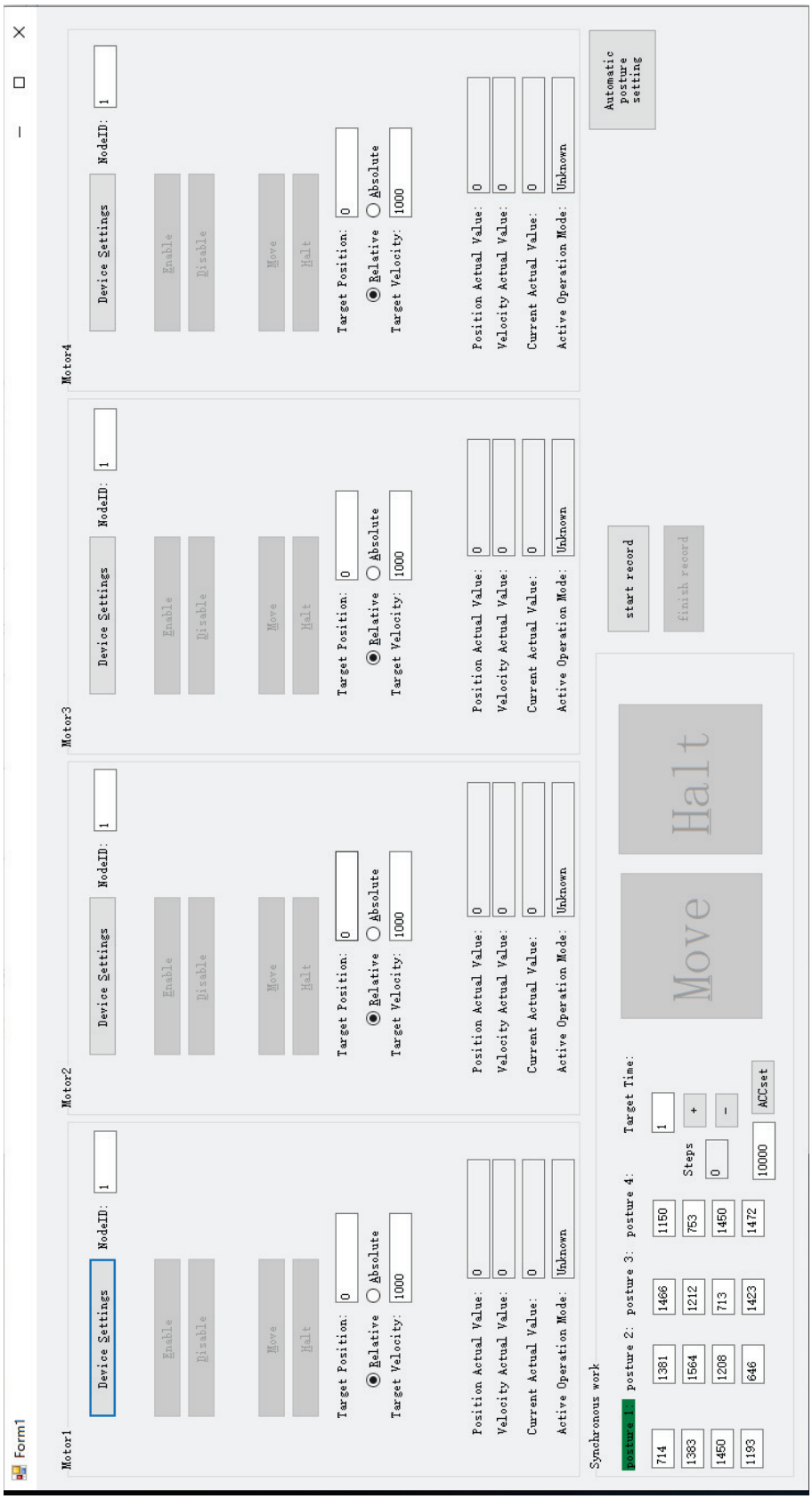

Figure 6.10: Program interface

aerospace.

The Epos4 that we used in the experiment as shown in Figure 6.9 is a high-performance motion controller developed by Maxon Motor that can be used to control Maxon motors. It uses the CANopen communication protocol and supports various control modes, such as speed mode, position mode, current mode, etc., enabling high-precision motion control. Additionally, the Epos4 has various features and communication interfaces, such as digital input/output, analog input/output, USB interface, Ethernet interface, etc., which can meet the requirements of different application scenarios. The communication in this experiment is based on its USB interface.

We have developed a graphical user interface (GUI) program using C# as shown in Figure 6.10 to communicate with the EPOS4 motion controller. The GUI provides a user-friendly way to send commands to the controller and receive data from it.

The communication between the GUI and the EPOS4 is based on the CANopen communication protocol, which is widely used in the field of motion control. In our implementation, we use the PCAN-USB adapter to connect the computer and the EPOS4, and we use the PCAN-Basic library to handle the communication.

The communication process starts by initializing the CAN bus and setting up the connection between the PCAN-USB adapter and the EPOS4. The EPOS4 is configured to use the CANopen protocol and assigned with a unique node ID. The GUI sends commands to the EPOS4 by constructing CAN messages and sending them over the CAN bus. The messages contain the necessary information for the EPOS4 to perform the desired action, such as setting the motor velocity or position.

The EPOS4 responds to the commands by sending back CAN messages with the requested data. The GUI receives these messages and extracts the data, which is then displayed on the GUI. The GUI also provides real-time feedback of the motor status, such as its position and velocity.

To ensure reliable communication, error handling mechanisms are implemented in the GUI program. The program checks for errors such as communication timeouts or incorrect responses from the EPOS4, and displays error messages to the user.

6.4.2 Control Realization

Morphology-based control (MBC) is applicable to higher-order or difficult-to-linearize systems that are often challenging to control directly. However, for such systems, direct control is not feasible. Nevertheless, the convergence characteristics of the system, such as convergence speed or target convergence state, can be altered by controlling the inputs. Despite its indirect nature, this type of control offers a viable approach.

In the case of SRWT, its motion equations are more complex and nonlinear compared to traditional second-order equations due to the high coupling of internal elastic elements. Employing conventional control methods would lead to significant variations in the structure of this highly sensitive nonlinear system, even if control were achieved, due to any slight disturbance during the experimental process. Although optimization can enhance control stability, it does not bring about substantial changes to such systems. However, with the use of MBC, the control objective shifts from controlling the position to controlling the convergence characteristics of the system. This enables the elimination of any disturbance through the system's inherent convergence property. Although indirect, this method ensures the achievement of the target state and controls the convergence speed, i.e., the motion speed, indirectly.

During simulation, we have already established the method for setting the target posture. In the experiment, we utilize the simulation results to control the lengths of the four strings, thereby generating different elastic forces and achieving variations in morphological characteristics. This leads to different convergence states or target states, allowing for control.

At the beginning of the control process, the four strings quickly reach their designated positions in minimal time, facilitated by the motor's position control. This involves real-time feedback of the motor's position through a Hall sensor, creating a closed-loop negative feedback control system. After reaching the target position, imbalanced tension within the system arises due to the presence of elastic elements. This tension is caused by the elastic elements, disrupting the current equilibrium state and moving towards the target state. This change alters the morphological characteristics of the system, namely, the convergence state. Based on its inherent convergence speed, SRWT gradually achieves changes in its attitude, leading to movement.

Based on previous theories, such attitude changes result in a forward moment, which, in turn, can generate a limit cycle gait when accompanied by consistent restoring energy or con-

sistent landing posture. Therefore, the experimental results have also demonstrated the achievement of stable limit cycle gaits, as detailed in the following section.

6.4.3 Experimental results

Drawing from the theory outlined above, we selected appropriate arbitrary parameters, to generate the target landing posture for every step. We adopted position control mode and set the parameter T_{set} to 0.4 [s]. However, due to the motor's acceleration limitation, the actual time required to complete the trajectory will exceed the set 0.4 [s]. The objective of the control is to generate a forward moment, and thus, a tracking error is permissible for the robot.

As the presented motion is periodic, consisting of four steps to complete one cycle, the presented data consist of four-step sequences. Figure 6.12 presents an image sequence of the walking gait, showing four steps arranged in a circle. Correspondingly, Figure 6.13 and Figure 6.14 demonstrate the associated data form the winder during the gait. To ensure data accuracy, a sampling interval of 0.03 [s] is used for data collection. However, due to communication delay, we could not guarantee precise adherence to this sampling interval, resulting in an error of several millimeters.

Figure 6.13 clearly shows that the motor does not achieve zero velocity during the transition between four steps. This observation indicates that the motor has not yet reached its intended target position upon landing and is in the process of adjusting its posture. This dynamic behavior can produce a positive response to collisions during landing and generate forward torque. Nevertheless, to ensure experimental rigor, the motor can be operated in reverse to facilitate string release and match the contraction of the other strings. By doing so, all motors can work simultaneously, as depicted in Figure 6.13 (c), which displays their combined output torque of approximately 0.3 [Nm].

Figure 6.14 displays the phase diagram for the physical experiment involving all four motors. Due to mechanical constraints, the string lengths associated with each motor cannot be perfectly identical. As a result, the phase diagram is horizontally shifted, with only the positions varying. Nevertheless, the phase diagram clearly depicts a limit cycle with a period-1 gait.

The physical parameters of the experimental setup differ from those used in the simulation. In particular, the physical experiment cannot ensure an exact initial state of motion. However,

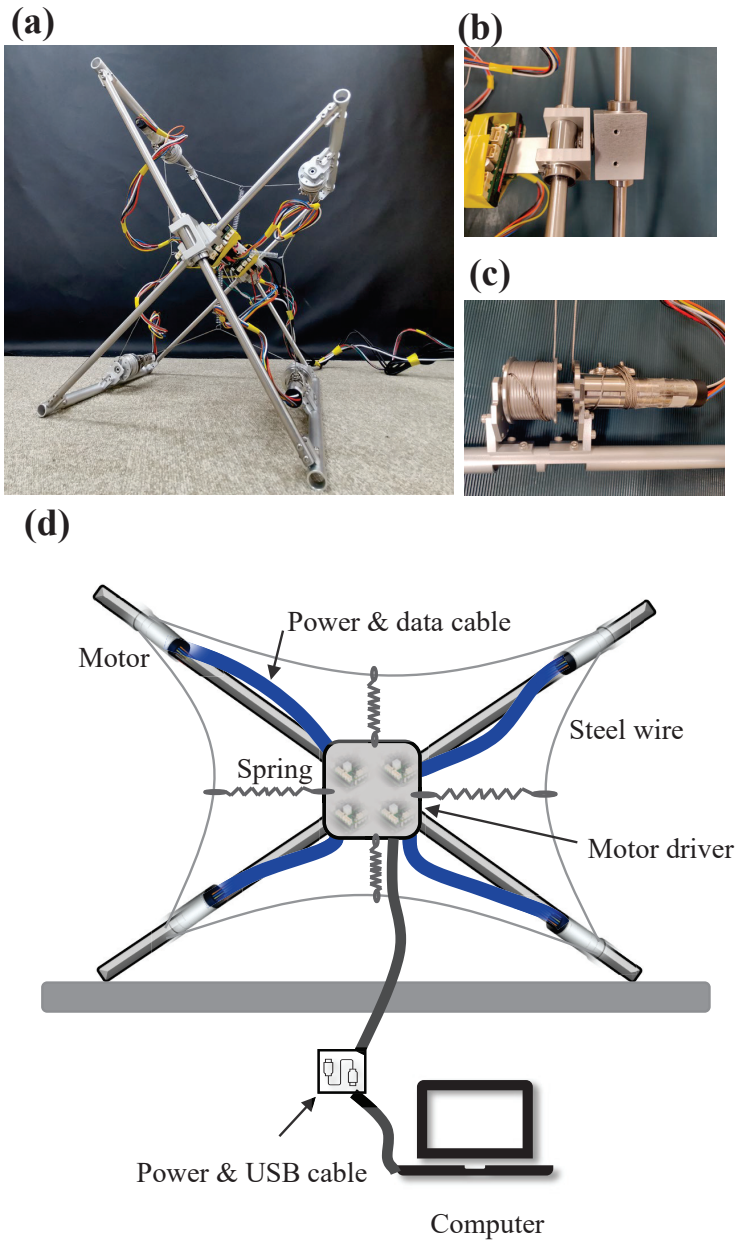

Figure 6.11: Experimental prototype. (a) is the physical prototype, which consists of two frames. (b) is two linear bearings that can rotate with each other connect the two frames, ensuring that the two frames move freely in the XOZ plane, while the frame structure ensures the limitation in the Y direction. (c) is a kit that includes a motor reducer and a Hall sensor. (d) is the structure diagram, four motors are installed in the top of the frame, and the motor drive which is installed in the middle, connected to the computer via USB. The computer acts as a controller to send commands to the drivers and receive data.

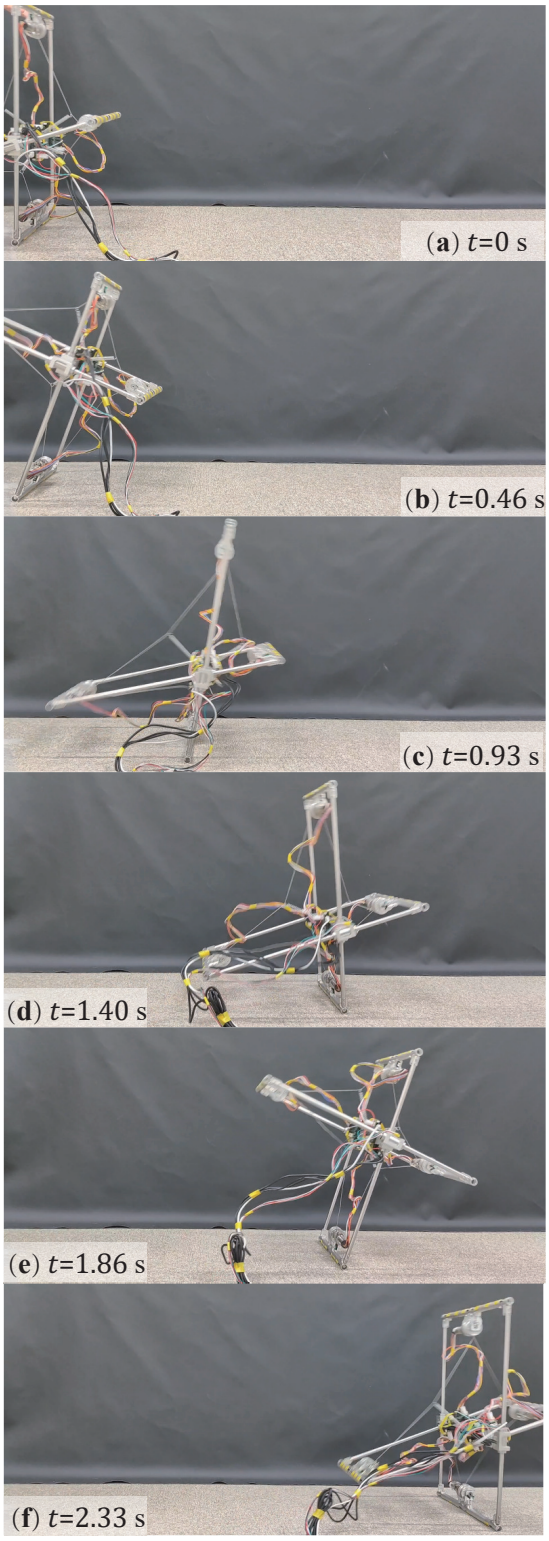

Figure 6.12: Image sequence of a walking gait with four steps in a circle

the system's intrinsic compliance allows it to exhibit the desired gait in both cases. This not only demonstrates the achievability of stable walking through this property, but also highlights its independence from high-precision control.

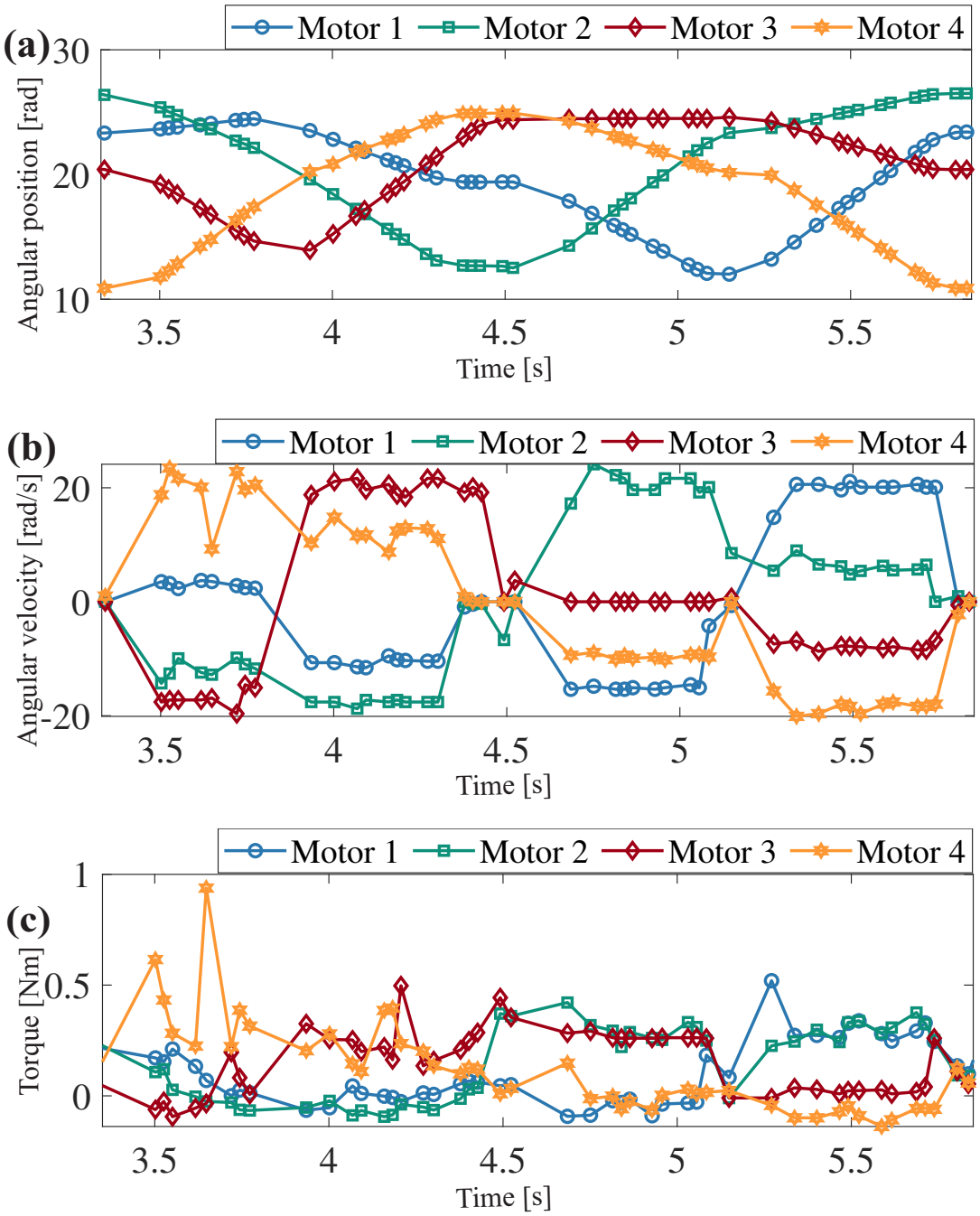

Figure 6.13: Physical experiment results. (a) shows its the time evolution of the angular position of the winder. (b) is the time evolution of the angular speed of the winder. (c) is the motor output torque.

6.5 Summary and Discussions

This chapter presents two sets of physical experiments based on the previous chapters. The first set is a verification experiment that validates the morphology characteristics of RWT and

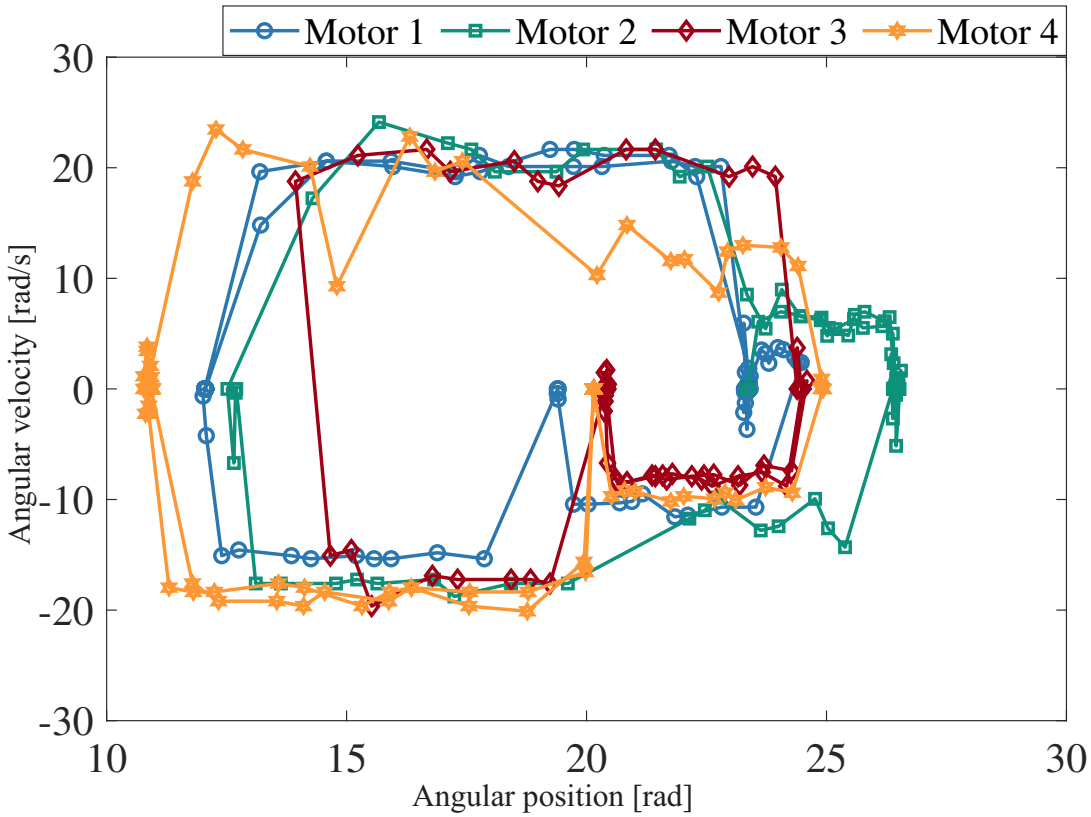

Figure 6.14: Phase diagram of physical experiment

discovers the regularity of its motion characteristics, consistent with the simulation, thus proving the effectiveness of the mathematical model and simulation. On the other hand, an engineering experiment is conducted to achieve the planar walking of SRWT through MBC method. The data shows that stable limit cycle gaits can be generated, consistent with the simulation results, demonstrating the effectiveness and stability of the control, as well as the practical engineering significance of the minimal model proposed in this study.

Chapter 7

Conclusion and Future Works

7.1 Summary

In recent years, considering the morphology of robots has become a criterion for robot design. However, there is currently no systematic framework to guide specific robot tasks. Based on this, in this study, a feasible method for robot morphology is provided by selecting tensegrity robots as the carrier.

The first step based on the tensegrity robot includes the following:

- A minimal model RWT is proposed to solve the problem of difficult dynamic modeling of tensegrity robots.
- In dynamic modeling, the coupling of internal elastic forces and environmental constraint forces during MSP is emphasized, and modeling methods are provided for each case.
- Improved models such as curved feet and frictional surfaces are discussed to expand the model's applicability.

The second step is to verify the correctness of the modeling and explore the characteristics of RWT:

- A simulator is designed using MATLAB to demonstrate the existence of forward collision phenomena during motion that are difficult to observe objectively. Periodic passive walking is ultimately achieved.
- Period-1, period-2 or chaotic gaits are observed, demonstrating that RWT has multiple convergence properties and provides a basis for morphology research.

- The conditions and most suitable movement modes for different morphologies, such as crawling, walking, and skipping, are further analyzed.

The third step proposes MBC, which changes the posture and characteristics of the original model by controlling the input, i.e., changes in posture by characteristics of the morphology.

- The control concept and implementation process of MBC are introduced using the simplest model of a spring cart system.
- MBC is used on passive gaits to achieve changes in morphology, i.e., crawling-walking.
- MBC can be used not only for single morphology/posture changes but also for continuous morphology/posture changes. Thus, this study further simplifies RWT and proposes the SRWT model.
- By simulating the convergence of morphology, SRWT posture changes are achieved, thus realizing walking on flat ground.
- Based on walking on flat ground, typical gaits are discussed, and its stability is analyzed.
- The applications of SRWT are given, such as walking on uneven ground and its suitability for low-gravity environments.

The fourth step is experimental verification:

- The Simple experiments verify the relevant conclusions of RWT under passive gaits, demonstrating the significance of the minimum model of robot morphology research.
- Based on MBC, SRWT's walking on flat ground is achieved, demonstrating the effectiveness of the control and dynamic characteristics of the model.

7.2 Contribution and Conclusion

This study proposes a novel minimal model, RWT, based on tensegrity structures that unifies the characteristics of both rigid and soft robots. Due to its unique features, RWT can serve as the minimal model for robot morphology design and offer theoretical insights in academia. Through passive gait, this study demonstrates that RWT possesses various characteristics and

can take on different forms. RWT can serve as a fundamental platform for robot morphology design.

Moreover, this study is based on the RWT dynamics model and proposes a modeling method that overcomes the difficulties in tensegrity robot dynamics modeling. Due to this difficulty, tensegrity robots have not been widely utilized in engineering applications despite their unique features. However, with this modeling method, model-based control can be achieved, greatly improving the practicality of this type of robot.

This study proposes a new control method based on morphology control, which aims to change the system characteristics by controlling the input. Compared to traditional control methods, which directly change the posture of rigid robots, this method relies on the convergence properties of the system to change posture. Such control reduces control complexity and improves the adaptability of the robot by relying more on its own structural characteristics for motion implementation.

7.3 Future Works

Regarding the current work of this study, there are still some tasks that need to be completed. First, although the proposed RWT model has shown great potential in robot morphology study and motion control, there is still room for improvement. One possible direction is to investigate how to optimize the design parameters of the RWT model for specific tasks. For example, how can we adjust the tension and compression elements to achieve better stability and mobility for different types of terrains or environments?

Second, although the proposed control strategy based on morphology control has shown advantages over traditional posture control for RWT, its performance can be further improved. One possible direction is to explore the integration of reinforcement learning or other machine learning techniques to enhance the adaptive capability of the RWT model.

Thirdly, while the proposed modeling method has filled the gap in the dynamic modeling of tensegrity robots, it is still limited to simple tensegrity structures. Therefore, another possible direction is to extend the proposed modeling method to more general tensegrity structures and investigate how to apply the method to other types of tensegrity robots.

Finally, conducting experimental validation of the proposed RWT model and control strategy in real-world scenarios will also be of significant value. This study only proposed walking

experiments, and in future work, experiments for movement in various forms will also need to be completed.

Bibliography

[1] J. Reher, W.-L. Ma, and A. D. Ames, "Dynamic walking with compliance on a cassie bipedal robot," *2019 18th European Control Conference (ECC)*, pp. 2589–2595, 2019.

[2] A. Bouman, M. F. Ginting, N. Alatur, M. Palieri, D. D. Fan, T. Touma, T. Pailevanian, S.-K. Kim, K. Otsu, J. Burdick, and A.-a. Agha-Mohammadi, "Autonomous spot: Long-range autonomous exploration of extreme environments with legged locomotion," *2020 IEEE/RSJ International Conference on Intelligent Robots and Systems (IROS)*, pp. 2518–2525, 2020.

[3] F. Enner, D. Rollinson, and H. Choset, "Motion estimation of snake robots in straight pipes," *2013 IEEE International Conference on Robotics and Automation*, pp. 5168–5173, 2013.

[4] S. Kuindersma, R. Deits, M. Fallon, A. Valenzuela, H. Dai, F. Permenter, T. Koolen, P. Marion, and R. Tedrake, "Optimization-based locomotion planning, estimation, and control design for the atlas humanoid robot," *Autonomous robots*, vol. 40, pp. 429–455, 2016.

[5] J. Yue, "Biomimetic wheeled-foot robot based on the motion mechanism of moroccan spider," *2022 IEEE 5th International Conference on Information Systems and Computer Aided Education (ICISCAE)*, pp. 623–627, 2022.

[6] V. G. Jáuregui, *Tensegrity structures and their application to architecture*, vol. 2. Ed. Universidad de Cantabria, 2020.

[7] D. S. Shah, J. W. Booth, R. L. Baines, K. Wang, M. Vespignani, K. Bekris, and R. Kramer-Bottiglio, "Tensegrity robotics," *Soft robotics*, vol. 9, no. 4, pp. 639–656, 2022.

[8] J. Friesen, A. Pogue, T. Bewley, M. de Oliveira, R. Skelton, and V. Sunspiral, "Ductt: A tensegrity robot for exploring duct systems," *2014 IEEE International Conference on Robotics and Automation (ICRA)*, pp. 4222–4228, 2014.

[9] T. Rhodes, C. Gotberg, and V. Vikas, "Compact shape morphing tensegrity robots capable of locomotion," *Frontiers in Robotics and AI*, vol. 6, 2019.

[10] A. P. Sabelhaus, J. Bruce, K. Caluwaerts, P. Manovi, R. F. Firoozi, S. Dobi, A. M. Agogino, and V. SunSpiral, "System design and locomotion of superball, an untethered tensegrity robot," *2015 IEEE international conference on robotics and automation (ICRA)*, pp. 2867–2873, 2015.

[11] R. Siegwart, I. Nourbakhsh, and D. Scaramuzza, *Introduction to Autonomous Mobile Robots, second edition*. Intelligent Robotics and Autonomous Agents series, MIT Press, 2011.

[12] F. Rubio, F. Valero, and C. Llopis-Albert, "A review of mobile robots: Concepts, methods, theoretical framework, and applications," *International Journal of Advanced Robotic Systems*, vol. 16, no. 2, p. 1729881419839596, 2019.

[13] J. Borenstein, H. R. Everett, L. Feng, and D. Wehe, "Mobile robot positioning: Sensors and techniques," *Journal of Robotic Systems*, vol. 14, no. 4, pp. 231–249, 1997.

[14] F. R. Noreils, "Toward a robot architecture integrating cooperation between mobile robots: Application to indoor environment," *The International Journal of Robotics Research*, vol. 12, no. 1, pp. 79–98, 1993.

[15] M. Cardona, F. Cortez, A. Palacios, and K. Cerros, "Mobile robots application against covid-19 pandemic," in *2020 IEEE ANDESCON*, pp. 1–5, 2020.

[16] O. Miglino, H. H. Lund, and S. Nolfi, "Evolving Mobile Robots in Simulated and Real Environments," *Artificial Life*, vol. 2, pp. 417–434, 07 1995.

[17] G. Dudek and M. Jenkin, *Computational principles of mobile robotics*. Cambridge university press, 2010.

[18] E. Krotkov and J. Blitch, "The defense advanced research projects agency (darpa) tactical mobile robotics program," *The International Journal of Robotics Research*, vol. 18, no. 7, pp. 769–776, 1999.

[19] M. Montemerlo, J. Pineau, N. Roy, S. Thrun, and V. Verma, "Experiences with a mobile robotic guide for the elderly," *AAAI/IAAI*, vol. 2002, pp. 587–592, 2002.

[20] D. Klenert, E. Fernández-Macías, and J.-I. Antón, "Do robots really destroy jobs? evidence from europe," *Economic and Industrial Democracy*, vol. 44, no. 1, pp. 280–316, 2023.

[21] T. B. Sheridan, "Human–robot interaction: Status and challenges," *Human Factors*, vol. 58, no. 4, pp. 525–532, 2016. PMID: 27098262.

[22] T. Haidegger, J. Sándor, and Z. Benyó, "Surgery in space: the future of robotic telesurgery," *Surgical endoscopy*, vol. 25, pp. 681–690, 2011.

[23] T. Williams, G. Briggs, B. Oosterveld, and M. Scheutz, "Going beyond literal command-based instructions: Extending robotic natural language interaction capabilities," *Proceedings of the AAAI Conference on Artificial Intelligence*, vol. 29, no. 1, 2015.

[24] D. Gweon and H. Kim, "Development of a mobile robot controlled by three motors for a hostile environment," *Mechatronics*, vol. 2, no. 1, pp. 43–63, 1992.

[25] L. E. Parker, D. Rus, and G. S. Sukhatme, "Multiple mobile robot systems," *Springer Handbook of Robotics*, pp. 1335–1384, 2016.

[26] M. B. Alatise and G. P. Hancke, "A review on challenges of autonomous mobile robot and sensor fusion methods," *IEEE Access*, vol. 8, pp. 39830–39846, 2020.

[27] F. Rubio, F. Valero, and C. Llopis-Albert, "A review of mobile robots: Concepts, methods, theoretical framework, and applications," *International Journal of Advanced Robotic Systems*, vol. 16, no. 2, p. 1729881419839596, 2019.

[28] J. Liu, M. Tan, and X. Zhao, "Legged robots — an overview," *Transactions of the Institute of Measurement and Control*, vol. 29, no. 2, pp. 185–202, 2007.

[29] T. Ho, S. Choi, and S. Lee, "Development of a biomimetic quadruped robot," *Journal of Bionic Engineering*, vol. 4, no. 4, pp. 193–199, 2007.

[30] M. Hutter, C. Gehring, A. Lauber, F. Gunther, C. D. Bellicoso, V. Tsounis, P. Fankhauser, R. Diethelm, S. Bachmann, M. Bloesch, H. Kolvenbach, M. Bjelonic, L. Isler, and K. Meyer, "Anymal - toward legged robots for harsh environments," *Advanced Robotics*, vol. 31, no. 17, pp. 918–931, 2017.

[31] C. D. Bellicoso, M. Bjelonic, L. Wellhausen, K. Holtmann, F. Günther, M. Tranzatto, P. Fankhauser, and M. Hutter, "Advances in real-world applications for legged robots," *Journal of Field Robotics*, vol. 35, no. 8, pp. 1311–1326, 2018.

[32] H. Zhuang, H. Gao, Z. Deng, L. Ding, and Z. Liu, "A review of heavy-duty legged robots," *Science China Technological Sciences*, vol. 57, pp. 298–314, 2014.

[33] D. J. Todd, *Walking machines: an introduction to legged robots*. Springer Science & Business Media, 2013.

[34] B. He, S. Wang, and Y. Liu, "Underactuated robotics: a review," *International Journal of Advanced Robotic Systems*, vol. 16, no. 4, p. 1729881419862164, 2019.

[35] G. Surbhi and K. Amod, "A brief review of dynamics and control of underactuated biped robots," *Advanced Robotics*, vol. 31, no. 12, pp. 607–623, 2017.

[36] C. Grand, F. BenAmar, F. Plumet, and P. Bidaud, "Decoupled control of posture and trajectory of the hybrid wheel-legged robot hylos," in *IEEE International Conference on Robotics and Automation, 2004. Proceedings. ICRA '04. 2004*, vol. 5, pp. 5111–5116, 2004.

[37] K. Yin, K. Loken, and M. van de Panne, "Simbicon: Simple biped locomotion control," *ACM Trans. Graph.*, vol. 26, p. 105–es, jul 2007.

[38] M. W. Spong, "Underactuated mechanical systems," in *Control Problems in Robotics and Automation* (B. Siciliano and K. P. Valavanis, eds.), (Berlin, Heidelberg), pp. 135–150, Springer Berlin Heidelberg, 1998.

[39] J. K. Holm and M. W. Spong, "Kinetic energy shaping for gait regulation of underactuated bipeds," in *2008 IEEE International Conference on Control Applications*, pp. 1232–1238, 2008.

[40] S. Rezazadeh and J. W. Hurst, "Toward step-by-step synthesis of stable gaits for underactuated compliant legged robots," in *2015 IEEE International Conference on Robotics and Automation (ICRA)*, pp. 4532–4538, 2015.

[41] C. Paul and J. Bongard, "The road less travelled: morphology in the optimization of biped robot locomotion," in *Proceedings 2001 IEEE/RSJ International Conference on Intelligent Robots and Systems. Expanding the Societal Role of Robotics in the the Next Millennium (Cat. No.01CH37180)*, vol. 1, pp. 226–232 vol.1, 2001.

[42] H. Lund, J. Hallam, and W.-P. Lee, "Evolving robot morphology," in *Proceedings of 1997 IEEE International Conference on Evolutionary Computation (ICEC '97)*, pp. 197–202, 1997.

[43] F. Iida and S. G. Nurzaman, "Adaptation of sensor morphology: an integrative view of perception from biologically inspired robotics perspective," *Interface Focus*, vol. 6, no. 4, p. 20160016, 2016.

[44] S. Mintchev and D. Floreano, "Adaptive morphology: A design principle for multimodal and multifunctional robots," *IEEE Robotics & Automation Magazine*, vol. 23, no. 3, pp. 42–54, 2016.

[45] F. W. Grasso, T. R. Consi, D. C. Mountain, and J. Atema, "Biomimetic robot lobster performs chemo-orientation in turbulence using a pair of spatially separated sensors: Progress and challenges," *Robotics and Autonomous Systems*, vol. 30, no. 1, pp. 115–131, 2000.

[46] W.-S. Chu, K.-T. Lee, S.-H. Song, M.-W. Han, J.-Y. Lee, H.-S. Kim, M.-S. Kim, Y.-J. Park, K.-J. Cho, and S.-H. Ahn, "Review of biomimetic underwater robots using smart actuators," *International journal of precision engineering and manufacturing*, vol. 13, pp. 1281–1292, 2012.

[47] F. W. Grasso, T. R. Consi, D. C. Mountain, and J. Atema, "Biomimetic robot lobster performs chemo-orientation in turbulence using a pair of spatially separated sensors: Progress and challenges," *Robotics and Autonomous Systems*, vol. 30, no. 1, pp. 115–131, 2000.

[48] J. Yu, L. Wang, and M. Tan, "A framework for biomimetic robot fish's design and its realization," in *Proceedings of the 2005, American Control Conference, 2005.*, pp. 1593–1598 vol. 3, 2005.

[49] H. Witte, H. Hoffmann, R. Hackert, C. Schilling, M. S. Fischer, and H. Preuschoft, "Biomimetic robotics should be based on functional morphology," *Journal of Anatomy*, vol. 204, no. 5, pp. 331–342, 2004.

[50] C. Laschi and M. Cianchetti, "Soft robotics: New perspectives for robot bodyware and control," *Frontiers in Bioengineering and Biotechnology*, vol. 2, 2014.

[51] M. J. Pearson, B. Mitchinson, J. C. Sullivan, A. G. Pipe, and T. J. Prescott, "Biomimetic vibrissal sensing for robots," *Philosophical Transactions of the Royal Society B: Biological Sciences*, vol. 366, no. 1581, pp. 3085–3096, 2011.

[52] M. Foote, "The evolution of morphological diversity," *Annual Review of Ecology and Systematics*, vol. 28, no. 1, pp. 129–152, 1997.

[53] R. SATTLER and R. RUTISHAUSER, "The fundamental relevance of morphology and morphogenesis to plant research," *Annals of Botany*, vol. 80, no. 5, pp. 571–582, 1997.

[54] T. Garland Jr and J. B. Losos, "Ecological morphology of locomotor performance in squamate reptiles," *Ecological morphology: integrative organismal biology*, pp. 240–302, 1994.

[55] P. Aerts, R. Van Damme, B. Vanhooydonck, A. Zaaf, and A. Herrel, "Lizard locomotion: how morphology meets ecology," *Netherlands Journal of Zoology*, vol. 50, no. 2, pp. 261–278, 2000.

[56] M. F. Flajnik and M. Kasahara, "Origin and evolution of the adaptive immune system: genetic events and selective pressures," *Nature Reviews Genetics*, vol. 11, no. 1, pp. 47–59, 2010.

[57] G. M. Erickson, P. M. Gignac, S. J. Steppan, A. K. Lappin, K. A. Vliet, J. D. Brueggen, B. D. Inouye, D. Kledzik, and G. J. W. Webb, "Insights into the ecology and evolutionary success of crocodilians revealed through bite-force and tooth-pressure experimentation," *PLOS ONE*, vol. 7, no. 3, p. e31781, 2012.

[58] T. McGeer *et al.*, "Passive dynamic walking," *Int. J. Robotics Res.*, vol. 9, no. 2, pp. 62–82, 1990.

[59] K. L. Hoffman and R. J. Wood, "Passive undulatory gaits enhance walking in a myriapod millirobot," in *2011 IEEE/RSJ International Conference on Intelligent Robots and Systems*, pp. 1479–1486, 2011.

[60] Z. Gan, T. Wiestner, M. A. Weishaupt, N. M. Waldern, and C. David Remy, "Passive Dynamics Explain Quadrupedal Walking, Trotting, and Tölting," *Journal of Computational and Nonlinear Dynamics*, vol. 11, 08 2015.

[61] S. Collins, A. Ruina, R. Tedrake, and M. Wisse, "Efficient bipedal robots based on passive-dynamic walkers," *Science*, vol. 307, no. 5712, pp. 1082–1085, 2005.

[62] M. A. Johnson and M. H. Moradi, *PID control*. Springer, 2005.

[63] N. Bredeche, E. Haasdijk, and A. Prieto, "Embodied evolution in collective robotics: a review," *Frontiers in Robotics and AI*, vol. 5, p. 12, 2018.

[64] C. Paul, "Morphological computation: A basis for the analysis of morphology and control requirements," *Robotics and Autonomous Systems*, vol. 54, no. 8, pp. 619–630, 2006. Morphology, Control and Passive Dynamics.

[65] T. F. Nygaard, C. P. Martin, D. Howard, J. Torresen, and K. Glette, "Environmental Adaptation of Robot Morphology and Control Through Real-World Evolution," *Evolutionary Computation*, vol. 29, pp. 441–461, 12 2021.

[66] R. M. Füchslin, A. Dzyakanchuk, D. Flumini, H. Hauser, K. J. Hunt, R. H. Luchsinger, B. Reller, S. Scheidegger, and R. Walker, "Morphological Computation and Morphological Control: Steps Toward a Formal Theory and Applications," *Artificial Life*, vol. 19, pp. 9–34, 01 2013.

[67] A. Ishiguro, M. Shimizu, and T. Kawakatsu, "Don't try to control everything!: an emergent morphology control of a modular robot," *2004 IEEE/RSJ International Conference on Intelligent Robots and Systems (IROS) (IEEE Cat. No.04CH37566)*, vol. 1, pp. 981–985 vol.1, 2004.

[68] I. F. Rosendo A, von Atzigen M, "The trade-off between morphology and control in the co-optimized design of robots," *PLoS One*, vol. 12, 10 2017.

[69] R. Ortega and M. W. Spong, "Adaptive motion control of rigid robots: A tutorial," *Automatica*, vol. 25, no. 6, pp. 877–888, 1989.

[70] C. Abdallah, D. Dawson, P. Dorato, and M. Jamshidi, "Survey of robust control for rigid robots," *IEEE Control Systems Magazine*, vol. 11, no. 2, pp. 24–30, 1991.

[71] F. Schmitt, O. Piccin, L. Barbé, and B. Bayle, "Soft robots manufacturing: A review," *Frontiers in Robotics and AI*, vol. 5, 2018.

[72] D. Rus and M. T. Tolley, "Design, fabrication and control of soft robots," *Nature*, vol. 521, no. 7553, pp. 467–475, 2015.

[73] C. Calladine, "Buckminster fuller's "tensegrity" structures and clerk maxwell's rules for the construction of stiff frames," *International Journal of Solids and Structures*, vol. 14, no. 2, pp. 161–172, 1978.

[74] A. Pugh, *An introduction to tensegrity*. Univ of California Press, 1976.

[75] C. Sultan, *Modeling, design, and control of tensegrity structures with applications*. Purdue University, 1999.

[76] R. Skelton, R. Adhikari, J.-P. Pinaud, W. Chan, and J. Helton, "An introduction to the mechanics of tensegrity structures," in *Proceedings of the 40th IEEE Conference on Decision and Control (Cat. No.01CH37228)*, vol. 5, pp. 4254–4259 vol.5, 2001.

[77] D. S. Shah, J. W. Booth, R. L. Baines, K. Wang, M. Vespignani, K. Bekris, and R. Kramer-Bottiglio, "Tensegrity robotics," *Soft Robotics*, vol. 9, no. 4, pp. 639–656, 2022.

[78] Y. Liu, Q. Bi, X. Yue, J. Wu, B. Yang, and Y. Li, "A review on tensegrity structures-based robots," *Mechanism and Machine Theory*, vol. 168, p. 104571, 2022.

[79] K. Caluwaerts, J. Despraz, A. Işçen, A. P. Sabelhaus, J. Bruce, B. Schrauwen, and V. SunSpiral, "Design and control of compliant tensegrity robots through simulation and hardware validation," *Journal of The Royal Society Interface*, vol. 11, no. 98, p. 20140520, 2014.

[80] C. Paul, F. Valero-Cuevas, and H. Lipson, "Design and control of tensegrity robots for locomotion," *IEEE Transactions on Robotics*, vol. 22, no. 5, pp. 944–957, 2006.

[81] R. Kobayashi, H. Nabae, G. Endo, and K. Suzumori, "Soft tensegrity robot driven by thin artificial muscles for the exploration of unknown spatial configurations," *IEEE Robotics and Automation Letters*, vol. 7, no. 2, pp. 5349–5356, 2022.

[82] C. Sultan, "Chapter 2 tensegrity: 60 years of art, science, and engineering," in *Advances in Applied Mechanics*, vol. 43 of *Advances in Applied Mechanics*, pp. 69–145, Elsevier, 2009.

[83] U. Saranli, M. Buehler, and D. E. Koditschek, "Rhex: A simple and highly mobile hexapod robot," *The International Journal of Robotics Research*, vol. 20, no. 7, pp. 616–631, 2001.

[84] T. Sheridan, "Human supervisory control of robot systems," in *Proceedings. 1986 IEEE International Conference on Robotics and Automation*, vol. 3, pp. 808–812, 1986.

[85] S. Kajita, F. Kanehiro, K. Kaneko, K. Yokoi, and H. Hirukawa, "The 3d linear inverted pendulum mode: a simple modeling for a biped walking pattern generation," in *Proceedings 2001 IEEE/RSJ International Conference on Intelligent Robots and Systems. Expanding the Societal Role of Robotics in the the Next Millennium (Cat. No.01CH37180)*, vol. 1, pp. 239–246 vol.1, 2001.

[86] F. Asano, "Fully analytical solution to discrete behavior of hybrid zero dynamics in limit cycle walking with constraint on impact posture," *Multibody System Dynamics*, vol. 35, no. 2, pp. 191–213, 2015.

[87] M. Wisse, A. Schwab, R. van der Linde, and F. van der Helm, "How to keep from falling forward: elementary swing leg action for passive dynamic walkers," *IEEE Transactions on Robotics*, vol. 21, no. 3, pp. 393–401, 2005.

[88] J. Yan and S. Agrawal, "Rimless wheel with radially expanding spokes: dynamics, impact, and stable gait," in *IEEE International Conference on Robotics and Automation, 2004. Proceedings. ICRA '04. 2004*, vol. 4, pp. 3240–3244 Vol.4, 2004.

[89] N. Fazeli, R. Kolbert, R. Tedrake, and A. Rodriguez, "Parameter and contact force estimation of planar rigid-bodies undergoing frictional contact," *The International Journal of Robotics Research*, vol. 36, no. 13-14, pp. 1437–1454, 2017.

[90] Y. Or, "Painlevé s paradox and dynamic jamming in simple models of passive dynamic walking," *Regular and Chaotic Dynamics*, vol. 19, no. 1, pp. 64–80, 2014.

[91] M. J. Coleman, A. Chatterjee, and A. Ruina, "Motions of a rimless spoked wheel: a simple three-dimensional system with impacts," *Dynamics and Stability of Systems*, vol. 12, no. 3, pp. 139–159, 1997.

[92] S. Iqbal, X. Zang, Y. Zhu, and J. Zhao, "Bifurcations and chaos in passive dynamic walking: A review," *Robotics and Autonomous Systems*, vol. 62, no. 6, pp. 889–909, 2014.

[93] M. Wisse and J. van Frankenhuyzen, "Design and construction of mike; a 2-d autonomous biped based on passive dynamic walking," *Adaptive Motion of Animals and Machines*, pp. 143–154, 2006.

[94] M. Wisse, "Essentials of dynamic walking; analysis and design of two-legged robots," 2004.

[95] T. Cnops, Z. Gan, and C. D. Remy, "The basin of attraction for running robots: Fractals, multistep trajectories, and the choice of control," *2015 IEEE/RSJ International Conference on Intelligent Robots and Systems (IROS)*, pp. 1586–1591, 2015.

[96] S. Heim and A. Spröwitz, "Beyond basins of attraction: Quantifying robustness of natural dynamics," *IEEE Transactions on Robotics*, vol. 35, no. 4, pp. 939–952, 2019.

[97] A. Wuensche, "Genomic regulation modeled as a network with basins of attraction," *Pacific Symposium on Biocomputing. Pacific Symposium on Biocomputing*, p. 89—102, 1998.

[98] *Basin of Attraction of the Simplest Walking Model*, vol. Volume 6A: 18th Biennial Conference on Mechanical Vibration and Noise of *International Design Engineering Technical Conferences and Computers and Information in Engineering Conference*, 09 2001.

[99] E. Eschenazi, H. G. Solari, and R. Gilmore, "Basins of attraction in driven dynamical systems," *Phys. Rev. A*, vol. 39, pp. 2609–2627, Mar 1989.

[100] M. S. Suraj, M. C. Asique, U. Prasad, M. Hassan, and K. Shalini, "Fractal basins of attraction in the restricted four-body problem when the primaries are triaxial rigid bodies," *Astrophysics and Space Science*, vol. 362, pp. 1–16, 2017.

[101] D. D. Quinn, A. L. Triplett, L. A. Bergman, and A. F. Vakakis, "Comparing Linear and Essentially Nonlinear Vibration-Based Energy Harvesting," *Journal of Vibration and Acoustics*, vol. 133, 12 2010. 011001.

Publications

Journal Paper

[1] Yanqiu Zheng, Longchuan Li, Yuxuan Xiang, Yuetong He, Cong Yan, Fumihiko Asano, "Motion analysis of passive dynamic walking with a rigorously constraint model: A necessary condition for maintaining period-1 gait," *Biomimetic Intelligence and Robotics*, vol. 2, No. 2, pp. 100048, 2022.

[2] Fumihiko Asano, Yanqiu Zheng, "High-speed and energy-efficient collisionless walking of underactuated rimless wheel," *Artificial Life and Robotics*, vol. 23, No. 4, pp. 523-531, 2018.

[3] Fumihiko Asano, Yanqiu Zheng, Xuan Xiao, "Time-scale control approaches to collisionless walking of an underactuated rimless wheel," *Journal of Robotics and Mechatronics*, vol. 29, No. 3, pp. 471-479, 2017.

International Conference

[4] Fumihiko Asano, Yuxuan Xiang, Yanqiu Zheng, Cong Yan, "Motion Analysis of Planar Passive-dynamic Walkers with Different Tensegrity Structures Formed by Four Rigid Frames and Eight Viscoelastic Elements," *2022 International Conference on Advanced Robotics and Mechatronics (ICARM)*, pp. 95-100, 2022.

[5] Fumihiko Asano, Yuxuan Xiang, Yanqiu Zheng, Cong Yan, "Modeling, Analysis and Activation of Planar Viscoelastically-Combined Rimless Wheels," *2022 IEEE/RSJ International Conference on Intelligent Robots and Systems (IROS)*, pp. 12957-12962, 2022.

[6] Runyu Liu, Fumihiko Asano, Yanqiu Zheng, Cong Yan, "Ultrahigh-speed Stealth Walking on Zero-friction Floating Island Based on Horizontal and Vertical Ground Reaction Force Control," *2022 13th Asian Control Conference (ASCC)*, pp. 1221-1226, 2022.

[7] Yuetong He, Fumihiko Asano, Yanqiu Zheng, Cong Yan, "Water Surface Walking and Gait Efficiency Analysis of Legged Locomotion Robot Equipped with Floats on Feet," *2022 13th Asian Control Conference (ASCC)*, pp. 1227-1232, 2022.

[8] Yanqiu Zheng, Fumihiko Asano, Cong Yan, Longchuan Li, "A modeling method of passive dynamic walking with a rigorously constraint model," *Proceedings of the Fifth International Symposium on Swarm Behavior and Bio-Inspired Robotics*, pp. 1705-1708, 2022.

[9] Cong Yan, Yanqiu Zheng, Fumihiko Asano, Longchuan Li, "Modeling and analysis of bipedal robot walking uphill by hybrid control," *Proceedings of the Fifth International Symposium on Swarm Behavior and Bio-Inspired Robotics*, pp. 1709-1713, 2022.

[10] Cong Yan, Haosong Chen, Yanqiu Zheng, Longchuan Li, Isao Tokuda, Fumihiko Asano, "Entrainment-Based Control for Underactuated Compass-Like Biped Robot," *2021 20th International Conference on Advanced Robotics (ICAR)*, pp. 404-409, 2021.

[11] Yanqiu Zheng, Fumihiko Asano, Longchuan Li, Cong Yan, "Analysis of Passive Dynamic Gait of Tensegrity Robot," *Climbing and Walking Robots Conference*, pp. 274-285, 2021.

[12] Cong Yan, Fumihiko Asano, Yanqiu Zheng, Longchuan Li, "Analysis of Biped Robot on Uneven Terrain Based on Feed-Forward Control," *Climbing and Walking Robots Conference*, pp. 37-39, 2021.

[13] Fumihiko Asano, Yanqiu Zheng, Longchuan Li, "Modeling and Motion Analysis of Planar Passive-Dynamic Walker with Tensegrity Structure Formed by Four Limbs andEight Viscoelastic Elements," *Climbing and Walking Robots Conference*, pp. 242-254, 2021.

[14] Cong Yan, Haosong Chen, Yanqiu Zheng, Fumihiko Asano, "Gait analysis of biped robot with semicircular feet only on front side driven by sinusoidal hip torque," *Proceedings of the SWARM2021: The 4th International Symposium on Swarm Behavior and Bio-inspired Robotics*, pp. 486-497, 2021.

[15] Yanqiu Zheng, Longchuan Li, Fumihiko Asano, Cong Yan, Xindi Zhao, Haosong Chen, "Modeling and Analysis of Tensegrity Robot for Passive Dynamic Walking," *2021 IEEE/RSJ International Conference on Intelligent Robots and Systems (IROS)*, pp. 2479-2484, 2021.

[16] Yanqiu Zheng, Fumihiko Asano, "Toward collisionless walking without including period of double-limb support," *Proceedings of the SWARM2017: The 2nd International Symposium on Swarm Behavior and Bio-inspired Robotics*, pp. 29-32, 2017.

[17] Fumihiko Asano, Yanqiu Zheng, Yasunori Kikuchi, Xuan Xiao, "Generation of collisionless walking gait for non-straight-legged biped," *2017 56th Annual Conference of the Society of Instrument and Control Engineers of Japan (SICE)*, pp. 817-820, 2017.

[18] Fumihiko Asano, Yasunori Kikuchi, Yanqiu Zheng, Xuan Xiao, "Effect of non-straight leg frames on gait efficiency in collisionless walking," *2017 56th Annual Conference of the Society of Instrument and Control Engineers of Japan (SICE)*, pp. 821-824, 2017.

[19] Fumihiko Asano, Ryosuke Nakamura, Mingyang Wu, Taiki Seino, Yanqiu Zheng, "Modeling and control of underactuated rimless wheel for walking over quagmire," *2016 Australian Control Conference (AuCC)*, pp. 364-369, 2016.

[20] Fumihiko Asano, Yanqiu Zheng, Xuan Xiao, "Generation of underactuated bipedal gait completing in one step," *2016 IEEE/RSJ International Conference on Intelligent Robots and Systems (IROS)*, pp. 2050-2055, 2016.